

The Pennsylvania State University
The Graduate School
Department of Materials Science and Engineering

PATTERNED SOLID STATE GROWTH OF BaTiO₃ CRYSTALS

A Dissertation in
Materials Science and Engineering

by

Michael Stephen Ugorek

© 2009 Michael Stephen Ugorek

Submitted in Partial Fulfillment
of the Requirements
for the Degree of

Doctor of Philosophy

May 2009

The dissertation of Michael Stephen Ugorek was reviewed and approved* by the following:

Gary L. Messing
Distinguished Professor of Ceramic Science and Engineering
Head of the Department of Materials Science and Engineering
Dissertation Co-Advisor
Chair of Committee

Susan Troler-McKinstry
Professor of Ceramic Science and Engineering
Dissertation Co-Advisor

Clive A. Randall
Professor of Materials Science and Engineering

Thomas R. Shrout
Senior Scientist and Professor of Materials Science and Engineering

*Signatures are on file in the Graduate School

ABSTRACT

An understanding of microstructure evolution in ceramic materials, including single crystal development and abnormal / enhanced grain growth should enable more controlled final ceramic element structures. In this study, two different approaches were used to control single crystal development in a patterned array. These two methods are: 1) patterned solid state growth in BaTiO₃ ceramics, and 2) metal – mediated single crystal growth in BaTiO₃.

With the patterned solid state growth technique, optical photolithography was used to pattern dopants as well as [001] and [110] BaTiO₃ single crystal template arrays with a 1000 μm line pattern array with 1000 μm spacings. These patterns were subsequently used to control the matrix grain growth evolution and single crystal development in BaTiO₃. It was shown that the growth kinetics can be controlled by a small initial grain size, atmosphere conditions, and the introduction of a dopant at selective areas / interfaces. By using a PO₂ of 1x10⁻⁵ atm during high temperature heat treatment, the matrix coarsening has been limited (to roughly 2 times the initial grain size), while retaining single crystal boundary motion up to 0.5 mm during growth for dwell times up to 9 h at 1300°C. The longitudinal and lateral growth rates were optimized at 10 – 15 μm/h at 1300°C in a PO₂ of 1x10⁻⁵ atm for single crystal growth with limited matrix coarsening. Using these conditions, a patterned microstructure in BaTiO₃ was obtained.

With the metal – mediated single crystal growth technique, a novel approach for fabricating 2-2 single crystal / polymer composites with a kerf < 5 microns was demonstrated. Surface templated grain growth was used to propagate a single crystal interface into a polycrystalline BaTiO₃ or Ba(Zr_{0.05}Ti_{0.95})O₃ matrix with lamellar nickel layers. The grain growth evolution and texture development were studied using both [001] and [110] BaTiO₃ single crystals templates. By using a PO₂ of 1x10⁻¹¹ atm during high temperature heat treatment, matrix coarsening was limited while enabling single crystal boundary motion up to 0.35 mm during growth between 1250°C and 1300°C with

growth rates $\sim 3\text{-}4 \mu\text{m/h}$ for both single crystal orientations. By removing the inner electrodes, 2-2 single crystal (or ceramic) composites were prepared. The piezoelectric and dielectric properties of the composites of the two compositions were measured. The d_{33} and d_{31} of the composites were similar to the polycrystalline ceramic of the same composition.

TABLE OF CONTENTS

LIST OF FIGURES	vii
LIST OF TABLES	xiii
ACKNOWLEDGEMENTS	xiv
Chapter 1 Introduction	1
1.1 Statement of the Problem	1
1.2 Scientific Goals and Overview	5
1.3 Organization of the Thesis	6
1.4 References	7
Chapter 2 Literature Review	9
2.1 Background on BaTiO ₃	9
2.1.1 Crystal Structure	9
2.1.2 Dielectric and Piezoelectric Properties	13
2.1.2.1 Polarization	14
2.1.2.2 Dielectric Permittivity	17
2.1.2.3 Piezoelectricity	20
2.1.3 Stoichiometry and Phase Equilibrium	22
2.2 Synthesis	26
2.2.1 Single Crystals	26
2.2.2 Textured Ceramics	30
2.3 Microstructure Evolution	33
2.3.1 Sintering / Normal Grain Growth	33
2.3.2 Exaggerated Grain Growth by Doping	35
2.3.3 Atmosphere Control	37
2.3.4 Grain Growth Inhibition	39
2.4 Patterning Techniques	40
2.5 References	45
Chapter 3 Enhanced BaTiO ₃ Grain Growth by Surface Doping	50
3.1 Introduction	50
3.2 Experimental Procedure	52
3.3 Results and Discussion	55
3.3.1 BaTiO ₃ Matrix Fabrication	55
3.3.1 Grain Growth in TiO ₂ and SiO ₂ Surface Patterned BaTiO ₃	57
3.4 Conclusions	68
3.5 References	68

Chapter 4 Patterned Solid State Growth of BaTiO ₃ Crystals	71
4.1 Introduction.....	71
4.2 Experimental Procedure.....	72
4.2.1 Patterned Single Crystal Template Fabrication.....	72
4.2.2 Bonding and Growth of BaTiO ₃ Template Crystals.....	75
4.3 Results and Discussion	77
4.3.1 Patterned Single Crystal Growth.....	81
4.4 Conclusions.....	88
4.5 References.....	89
Chapter 5 Fabrication of a 2-2 Ultrasound Transducer Array by Metal – Mediated Single Crystal Growth in BaTiO ₃	91
5.1 Background.....	91
5.2 Introduction.....	95
5.3 Experimental Procedure.....	96
5.3.1 Matrix Fabrication.....	96
5.3.2 Single Crystal / Polymer Composite Fabrication	98
5.3.3 Dielectric and Piezoelectric Property Measurements.....	101
5.4 Results and Discussion	102
5.4.1 Dielectric and Piezoelectric Results	115
5.5 Conclusions.....	127
5.6 References.....	128
Chapter 6 Summary and Future Work.....	131
6.1 Summary.....	131
6.2 Future Work.....	135
6.3 References.....	138

LIST OF FIGURES

Figure 1-2: SEM image of a $\text{Sr}_{0.53}\text{Ba}_{0.47}\text{Nb}_2\text{O}_6$ microstructure fabricated by TGG. ...	4
Figure 2-1: Schematic representation of the cubic BaTiO_3 perovskite unit cell.....	10
Figure 2-2: Schematic of a) a tetragonal BaTiO_3 unit cell and b) projection of the structure in the a-c plane, showing the relative displacements of the Ti^{4+} and O^{2-} ions. ²	10
Figure 2-3: Schematic of the phase transitions and unit cell dimensions in BaTiO_3 as a function of temperature. ³	11
Figure 2-4: Transition temperature trends as a function of dopant in BaTiO_3 . ³	12
Figure 2-5: Schematic of the frequency dependence of the relative permittivity due to the different polarization mechanisms. ³	13
Figure 2-6: Spontaneous polarization as a function of temperature for tetragonal BaTiO_3 . ⁴	15
Figure 2-7: Schematic of a BaTiO_3 ferroelectric hysteresis loop on a polarization (P) vs. electric field (E) graph. ⁵	17
Figure 2-8: Dielectric constant as a function of temperature for both pure BaTiO_3 (ϵ_{33} , ϵ_{11} , ϵ_{22}) ⁸ and $\text{Ba}(\text{Zr}_{0.05}\text{Ti}_{0.95})\text{O}_3$ (ϵ_{33}) ⁹ single crystals.	19
Figure 2-9: Schematic showing the a) direct and b) converse piezoelectric response. V = voltage, P = polarization direction, and L = length of the ceramic. The blue arrows denote an applied stress.....	20
Figure 2-10: Schematic of the engineered domain states for a) tetragonal BaTiO_3 ¹⁵ and b) orthorhombic BaTiO_3	22
Figure 2-11: Ti-rich, BaO-TiO ₂ phase equilibrium diagram.	23
Figure 2-12: BaO – TiO ₂ phase diagram under ambient air conditions. The dotted lines are extrapolated. BT S.S. = BaTiO_3 solid solution, Hex. = Hexagonal, Cub. = Cubic. ¹⁷	24
Figure 2-13: Ternary phase diagram of the BaO-TiO ₂ -Ti ₂ O ₃ system under heavy reducing conditions ($\text{PO}_2 < 1 \times 10^{-14}$ atm) for temperatures above 1300°C.....	25

Figure 2-14: a) Schematic and b) optical image showing the faceted planes of the grown single crystal in polycrystalline BaTiO ₃ from a [001] BaTiO ₃ single crystal. ²⁷	29
Figure 2-15: Schematic of the alignment of templates by tape casting and the texture development during the heat treatment.	30
Figure 2-16: Micrograph of solid state sintered BaTiO ₃ in air at 1300°C. ³⁶	34
Figure 2-17: Micrograph of BaTiO ₃ sintered via liquid phase sintering. The area marked M is the matrix grains (~1µm), and the area marked A are the abnormal grains. ³⁸	35
Figure 2-18: TEM images of a) low magnification image and b) high resolution image of grain boundaries in 0.4 mol% BaTiO ₃ sintered at 1300°C for 8 h in H ₂ after 1250°C for 30 min in H ₂ . ⁴⁶	38
Figure 2-19: TEM images of a) low magnification image and b) high resolution image of grain boundaries in 0.4 mol% BaTiO ₃ sintered at 1300°C for 8 h in air after 1250°C for 30 min in H ₂ . ⁴⁶	38
Figure 2-20: SEM images of colloidal alignment with different geometries produced by Yin et al. The arrows indicate missing particles. ⁵³	41
Figure 2-21: Schematics of different writing schemes, A) Precursor solution are decomposed near the focal point of a beam to deposit material on the surface. B) Ink Jet Printing, where liquids are ejected from a nozzle and deposited on the surface of the substrate. C) Direct writing of particles or a liquid onto a substrate. D) Fluorescence microscopy of an array of hybridized DNA sequences produced by dip-pen nanolithography. ⁵⁴	42
Figure 2-22: SEM images of different patterns produced by soft-lithography. ⁵⁴	44
Figure 3-1: Optical Image of the 1000 µm TiO ₂ line pattern (light region) on a polished polycrystalline BaTiO ₃ sample (dark region).	54
Figure 3-2: Average grain size as a function of relative density for air sintering (solid line) and reducing sintering at PO ₂ 1x10 ⁻¹¹ atm of BaTiO ₃ ceramics (dotted line).....	56
Figure 3-3: SEM image showing a polished and thermally etched (1200°C, 10 min, in air) surface of the BaTiO ₃ sample fired in PO ₂ = 1x10 ⁻¹¹ atm at 1300°C for 1.25 h.....	57

Figure 3-4: SEM micrographs showing the diffusion affected zone was observed using 300 nm of a) TiO ₂ and b) SiO ₂ fired in air at 1300°C for 10 min.	58
Figure 3-5: XRD analysis of the surface of the 300 nm SiO ₂ doped BaTiO ₃ sample fired in air at 1300°C for 10 min. (JCPDS Card #'s 00-005-0626 for BaTiO ₃ and 00-022-0513 for Ba ₂ TiSi ₂ O ₈).	58
Figure 3-6: An optical image of the enhanced growth region (light gray) in contrast to the remaining matrix grains (dark gray) for a 150 nm TiO ₂ doped BaTiO ₃ sample fired in air at 1300°C for 1 h.	59
Figure 3-7: Vertical and lateral growth distances as a function of time at 1300°C in air for 150 nm TiO ₂ doped BaTiO ₃ sample from 0.5 to 2 h.	60
Figure 3-8: Grain growth kinetics of matrix coarsening in BaTiO ₃ plotting log G vs. log t to determine the value of n.	61
Figure 3-9: Optical image of 150 nm TiO ₂ surface doped BaTiO ₃ fired in air to 1350°C for 0.5 h.	62
Figure 3-10: SEM micrographs of the samples with a) 50 nm, b) 100 nm, and c) 150 nm thick TiO ₂ layers fired to 1300°C for 0.5 h in a PO ₂ of 1x10 ⁻⁵ atm.	64
Figure 3-11: Growth of diffusion affected zone as a function of time for the samples fired in air at 1300°C and PO ₂ of 1x10 ⁻⁵ atm (red.).	66
Figure 3-12: SEM micrograph of the sample with 100 nm thick TiO ₂ layer fired to 1300°C for 2 h in a PO ₂ of 1x10 ⁻⁵ atm.	66
Figure 3-13: Cross section of a 150 nm TiO ₂ surface patterned BaTiO ₃ fired at 1350°C for 0.5 h in PO ₂ of 1x10 ⁻⁵ atm. The black bars on the top indicate the position of the original TiO ₂ patterns.	67
Figure 3-14: EBSD image of 150 nm TiO ₂ surface patterned BaTiO ₃ fired at 1350°C for 1 h in air showing the orientation of the diffusion affected zone.	67
Figure 4-1: Schematic of the template fabrication process.	74
Figure 4-2: Optical image of the etched single crystal showing a line pattern.	75
Figure 4-3: Schematic of the setup for bonding the BaTiO ₃ polycrystalline matrix to the patterned single crystal.	76
Figure 4-4: SEM images of a BaTiO ₃ single crystal bonded in air at 1350°C for 2 h (a) without and (b) with a TiO ₂ interface layer. The dotted line indicates the initial interface between the single crystal and ceramic.	78

Figure 4-5: Crystal boundary velocity as a function of atmosphere for [001] BaTiO ₃ single crystal conversion at 1300°C for 2 h dwell at each PO ₂ level.	79
Figure 4-6: Optical image of the crystal grown from a [100] BaTiO ₃ single crystal fired at 1300°C for 9 h in PO ₂ of 1x10 ⁻⁵ atm, with an inset SEM image of the matrix material.....	80
Figure 4-7: Optical images showing the patterned [110] BaTiO ₃ crystal before and after a 3 h growth run at 1300°C in a PO ₂ of 1x10 ⁻⁵ atm.	82
Figure 4-8: Distance of the crystal conversion as a function of time for the lateral and vertical directions with [001] and [110] single crystal templates at 1300°C in a PO ₂ of 1x10 ⁻⁵ atm.	84
Figure 4-9: Optical image of the equilibrium morphology of the grown crystal from a [100] BaTiO ₃ single crystal grown at 1300°C, PO ₂ of 1x10 ⁻⁵ atm for 25 h.	85
Figure 4-10: SEM image of the needle-like structures in the single crystal from the growth at 1300°C, PO ₂ of 1x10 ⁻⁵ atm for 25 h run outlined in Figure 4-9.	85
Figure 4-11: Optical image of the growth from the equilibrium morphology of the grown crystal from a [100] BaTiO ₃ single crystal grown at 1300°C, PO ₂ of 1x10 ⁻⁵ atm for an additional 2 h.	86
Figure 4-12: EBSD image showing the orientation of the grown crystal relative to the [100] template single crystal when heated to 1300°C for 25 h in PO ₂ of 1x10 ⁻⁵ atm.	87
Figure 4-13: SEM image showing the surface roughness of the grown crystal when heated to 1300°C for 25 h in PO ₂ of 1x10 ⁻⁵ atm.	88
Figure 5-1: XRD scan of the Ba(Zr _{0.05} Ti _{0.95})O ₃ powder calcined at 1100°C for 4 h in air. Indexed using an orthorhombic cell. (JCPDS Card # 00-056-1034).	96
Figure 5-2: Schematic of the screen printing and composite fabrication process.	97
Figure 5-3: Schematic of single crystal conversion into BaTiO ₃ / nickel 2-2 composite.....	99
Figure 5-4: Optical micrographs of the cross section of the etched and backfilled ceramic / epoxy composites etched using HNO ₃ for a) a continuous 4 h etch and b) removal and washing after 5 minute etch intervals.	100
Figure 5-5: Schematic showing the ceramic and epoxy layers of the composite with respect to the gold electrodes (colored black).	101

Figure 5-6: SEM image showing the nickel layer (middle) separating the polycrystalline BaTiO ₃ ceramic layers fired to 1300°C in a 1x10 ⁻¹³ atm PO ₂ for 1.25 h.....	103
Figure 5-7: SEM images showing a) polished and etched composite with the nickel layers and b) a composite sample after removing the nickel layers and backfilling with epoxy.	104
Figure 5-8: Graph of grain boundary velocity using a [001] BaTiO ₃ single crystal as a function of atmosphere for BaTiO ₃ and Ba(Zr _{0.05} Ti _{0.95})O ₃ samples fired at 1300°C for 2 h.....	105
Figure 5-9: Optical image of the growth of a [001] single crystal boundary through the commercial MLCC at 1300°C in PO ₂ of 1x10 ⁻¹¹ atm for 40 h. The dotted line indicates the original boundary between the single crystal and the capacitor.....	106
Figure 5-10: SEM image of the grown crystal with the lateral growth mediated by the nickel layers in the MLCC at 1300°C in PO ₂ of 1x10 ⁻¹¹ atm for 40 h. The dotted line indicates the original boundary between the single crystal and the MLCC.....	107
Figure 5-11: Optical image of a [001] BaTiO ₃ single crystal bonded to the 2-2 composite matrix at 1300°C in PO ₂ of 1x10 ⁻¹¹ atm for up to 80 h.....	108
Figure 5-12: a) Optical micrograph of a BaTiO ₃ sample fired at 1300°C for 70 h in a 1x10 ⁻¹¹ atm PO ₂ showing the nickel discontinuity along the metal layer, and b) Optical micrograph of a BaTiO ₃ sample heated at 1250°C for 100 h in a 1x10 ⁻¹¹ atm PO ₂ showing nickel continuity.	109
Figure 5-13: A BaTiO ₃ composite sample bonded to a [001] BaTiO ₃ single crystal fired at 1250°C for 30 h in a 1x10 ⁻¹¹ atm PO ₂	111
Figure 5-14: A BaTiO ₃ composite sample bonded to a [001] BaTiO ₃ single crystal fired at 1250°C for a total of 45 h in a 1x10 ⁻¹¹ atm PO ₂	111
Figure 5-15: An optical micrograph of a Ba(Zr _{0.05} Ti _{0.95})O ₃ / nickel composite that has been heated to 1250°C for 100 h in a PO ₂ of 1x10 ⁻¹¹ atm.	112
Figure 5-16: An optical micrograph of a Ba(Zr _{0.05} Ti _{0.95})O ₃ / epoxy composite, with an inset SEM image showing the single crystal / epoxy boundary.	113
Figure 5-17: Optical micrographs of the cross section of the etched and backfilled ceramic / epoxy composites etched using HNO ₃ for a) a continuous 4 h etch and b) removal and washing after 5 minute etch intervals.	114

Figure 5-18: Dielectric permittivity and loss tangents as a function of temperature for BaTiO ₃ ceramic and epoxy composites from 100 Hz to 100 kHz.	116
Figure 5-19: Dielectric permittivity as a function of temperature for Ba(Zr _{0.05} Ti _{0.95})O ₃ ceramic and epoxy composites from 100 Hz to 100 kHz.	117
Figure 5-20: Polarization vs. electric field for a BaTiO ₃ ceramic measured at 10 Hz.	120
Figure 5-21: Schematic showing the configurations of the composite geometry used for the d ₃₃ strain vs. field and the d ₃₁ resonance measurements. The black regions represent the electrode area.	120
Figure 5-22: Bipolar strain vs. electric field for a BaTiO ₃ ceramic and composite samples measured at 1 Hz.	121
Figure 5-23: Unipolar strain vs. electric field for a BaTiO ₃ ceramic and composite samples measured at 1 Hz.	122
Figure 5-24: Bipolar strain vs. electric field for a Ba(Zr _{0.05} Ti _{0.95})O ₃ ceramic and composite samples measured at 1 Hz.	123
Figure 5-25: Unipolar strain vs. electric field for a Ba(Zr _{0.05} Ti _{0.95})O ₃ ceramic and composite samples measured at 1 Hz.	124
Figure 6-1: Schematic of different template shapes and sizes (colored areas) for single crystal growth impingement experiments. The arrows show the direction of grown crystal directions with the dotted lines projecting the single crystal growth front.	137

LIST OF TABLES

Table 3-1 : Constants d_{33} , k_{33} , ϵ_{33} , and s_{33} in different BaTiO ₃ single crystal cut directions. ⁸	52
Table 4-1 : Conditions for nickel sputter deposition.	73
Table 4-2 : ICP-RIE conditions for producing single crystal templates.	74
Table 5-1 : Processing techniques and current resolution limits for composite transducers.	95
Table 5-2 : Single crystal growth rates at 1250°C and 1300°C (in parenthesis) at a PO ₂ of 1×10^{-11} atm for BaTiO ₃ and Ba(Zr _{0.05} Ti _{0.95})O ₃ samples bonded to [001] and [110] BaTiO ₃ single crystals.	110
Table 5-3 : Dielectric permittivity and loss at 1 kHz for BaTiO ₃ and Ba(Zr _{0.05} Ti _{0.95})O ₃ ceramic and epoxy composites.	118
Table 5-4 : Calculated and measured dielectric permittivity at room temperature and at the Curie temperature at 1 kHz for BaTiO ₃ and Ba(Zr _{0.05} Ti _{0.95})O ₃ epoxy composites.	119
Table 5-5 : Transverse electromechanical coefficients of BaTiO ₃ and Ba(Zr _{0.05} Ti _{0.95})O ₃ ceramic and composite samples.	125
Table 5-6 : Measured and calculated d_{33} and d_{31} coefficients assuming the parallel model for the BaTiO ₃ and Ba(Zr _{0.05} Ti _{0.95})O ₃ / epoxy composites.	126

ACKNOWLEDGEMENTS

Foremost, I would like to thank my co-advisors, Dr. Gary Messing and Dr. Susan Trolrier-McKinstry for their support and guidance over the years. They both made my graduate experience challenging and very rewarding. Second I would like to thank my committee members Dr. Clive Randall and Dr. Tom Shrout for their help on this work.

Thank you to all the technical staff at Steidle, and MRL, particularly Amanda Baker, Maria DiCola, Bill Drawl, Scott Henninger, Maria Klimkiewicz, Eric Sagmuller and Nichole Wonderling. Without their help, it would have taken me a few more years to get through my thesis project. I would like to specifically thank Amanda Baker, for her assistance with the screen printing work, and for fabricating the nickel ink that I used. Also, in particular to Eric Sagmuller and Steve Perini who helped out greatly in fabricating the controlled atmosphere furnace in Steidle.

Thank you to the staff at MRI, especially Changjun Huang, Guy Lavallee, Joe Lonjin, Andrzej Mieckowski, and Shane Miller. I had the opportunity to work on both my thesis and other projects in the NanoFab, and their assistance and suggestions enabled the work to go by smoothly.

I am lucky to have been a part of two research groups and am grateful to have worked with everyone; you guys are not only colleagues but good friends: Aravind, Kristen, Dr. Lee, Sujarinee, Adam, Bob, Mike R., Nevin, Stephen, Nia, Libby, Julie, Cherie, Yunfei, Pierrette, Carina, Nazanin, Srowthi, Mike B., Patamas, Tanawadee, Eunki, Song Won, Ioanna, Hajime, Mustafa Burak, Dan, Ichiro, Flavio, Raegan, Raffi, Silke, and Derek. Especially thank you to Raegan and Ioanna for their assistance in fabricating the TiO_2 sol-gel solution.

I would like to thank Adam, Bob, and Steve who have spent countless hours (especially on weekends) to iron out posters and presentations that I gave through my career at PSU.

Thank you to my family and friends for their support and encouragement over the years. I would especially like to thank my wife, Trish, who has been there to help me through the stressful times (especially the last few months).

I would also like to thank my bowling buddies: Dave “Edge” Meyer, Pat “Line” Ray, Rob “Thread” Burke, Chad “Screw” Eichfeld, Dan “Partial” Tinberg, and Eric “Deter” Deithorn. Sunday night bowling was the highlight of my week. I will miss all the good times we had (and the beer frames)!

Thank you to Susie Sherlock, who became my PSU mother. Thank you for lending a chair and an ear during my impromptu stop-overs.

Finally, thank you to the Air Force Office of Scientific Research for funding my project. Thank you to Deltronics Inc. and Dr. Hasou Luo from Shanghai Institute of Ceramics for supplying the BaTiO₃ single crystals.

Chapter 1

Introduction

1.1 Statement of the Problem

In many cases, domain engineered ferroelectric single crystals show higher piezoelectric properties relative to polycrystalline ceramics of similar compositions. This was demonstrated experimentally by Park and Shrout for $(1-x) \text{Pb}(\text{Mg}_{1/3}\text{Nb}_{2/3})\text{O}_3$ - $x\text{PbTiO}_3$ (PMN-PT) and $\text{Pb}(\text{Zn}_{1/3}\text{Nb}_{2/3})\text{O}_3$ - PbTiO_3 (PZN-PT) single crystals as shown in Figure 1-1.¹

Given the interest in reduction of lead in commercial products, these ideas have also been pursued in lead-free ferroelectrics such as BaTiO_3 . For example, Rehrig et al. showed an increase in the piezoelectric coefficient (d_{33}) of single crystal $\text{Ba}(\text{Zr}_{0.05}\text{Ti}_{0.95})\text{O}_3$ to 340-355 pC/N,² and Ceracomp has produced $\text{Ba}(\text{Zr}_{0.05}\text{Ti}_{0.95})\text{O}_3$ with a d_{33} of 1150 pC/N.³ Park et al. produced orthorhombic BaTiO_3 single crystals with a d_{33} of ~500 pC/N.⁴ For other materials, the d_{33} of KNbO_3 improves to 240 pm/V⁵, and for PZN-PT with a d_{33} of 2500 pC/N.⁶

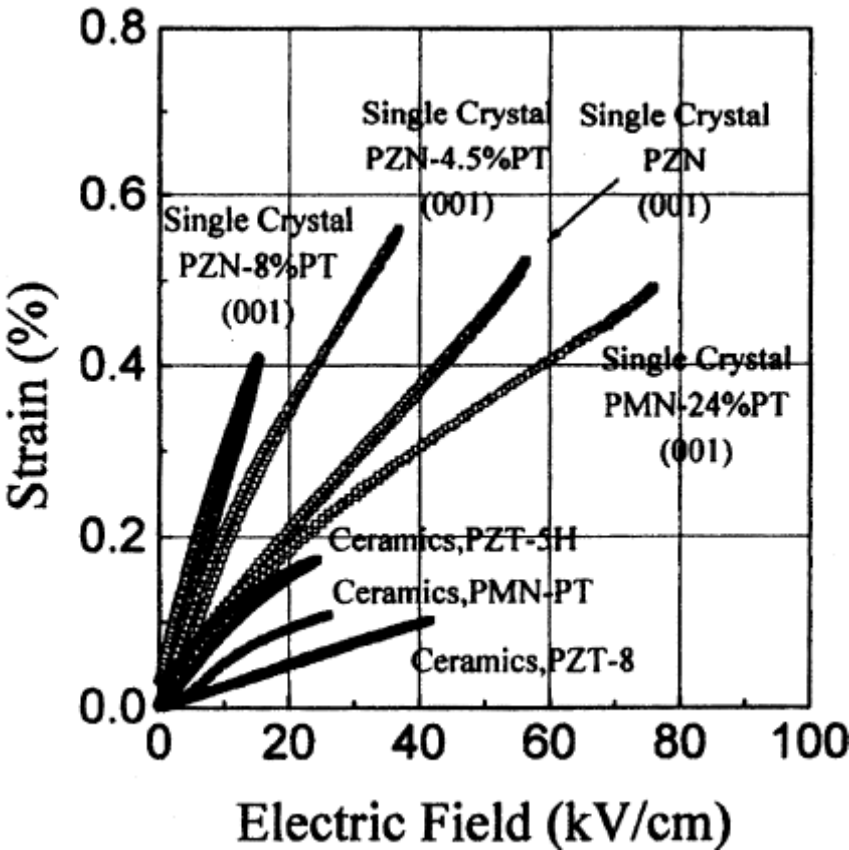


Figure 1-1: Strain vs. electric field behavior for <001> oriented rhombohedral single crystals of PZN-PT and PMN-PT and for various ceramics.

Critical to these efforts is a source of high quality single crystals or textured ceramics. Currently, top-seeded solution growth (TSSG) from a non-stoichiometric melt is used to produce BaTiO₃ single crystals. This process was originally adapted from the Czochralski method by Linz et al. and can produce higher quality single crystals with less impurities and reduced stresses within the grown crystal.⁷ The melt is typically Ti-rich to avoid the formation of the hexagonal crystal structure in BaTiO₃ (above 1440°C in stoichiometric BaTiO₃). Crystals are grown at a rate of 0.5 to 1 mm/h; boules of up to a few centimeters have been produced.⁷⁻⁹

There are some limitations to producing TSSG BaTiO₃ single crystals. Even though the impurity level in TSSG BaTiO₃ is lower compared to either Czochralski or any of the flux growth methods, rhodium and iridium contaminants are found in the growth crystals⁷ which gives the grown crystal a yellow tint. Also, extensive care is required to prevent cracking when the grown crystal is cooled through the Curie temperature.

While TSSG BaTiO₃ single crystals are also limited by production cost, textured ceramics of comparable properties and lower cost can be produced by the templated grain growth (TGG) process. In principle, poled textured ceramics have the same macroscopic symmetry as poled single crystals. Textured BaTiO₃ ceramics produced by a TGG method show improved piezoelectric responses relative to polycrystalline ceramics.¹⁰⁻¹² Wada et al. produced [110] oriented BaTiO₃ ceramics by TGG using [110] BaTiO₃ plate-like templates.¹² The authors showed a peak in the d₃₃ and -d₃₁ of 788 pC/N and 93 pC/N, respectively, for 85% textured ceramics as measured by XRD.¹²

There are several parameters that are used to characterize the textured ceramics produced by TGG. The main parameters are the orientation of the growth single crystals in the textured ceramic and the texture distribution. The March-Dollase equation, (Equation **1.1**) is used to model the effect of both of the orientation and the texture distribution function (ODF) in a textured ceramic.¹³

$$F(f, r, \theta) = f \left(r^2 \cos^2 \theta + \frac{\sin^2 \theta}{r} \right)^{-3/2} + (1 - f) \quad \mathbf{1.1}$$

where θ is the angle between the texture (orientation) axis and the scattering vector, r is the orientation parameter, and f is the volume fraction of oriented material. The orientation parameter is used to characterize the width of the orientation distribution and is normalized to the single crystal. In the normalization process, $r = 1$ for a random polycrystalline ceramic and $r = 0$ for a perfectly textured sample.¹³ The lowest orientation parameter for a textured ceramic produced by TGG approach was observed in the tape cast Sr_{0.53}Ba_{0.47}Nb₂O₆ system (Figure **1-2**) where the orientation distribution was

given as $r = 0.2$.¹⁴ In the quest to prepare single-crystal-like ceramics, improved orientation is clearly needed.

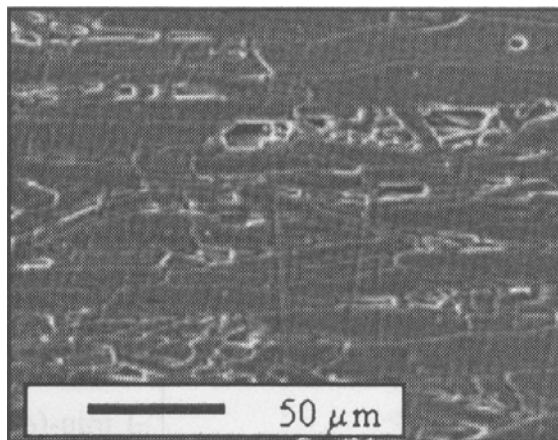


Figure 1-2: SEM image of a $\text{Sr}_{0.53}\text{Ba}_{0.47}\text{Nb}_2\text{O}_6$ microstructure fabricated by TGG.

The literature has reported that the volume fraction of oriented material in textured ceramics can approach 80 – 90% texture. The perovskite systems in which $\geq 90\%$ texture has been achieved include PMN- 67PT,¹⁵ $\text{Na}_{0.5}\text{Bi}_{0.5}\text{TiO}_3$ -BaTiO₃,¹⁶ and BaTiO₃.¹² Achieving 100% texture in TGG fabricated polycrystalline ceramics has been hindered by the misalignment of the initial templates and boundary impingement during subsequent growth on larger unconverted matrix grains.

Park and Shrout demonstrated the effects of changing the orientation in single crystal PZN- 45PT. With a 20° misalignment from the [001] direction, the strain vs. field properties were reduced by half (Figure 1-3).¹ Extrapolating this result to textured ceramics, it is clear that the overall piezoelectric response will be reduced by misalignment of the template grains. Thus, to avoid these problems, it is proposed to develop a process in which total control of the template location and orientation is achieved. Furthermore, by controlling the template distribution it is proposed that in a patterned array 100% texture, and improved piezoelectric response can be achieved.

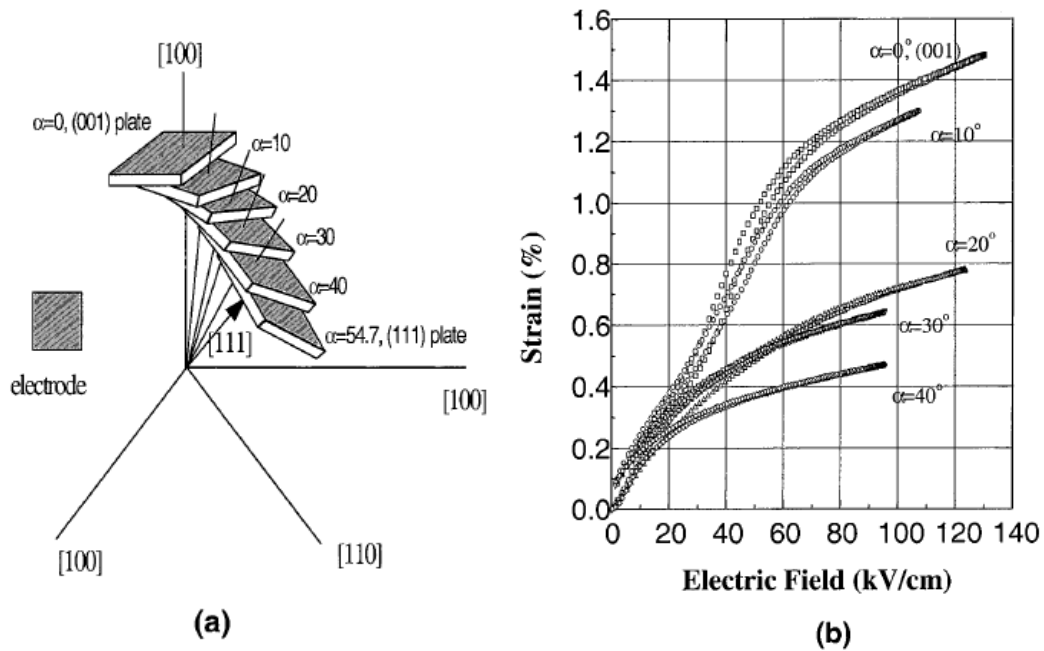


Figure 1-3: Schematic diagram (a) for sample preparation for investigating optimum crystallographic orientation and (b) strain vs. E-field behavior for PZN- 45PT crystals oriented along $[001] + \alpha$, where α is the degree of deviation from $[001]$ toward $[111]$.¹

1.2 Scientific Goals and Overview

The goal of this research program is three fold; 1) to develop a general methodology that would yield an oriented polycrystalline ceramic with unprecedented spatial and alignment control and 2) to apply the methodology to the design and fabrication of single crystal / epoxy composites of 2-2 connectivity and 3) correlate the piezoelectric properties of BaTiO_3 to the microstructure of the 2-2 composite. By designing and controlling the template / patterned features (size, shape, etc.) and placement, the amount of single crystal growth can be controlled. Thus, final microstructures with a varying amount of single crystal elements with high aspect ratios can be achieved. The objectives of the project are the following:

- To understand the factors involved in controlling local enhanced grain growth / single crystal growth while limiting matrix grain growth.
- To determine how to mediate the growth of single crystal elements by solid state conversion with metal interlayers in a 2-2 BaTiO₃ ceramic / nickel composite.
- To correlate piezoelectric properties with the scale of single crystal / epoxy composites produced by the metal – mediated TGG crystal growth process.

1.3 Organization of the Thesis

Chapter 2 introduces the crystal structure, processing and properties of BaTiO₃ and presents an overview of the available fabrication techniques for achieving textured ceramics and single crystals. Also, potential patterning approaches for the deposition of templates for texture development are briefly described. Chapter 3 presents efforts to achieve localized microstructural control by selective doping of BaTiO₃ by TiO₂ and SiO₂ in various atmosphere conditions. In Chapter 4, a process for controlling [001] and [110] solid state conversion of BaTiO₃ using patterned BaTiO₃ single crystals is outlined. Results on sustained texture development as a function of surface chemistry, crystal orientation and atmosphere are given with respect to the growth conditions obtained in Chapter 3. In Chapter 5, a metal – mediated growth process is outlined for fabricating 2-2 single crystal / epoxy composites with narrow inter-element spacings. The chapter starts with the background and fabrication of piezoelectric composites and concludes with the dielectric and piezoelectric properties of the composite structures as a function of composition and crystal orientation. Chapter 6 summarizes the thesis and proposes additional future work.

1.4 References

1. Park, S.E. and T.R. Shroud, "Ultrahigh Strain and Piezoelectric Behavior in Relaxor Based Ferroelectric Single Crystals," *J. Appl. Phys.*, **82**[4]: 1804-11 (1997).
2. Rehrig, P.W., S.-E. Park, S. Trolier-McKinstry, G.L. Messing, B. Jones, and T.R. Shroud, "Piezoelectric Properties of Zirconium-Doped Barium Titanate Single Crystals grown by Templated Grain Growth," *J. Appl. Phys.*, **86**[3]: 1657-61 (1999).
3. Ceracomp Corporation, 2008; Available from: <http://www.ceracomp.com/>.
4. Park, S.-E., S. Wada, L.E. Cross, and T.R. Shroud, "Crystallographically Engineered BaTiO₃ Single Crystals for High-Performance Piezoelectrics," *J. Appl. Phys.*, **86**[5]: 2746-50 (1999).
5. Hollenstein, E., *Preparation and Properties of KNbO₃-Based Piezoelectric Ceramics*. 2007, Ecole Polytechnique Fédérale de Lausanne. p. 143.
6. Park, S.-E., V. Vedula, M.-J. Pan, W.S. Hackenberger, P. Pertsch, and T.R. Shroud. *Relaxor Based Ferroelectric Single Crystals for Electromechanical Actuators*. in *Proceedings on SPIE's 5th Annual International Symposium on Smart Structures and Materials*. 1998. San Diego, CA.
7. Belruss, V., J. Kalnajs, A. Linz, and R.C. Folweiler, "Top-Seeded Solution Growth of Oxide Crystals from Non-Stoichiometric Melts," *Mater. Res. Bull.*, **6**[10]: 899-906 (1971).
8. MTI Corporation, *BaTiO₃: Barium Titanate Crystal*. 2008; Available from: <http://www.mtixtl.com>.
9. Surfacenet, *Barium Titanate, BaTiO₃*. 2008; Available from: http://www.surfacenet.de/html/barium_titanate.html.
10. Sato, T. and T. Kimura, "Preparation of <111> Textured BaTiO₃ Ceramics by Templated Grain Growth Method Using Novel Template Particles," *Ceramics International*, **34**: 757-760 (2008).
11. Sugawara, T., Y. Nomura, T. Kimura, and T. Tani, "Fabrication of <111> Oriented BaTiO₃ Bulk Ceramic by Reactive Templated Grain Growth," *J. Cer. Soc. Jap.*, **109**[10]: 897-900 (2001).

12. Wada, S., K. Takeda, T. Muraishi, H. Kakemoto, T. Tsurumi, and T. Kimura, "Preparation of [110] Grain Oriented Barium Titanate Ceramics by Templated Grain Growth Method and Their Piezoelectric Properties," *Jap. J. Appl. Phys.*, **46**[10B]: 7039-43 (2007).
13. Dollase, W.A., "Correction of Intensities for Preferred Orientation in Powder Diffractometry: Application of the March Model," *J. Appl. Cryst.*, **19**: 267-72 (1986).
14. Duran, C., S. Trolier-McKinstry, and G.L. Messing, "Dielectric and Piezoelectric Properties of Textured $\text{Sr}_{0.53}\text{Ba}_{0.47}\text{Nb}_2\text{O}_6$ Ceramics Prepared by Templated Grain Growth," *J. Mater. Res.*, **18**[1]: 228-38 (2003).
15. Kwon, S., E.M. Sabolsky, G.L. Messing, and S. Trolier-McKinstry, "Templated Grain Growth and Piezoelectric Properties of High Strain {001} Textured $0.675\text{Pb}(\text{Mg}_{1/3}\text{Nb}_{2/3})\text{O}_3$ - 0.325PbTiO_3 Ceramics," *J. Am. Ceram. Soc.*, **88**[2]: 312-7 (2005).
16. Yilmaz, H., G.L. Messing, and S. Trolier-McKinstry, "(Reactive) Templated Grain Growth of Textured Sodium Bismuth Titanate ($\text{Na}_{1/2}\text{Bi}_{1/2}\text{TiO}_3$ - BaTiO_3) Ceramics - I Processing," *J. Electroceramics*, **11**: 207-15 (2003).

Chapter 2

Literature Review

Barium Titanate (BaTiO_3) was chosen as a model material since it is one of the most investigated ferroelectric materials, because of its history as the first oxide ferroelectric, simple crystallographic structure, and its extensive use in the electronics and optics industries. Microstructural control and fabrication of fine grained BaTiO_3 has been investigated and employed in the multilayer ceramic capacitor industry. Textured ceramics and single crystals have been shown to increase the piezoelectric responses in BaTiO_3 , improving its prospects as a potential lead-free piezoelectric.

This chapter reviews the crystal structure of BaTiO_3 and the impact of the equilibrium phases on the dielectric properties. Following this, a review is given of BaTiO_3 processing, including fabrication of textured ceramics and single crystals, and microstructure evolution. Finally, a review on piezoelectric composites and potential approaches for patterning template particles for solid state crystal growth is given.

2.1 Background on BaTiO_3

2.1.1 Crystal Structure

Barium titanate has a perovskite-type structure. The prototype perovskite phase has barium atoms sitting at the unit cell corners, oxygen atoms at the face centers, and the titanium ion in the center of the unit cell. Figure 2-1 shows a unit cell of BaTiO_3 in the cubic phase.¹ It can be seen that the point group is $m\bar{3}m$. Thus, above the Curie temperature ($\sim 130^\circ\text{C}$ depending on doping) the structure is a non-polar, paraelectric phase.¹

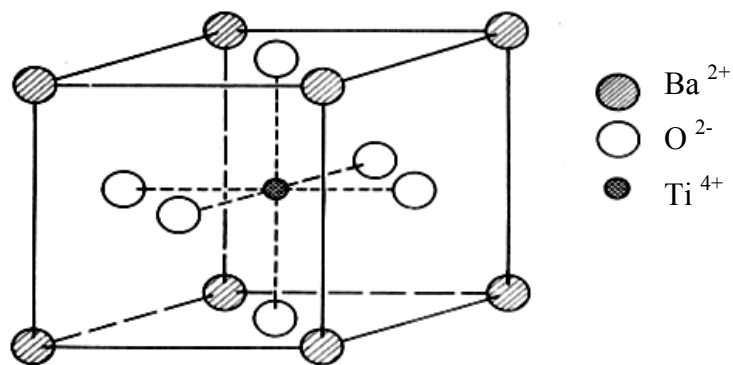


Figure 2-1: Schematic representation of the cubic BaTiO₃ perovskite unit cell.

Below the Curie temperature, the unit cell undergoes a change to a tetragonal structure (4mm point group) where one axis elongates (becomes the c-axis) while the other two directions contract. This is caused by the relative displacements of the cations (Ba²⁺ and Ti⁴⁺) with respect to the anions (O²⁻) along the [001] directions as is shown in Figure 2-2.²

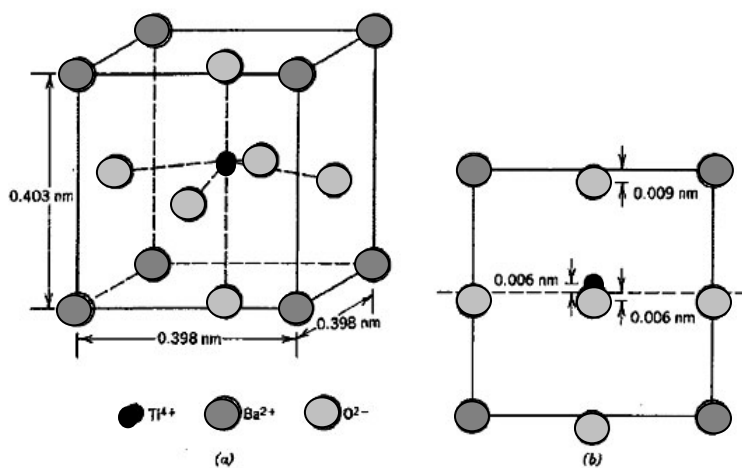


Figure 2-2: Schematic of a) a tetragonal BaTiO₃ unit cell and b) projection of the structure in the a-c plane, showing the relative displacements of the Ti⁴⁺ and O²⁻ ions.²

With further cooling, BaTiO₃ undergoes additional phase transitions to lower symmetry. Around 5°C, BaTiO₃ becomes orthorhombic (point group mm2) and a spontaneous polarization develops along the [101] directions (12 possible polar directions) with respect to the original cubic structure. Below -90°C, BaTiO₃ is rhombohedral (point group 3m) and the spontaneous polarization is along the cubic [111] directions (8 possible polar directions). Figure 2-3 shows a schematic of the phase transitions and unit cell parameters.³

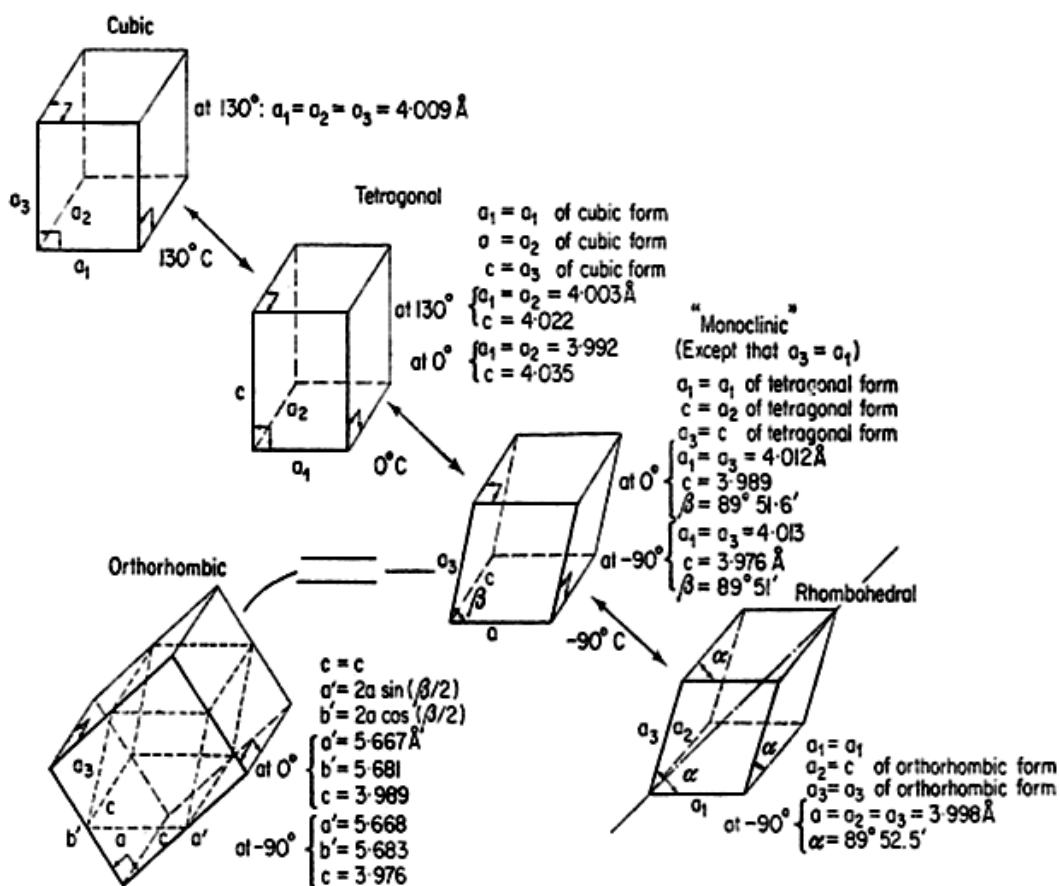


Figure 2-3: Schematic of the phase transitions and unit cell dimensions in BaTiO₃ as a function of temperature.³

In this study, both Ti-rich BaTiO_3 ($\text{Ba}/\text{Ti} = 0.996$) and $\text{Ba}(\text{Zr}_{0.05}\text{Ti}_{0.95})\text{O}_3$ were used. Figure 2-4 shows how the Curie temperature and other phase transition temperatures are influenced by the addition of different ions.³ Zr is sometimes referred to as a “pincher ion” in BaTiO_3 , since all three phase transition temperatures tend to converge. Thus, for $\text{Ba}(\text{Zr}_{0.05}\text{Ti}_{0.95})\text{O}_3$, the Curie temperature drops to 100°C , while the orthorhombic to tetragonal phase transition has shifted above room temperature. Zr was added to BaTiO_3 to increase the piezoelectric response by domain engineering $\text{Ba}(\text{Zr}_{0.05}\text{Ti}_{0.95})\text{O}_3$, as discussed in the next section.

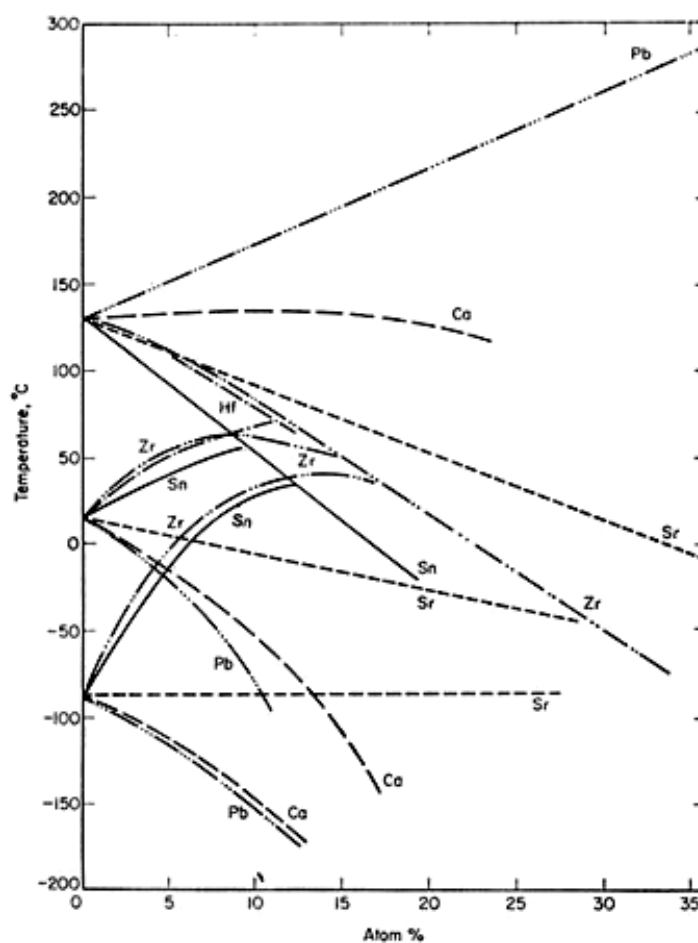


Figure 2-4: Transition temperature trends as a function of dopant in BaTiO_3 .³

2.1.2 Dielectric and Piezoelectric Properties

The electrical response of a material at the molecular and microscopic levels to an applied electric field constitutes a material's dielectric properties. The dielectric properties that are of common interest include the polarization and the dielectric permittivity and loss. These two property sets are a function of temperature and frequency in ferroelectric materials.

In general there are several different mechanisms that contribute to a material's polarization. These include electronic polarizability, ionic polarizability, dipolar reorientation, space charge polarizability, and in ferroelectric materials, domain wall movement.³ The total polarization is the sum of these individual mechanisms. The frequency dependence of the relative permittivity due to these different polarization mechanisms is shown in Figure 2-5.³

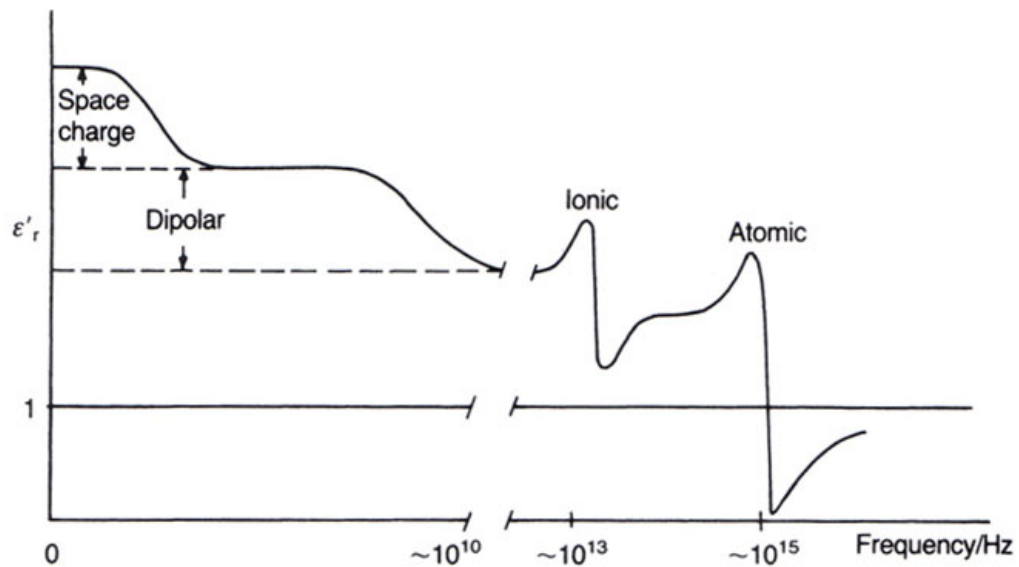


Figure 2-5: Schematic of the frequency dependence of the relative permittivity due to the different polarization mechanisms.³

The polarization (P) can be related to the relative permittivity through the electric field by Equation 2.1:³

$$P = (\epsilon_r - 1)\epsilon_o E \quad 2.1$$

where E is the electric field, ϵ_o is the permittivity of free space (8.85×10^{-12} F/m), and ϵ_r is the relative permittivity. The dominant polarization mechanism in BaTiO₃ is from dipolar reorientation. The dipoles arise from the displacement of the center Ti⁴⁺ ion from the center of the unit cell to produce a spontaneous polarization. The formation of the spontaneous polarization is discussed in more detail in Section 2.1.2.1.

2.1.2.1 Polarization

As BaTiO₃ is cooled through its Curie point, a spontaneous polarization is developed. Figure 2-6 shows the spontaneous polarization as a function of temperature for tetragonal BaTiO₃.⁴ The value for the spontaneous polarization at room temperature is around $27 \mu\text{C}/\text{cm}^2$. It is clear from Figure 2-6 that the cubic to tetragonal transition is a first order phase transition.⁴

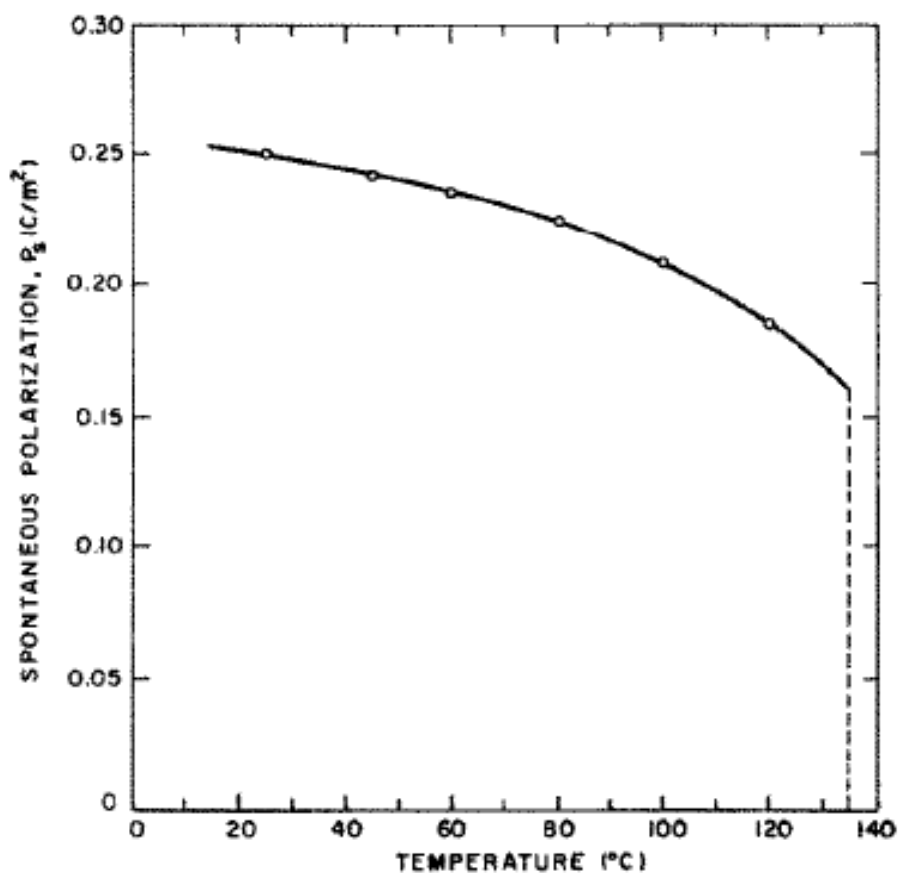


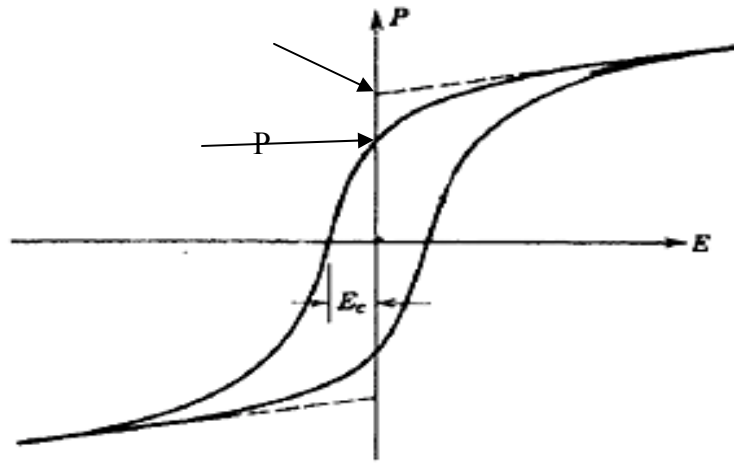
Figure 2-6: Spontaneous polarization as a function of temperature for tetragonal BaTiO₃.⁴

Upon cooling from the cubic phase, the spontaneous polarization can arise in multiple equivalent directions (any one of the 6 [001] directions). It is therefore possible to re-orient the spontaneous polarization with the application of an external electric field. If a strong alternating electric field is applied to the BaTiO₃ ceramic, a ferroelectric hysteresis loop is observed (Figure 2-7).⁵ The ferroelectric hysteresis loop results from the movement of the ferroelectric domain walls within each grain. When an electric field is applied, the domains that are aligned with the applied electric field have a lower energy; thus the domain walls move to reduce the energy of the misaligned domains. The

energy associated with the movement of the domain walls is generally smaller than that required for nucleation of new domains and the rotation of the misaligned domains.⁶

The ferroelectric domains are formed from cooling BaTiO₃ from the cubic phase to the tetragonal and lower symmetry crystal structures. Upon cooling, most grains in the BaTiO₃ ceramic will divide into a number of domains, each having a spontaneous polarization along one of the possible [001] directions in the tetragonal crystal structure. When this occurs, there are two types of domain configurations possible. The first domain configuration consists of 90° domain walls, which are related by the rotation around the normal to the {101} planes (this is the plane that is common between the two).⁶ The second domain configuration includes 180° domain walls. This domain configuration is rotated around the normal of the {100} plane. The different domain configurations are formed as a result of the reduction of stresses, uncompensated surface charges, grain boundary structure, and physical imperfections in the material.⁷

It is also possible to apply a large, uni-directional electric field when cooling through the Curie Point to effectively pole the ceramic. This causes the dipoles in the sample to align as well as possible with the applied electric field, given the constraints that the polarization will not remain rotated off its preferred direction at zero field, and that local elastic and electric fields influence the domain state. When the external electric field is removed, there remains a remanent polarization in the BaTiO₃ ceramic. Once the electric field is removed, there is some relaxation; however, most domains remain aligned. Thus there is a remanent polarization with no applied field after poling.



P_r = Remanent Polarization

P_{sat} = Saturation Polarization

E_c = Coercive Field

Figure 2-7: Schematic of a $BaTiO_3$ ferroelectric hysteresis loop on a polarization (P) vs. electric field (E) graph.⁵

2.1.2.2 Dielectric Permittivity

$BaTiO_3$ has a high dielectric permittivity that is strongly dependent on temperature, composition and crystalline perfection. Figure 2-8 shows examples of the variation in the dielectric permittivity as a function of temperature for both pure $BaTiO_3$ and $Ba(Zr_{0.05}Ti_{0.95})O_3$ single crystals.^{8,9} The $BaTiO_3$ graph is based on phenomenological calculations for single crystal $BaTiO_3$; as a result, it does not include domain wall contributions to the properties.⁸ It is clear that the dielectric permittivity is anisotropic below the Curie temperature and shows peaks at the phase transitions.

A general relationship between the polarizability of a material and the dielectric permittivity was derived by Lyddane, Sachs, and Teller (LST). This generalized approach

takes into account electronic and ionic polarizability as well as dipolar formation and re-orientation as a function of frequency. The derivation also assumes both transverse and longitudinal charge displacement, and thus can be applied to any material system and polar crystal structure.

The LST equation for the dielectric permittivity of materials is given in Equation 2.2,¹⁰ where ϵ is the dielectric permittivity of the material, ϵ_0 is the permittivity of free space, ω_t and ω_l are the transverse and longitudinal polar vibrations of charge displacement within a material from all frequencies. Since this equation is not dependent on the type of material (or crystal structure) it can be applied to ferroelectric materials.

$$\frac{\epsilon}{\epsilon_0} = \frac{\omega_l^2}{\omega_t^2} \quad 2.2$$

Baker showed that the LST equation can be derived using a classical oscillator dispersion mode (from ionic polarizability), Debye dispersion modes (from dipolar orientation polarizability) and a combination of both.¹¹ The characteristic frequencies of a given material can then be related to the ratio of $\frac{\epsilon}{\epsilon_0}$, thus the definition of LST is generalized to include all the dispersions in the dielectric response.

For $\text{Ba}(\text{Zr}_{0.05}\text{Ti}_{0.95})\text{O}_3$ only the c-axis dielectric response of the single crystal was reported by Rehrig.⁹ With the addition of zirconium, the phase transitions are shifted.

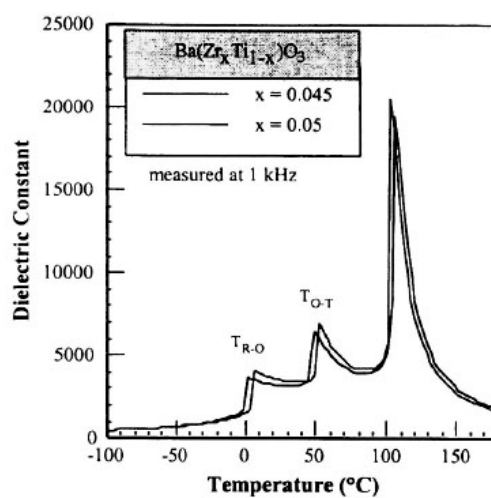
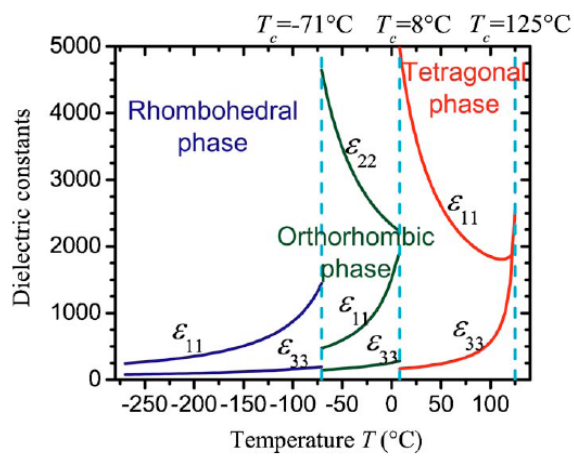


Figure 2-8: Dielectric constant as a function of temperature for both pure BaTiO_3 (ϵ_{33} , ϵ_{11} , ϵ_{22})⁸ and $\text{Ba}(\text{Zr}_{0.05}\text{Ti}_{0.95})\text{O}_3$ (ϵ_{33})⁹ single crystals.

2.1.2.3 Piezoelectricity

The piezoelectric effect in a material is a phenomenon that relates mechanical strain to electric energy. This phenomenon was first discovered in 1880 by Jacques and Pierre Curie. The Curie brothers observed that certain materials, such as quartz and Rochelle salt when subjected to a mechanical strain will become electrically polarized. Later in the following year, the Curie brothers also proved that the opposite effect was true, that on applying an external electric field the materials will deform.³ The direct and converse piezoelectric phenomena are shown in Figure 2-9; the equations describing the direct and converse piezoelectric response are given in Equation 2.3.³

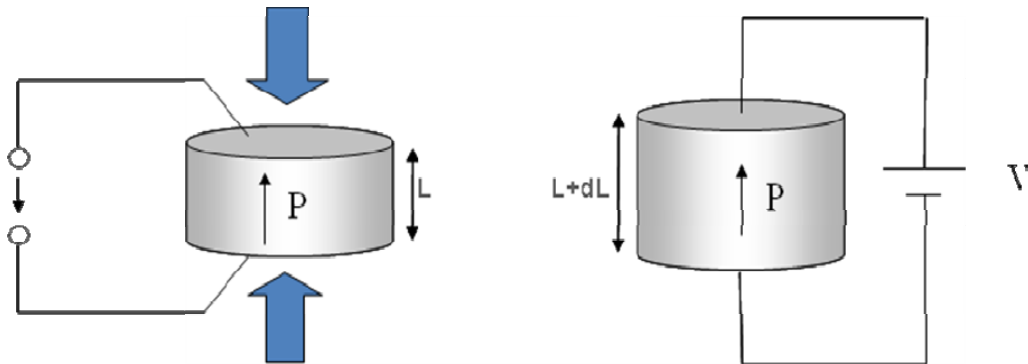


Figure 2-9: Schematic showing the a) direct and b) converse piezoelectric response. V = voltage, P = polarization direction, and L = length of the ceramic. The blue arrows denote an applied stress.

$$\frac{\partial D_i}{\partial X_{jk}} = d_{ijk}^E, \quad \frac{\partial x_{jk}}{\partial E_i} = d_{ijk}^T \quad 2.3$$

where D is the dielectric displacement, X is the stress, x is the strain, E is the electric field, and d is the piezoelectric coefficient.

The piezoelectric coefficient is anisotropic and dependent on the direction the electric field is applied and the resulting strain is measured. For a poled random ceramic, the point group becomes ∞m , and due to symmetry constraints the piezoelectric

coefficients in matrix notation can be reduced to the following: d_{33} , d_{31} (equal to d_{32}), and d_{15} (equal to d_{24}). The matrix notation is a convenient method of representing higher rank tensors (≥ 3), by reducing the number of suffixes to represent tensor properties. For example, with the piezoelectric constant, there are 27 different tensor values, however in matrix form it is reduced to 18.¹²

Du et al.¹³ investigated the anisotropy of the piezoelectric properties in [001] poled single crystal BaTiO₃. The authors calculated the d_{33} and coupling coefficient (k_{33}) for a [001] single crystal at angles from 0° – 60° away from the poled axis. The maxima in the d_{33} and k_{33} were calculated to be 47° and 52° away from the [001] direction, respectively. This was confirmed by the experimental results of the cut crystal, where the d_{33} was measured to be 250 pC/N and the k_{33} was 0.33.¹³

Additional work was completed by Wada et al.,¹⁴ where the authors took advantage of the piezoelectric anisotropy, via domain engineering.^{14, 15} There are specific angles away from the poled direction for the tetragonal and orthorhombic crystal structures in BaTiO₃ that provide optimized response. The crystal orientations needed for the tetragonal and orthorhombic phases are [111] and [001], respectively, and are schematically shown in Figure 2-10. Domain engineered ferroelectric crystals enhance the piezoelectric performance by the following three features: 1) hysteresis-free strain vs. field behavior due to the inhibition of the domain wall motion since the polarization directions of a poled crystal are all in energy equivalent states, 2) high piezoelectric constants along the non-polar direction due to tilting of the polar vectors with an applied electric field, and 3) potential change in the macroscopic symmetry in the crystals.¹⁵

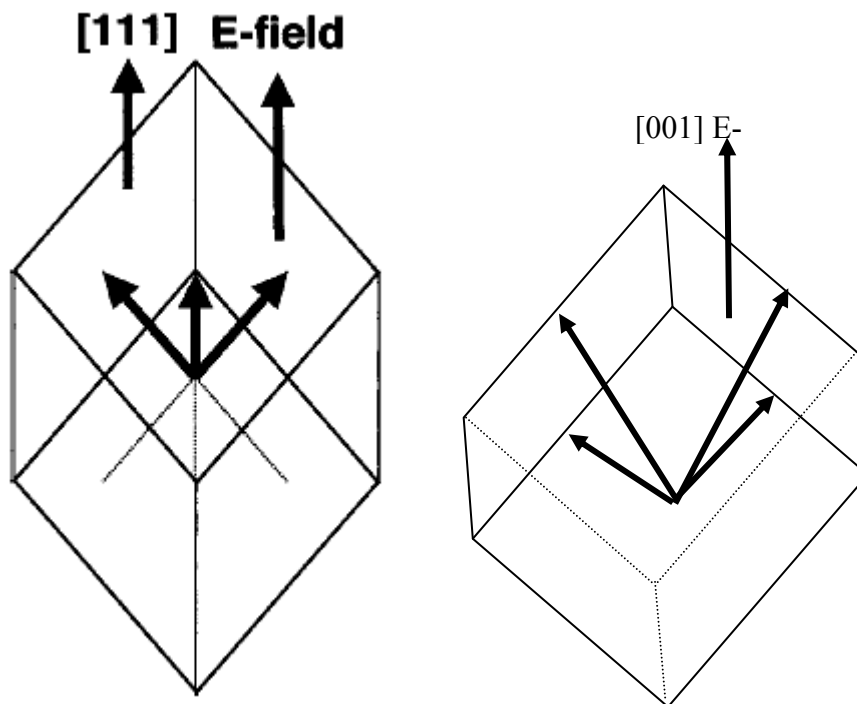


Figure 2-10: Schematic of the engineered domain states for a) tetragonal BaTiO_3 ¹⁵ and b) orthorhombic BaTiO_3 .

Due to the availability of BaTiO_3 single crystals, the $[110]$ and $[001]$ directions will be used in this study. Thus, to test the effects of domain engineering on the enhancement of the piezoelectric constants, $\text{Ba}(\text{Zr}_{0.05}\text{Ti}_{0.95})\text{O}_3$, an orthorhombic crystal structure at room temperature, will be used in combination with undoped BaTiO_3 .

2.1.3 Stoichiometry and Phase Equilibrium

Figure 2-11 shows the BaO-TiO_2 phase diagram on the Ti-rich side.¹⁶ It can be seen that there is a eutectic at 1332°C associated with the reaction of cubic BaTiO_3 and $\text{Ba}_6\text{Ti}_{17}\text{O}_{40}$. At 1350°C , above the eutectic temperature, cubic BaTiO_3 is in equilibrium with a liquid. Thus, any addition of TiO_2 to BaTiO_3 will segregate into the liquid at this

temperature. Upon cooling, $\text{Ba}_6\text{Ti}_{17}\text{O}_{40}$ forms.¹⁶ In contrast, at 1300°C , below the eutectic temperature, there is no liquid phase. In this case, if Ti is present in sufficient quantities, $\text{Ba}_6\text{Ti}_{17}\text{O}_{40}$ can be present based on the phase diagram.

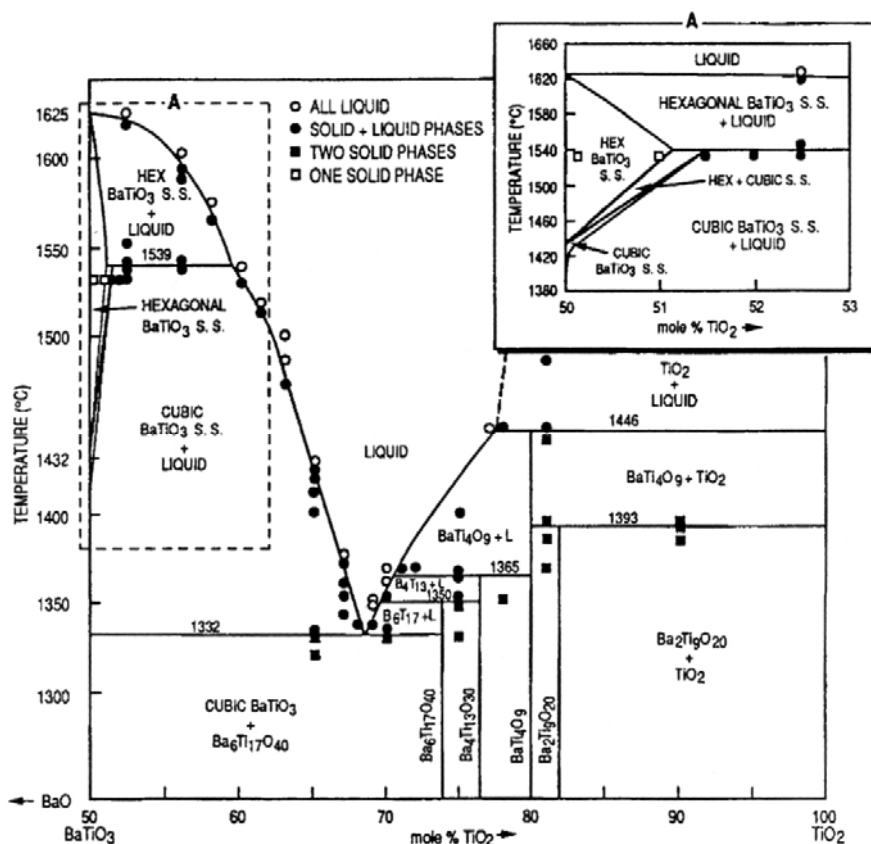


Figure 2-11: Ti-rich, BaO-TiO₂ phase equilibrium diagram.

The solubility limits of BaO and TiO₂ were studied in detail by Lee et al. for samples that were annealed for up to 50 h to achieve equilibrium.¹⁷ Figure 2-12 shows the updated BaO – TiO₂ phase diagram under ambient air conditions. It was determined that a wide solubility limit exists on the Ti-rich side of the phase diagram, centered around the 1320°C eutectic temperature, due to the higher defect formation energy for Ti vacancies compared to Ba vacancies.¹⁷ With increasing TiO₂ concentrations, both the $\text{Ba}_6\text{Ti}_{17}\text{O}_{40}$ and BaTi_2O_5 phases were identified by x-ray diffraction.

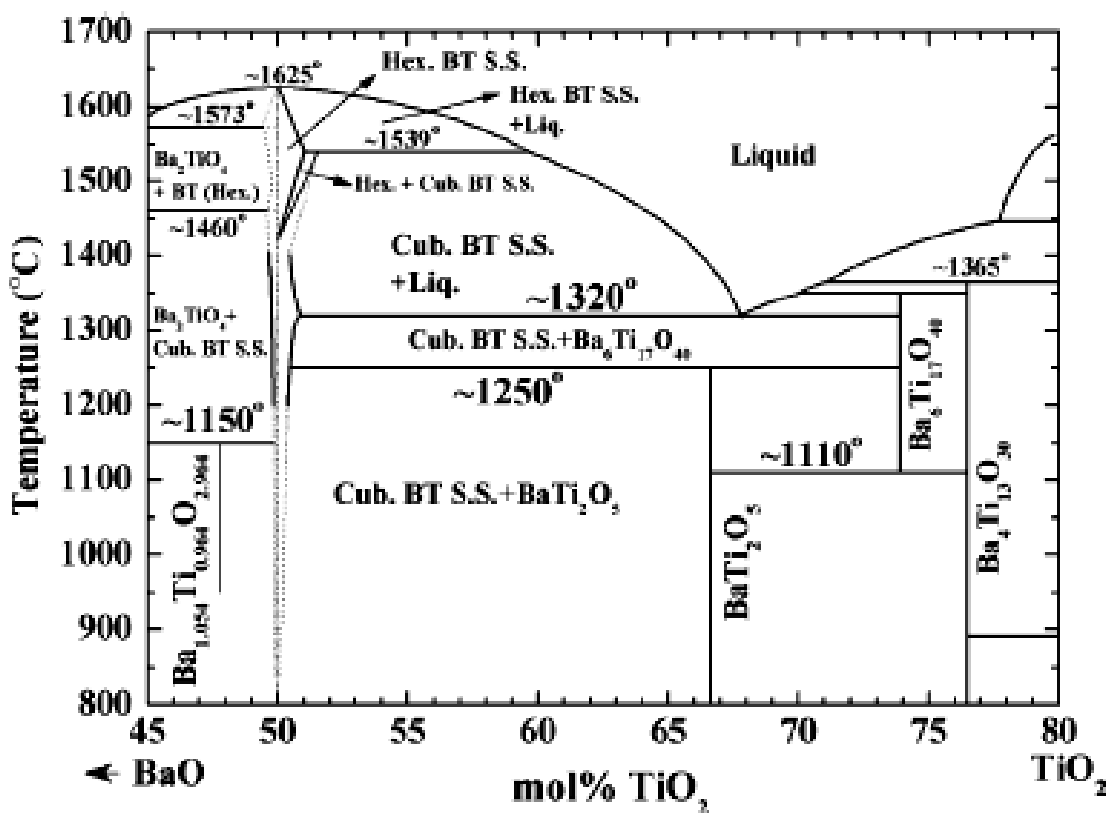


Figure 2-12: BaO – TiO₂ phase diagram under ambient air conditions. The dotted lines are extrapolated. BT S.S. = BaTiO₃ solid solution, Hex. = Hexagonal, Cub. = Cubic.¹⁷

The phase diagram for the BaO – TiO₂ – Ti₂O₃ ternary system under low PO₂ conditions of 1×10^{-15} atm and 1×10^{-18} atm was investigated by Lee et al. Figure 2-13.¹⁸ Samples were prepared with different Ba/Ti ratios by heating between 1200°C and 1350°C under various reducing conditions and slowly cooling to room temperature. XRD was used to quantify the phases present.

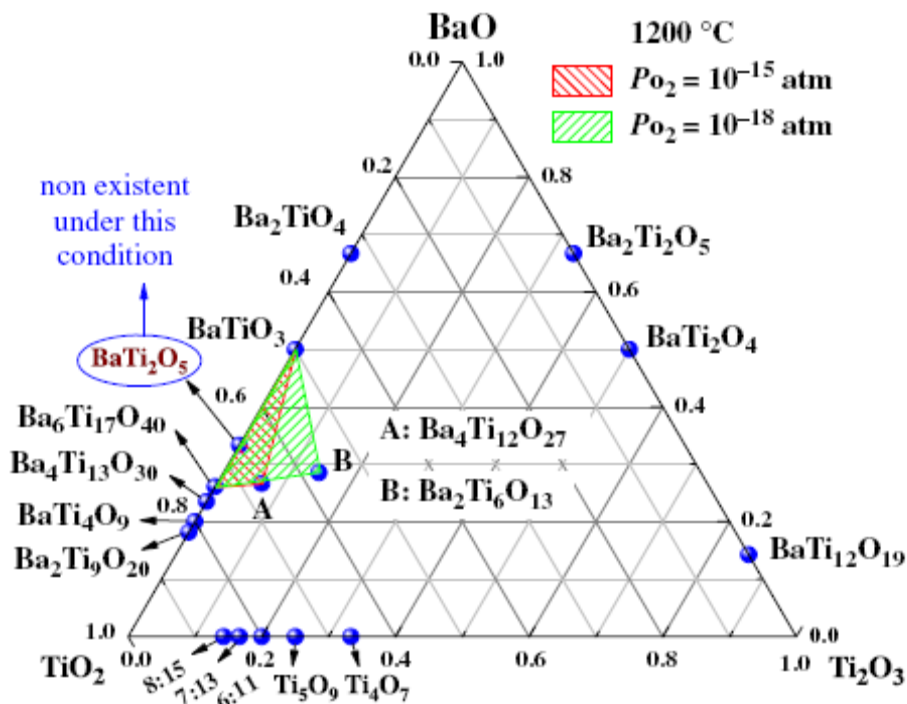


Figure 2-13: Ternary phase diagram of the BaO-TiO₂-Ti₂O₃ system under heavy reducing conditions ($P_{O_2} < 1 \times 10^{-14}$ atm) for temperatures above 1300°C.

The Ba₂TiO₄ phase is formed with Ti⁴⁺ ions and is monoclinic under heavy reducing conditions ($P_{O_2} < 1 \times 10^{-14}$ atm). Filimonov et al. found the phase to be stable under reducing conditions and at high temperatures (above 1350°C), without the presence of any Ti³⁺ ions or oxygen vacancies.¹⁸

The Ba₂Ti₆O₁₃ phase is monoclinic and contains both Ti³⁺ and Ti⁴⁺; however Filimonov et al. showed no ordering between the two different titanium ions. The authors also showed that this phase can occur in heavily reducing conditions for temperatures above 1375°C after slow cooling to room temperature.¹⁸ The hollandite phase can be either tetragonal or monoclinic depending on the barium and oxygen stoichiometry. This phase also consists of a combination of Ti⁴⁺ and Ti³⁺, with no long-range ordering present in the phases at room temperature. The hollandite phase can accommodate oxygen vacancies, and is shown to be present at room temperature with

BaTiO_{3-δ} when sintering in heavily reducing conditions at temperatures above 1380°C with Ti-excess samples.¹⁸

Lee and Randall also showed the presence of Ba₂Ti₆O₁₃ as well as Ba₄Ti₁₂O₂₇ when sintering in reducing conditions for titanium rich compositions. The phases are formed due to the reduction of Ti⁴⁺ to Ti³⁺. The Ba₂Ti₆O₁₃ phase is shown to be stable at a PO₂ ≤ 1x10⁻¹⁸ atm and the Ba₄Ti₁₂O₂₇ phase is stable at a PO₂ > 1x10⁻¹⁸ atm at 1200°C. Increasing the sintering temperature to 1350°C, both phases are stable at a PO₂ = 1x10⁻¹⁵ atm.¹⁹ To avoid the formation of some of these phases, all sintering experiments in this thesis will be done on Ti-rich BaTiO₃ in a PO₂ higher than 1x10⁻¹⁴ atm. Thus, the formation of Ba₂TiO₄, BaTi₂O₅, Ba₂Ti₆O₁₃, and the hexagonal form of BaTiO₃ should be suppressed.

For the above reasons, it is important to control the amount of excess TiO₂ used in sintering BaTiO₃. At the eutectic temperature, about 1 mol% TiO₂ can be incorporated into solid solution, however, on cooling, a second phase could be produced. This could have important implications for the resulting electromechanical properties as well as the success of TGG. Also, to avoid the formation and potential stabilization of the hexagonal crystal structure in BaTiO₃, all sintering in this thesis was performed in an oxygen atmosphere above PO₂ of 1x10⁻¹⁴ atm.

2.2 Synthesis

2.2.1 Single Crystals

It was shown in Chapter 1 that in many cases, single crystals of ferroelectric materials have improved properties relative to polycrystalline samples of the same composition. For BaTiO₃, there are several methods of producing single crystals. High temperature synthesis routes including flux growth and floating-zone methods utilize off-stoichiometric melts. BaTiO₃ single crystals cannot be grown from a stoichiometric melt because the hexagonal to cubic phase transition around 1440°C (Figure 2-11) results in

cracking of the crystals when cooled.¹⁶ Thus off-stoichiometric methods are used, so that solution growth can be accomplished below the hexagonal to cubic transition temperature (1440°C).

Remeika was the first to grow BaTiO₃ single crystals by the flux growth method.²⁰ This method is based on the eutectic reaction in the BaTiO₃ – KF system. Remeika combined powders of BaTiO₃, KF and a small amount of Fe₂O₃, heated the mixture to 1200°C and then cooled to 900°C. The remaining flux material was removed and the BaTiO₃ crystals were then cooled to room temperature.²⁰ Remeika BaTiO₃ single crystals are typically crystal plates of a triangular shape, with a thickness ranging from a few tenths of a millimeter to a few millimeters. The hypotenuse of the triangular plates are parallel to the pseudocubic [110] and the sides parallel to the [100] directions. When the crystallization occurs at 1000°C or above, {111} twin planes form.¹ These twin planes are typically from a single hexagonal stacking fault. However, when the temperature for crystallization occurs below 1000°C, no stacking faults (twins) are present. The twins form from the reduction of the stress / energy of the system when the sample begins to crystallize at too high a temperature.¹

Brown and Todt used the floating zone method to produce single crystals of BaTiO₃ containing 1.5% SrTiO₃.²¹ This mixture of BaTiO₃ and SrTiO₃ forms the cubic phase directly, avoiding the hexagonal phase. This eliminates the occurrence of cracking from the hexagonal to cubic phase change in pure BaTiO₃. Using this approach the authors fabricated BaTiO₃ single crystal boules 2.5 cm in length and 0.32 cm in diameter.

The top-seeded solution growth (TSSG) method is also used to produce BaTiO₃ single crystals from a non-stoichiometric melt. This process was originally adapted from the Czochralski method by Linz et al. and yields higher quality single crystals with less impurities and reduced stresses within the grown crystal.²² The melt is typically Ti-rich to avoid the formation of the hexagonal crystal structure in BaTiO₃ (above 1440°C in stoichiometric BaTiO₃). Crystals are grown at a rate of 0.5 to 1 mm/h; boules of up to a few centimeters have been produced. However, rhodium and iridium contaminants are present in the grown crystal.²²

Another technique that is used to produce BaTiO₃ single crystals relies on exploiting abnormal grain growth in the BaTiO₃ – SiO₂ or BaTiO₃-TiO₂ system. Yoo et al. used 1 mol% SiO₂ as a liquid phase former on the surface of a BaTiO₃ ceramic to initiate exaggerated grain growth to produce large BaTiO₃ single crystals.²³ They heated the compact at 1370°C for up to 80 h to fabricate a 1.5 cm sized BaTiO₃ single crystal. Saldana et al. produced single crystals by the addition of SiO₂ on the surfaces of green BaTiO₃ compacts.²⁴ The samples were sintered at 1260°C for up to 20 h to produce BaTiO₃ single crystals up to 5 mm on a side. Complete sample dimensions were not given. Both Yoo et al. and Schneider et al. observed trapped porosity and {111} twins in the grown single crystals.

Lee et al. proposed a two step sintering and annealing process to produce large BaTiO₃ single crystals from a Ti-rich matrix by secondary abnormal grain growth (SAGG).²⁵ Initial BaTiO₃ compacts were sintered in air to 1365°C, where a few abnormal grains were produced in the sintered ceramic. The second annealing step consisted of heating the sample to 1355°C for up to 100 h to promote the growth of the abnormal grains without nucleating any additional abnormal grains from the matrix. The BaTiO₃ single crystals reached 2 cm, but contained {111} double twins in the center of the crystal.

Another technique for producing BaTiO₃ single crystals is Templated Grain Growth. In this method, a single crystal “template” is placed in contact with a sintered polycrystalline BaTiO₃ matrix and then heated to migrate the single crystal boundary into the matrix. Yamamoto and Sakuma bonded a BaTiO₃ single crystal to a Ti-rich polycrystalline matrix at 1200°C for 2 h with 1.5 MPa.²⁶ The assembly was then heated to 1300°C for 30 h and a 3 x 3 x 0.5 mm BaTiO₃ single crystal was produced. The authors annealed below the eutectic temperature to avoid any abnormal grain growth from the matrix; however after 30 h the matrix grains were ~ 100 μm. The large matrix grain size, the lower temperature, and the inclusion of about 2% porosity hindered the single crystal boundary growth. In spite of this, a rate of 50 μm/h was measured.

Rehrig et al. produced millimeter sized single crystals of BaTiO₃²⁷ and Ba(Zr_{0.05}Ti_{0.95})O₃⁹ from a Ti-rich matrix using either BaTiO₃ or SrTiO₃ single crystal

templates. The samples were heated to 1350°C for up to 10 h and the growth rates for [111], [001], and [110] single crystals into a BaTiO₃ matrix were 590 – 790 μm/h, 180 – 350 μm/h, and 42 – 59 μm/h, respectively. Rehrig et al. also reported that the [111] and [001] crystal boundary became faceted and the growth rates were reduced to ~ 30 μm/h when the facet formed (Figure 2-14).²⁷ The grown single crystals were stoichiometric but contained a large amount of trapped porosity. The piezoelectric constant (d_{33}) at room temperature and 1kHz, and the remanant polarization of the grown crystals were 140 pC/N and 12 μC/cm² for the BaTiO₃ crystal and 330 pC/N and 13 μC/cm² for the Ba(Zr_{0.05}Ti_{0.95})O₃ respectively.²⁸

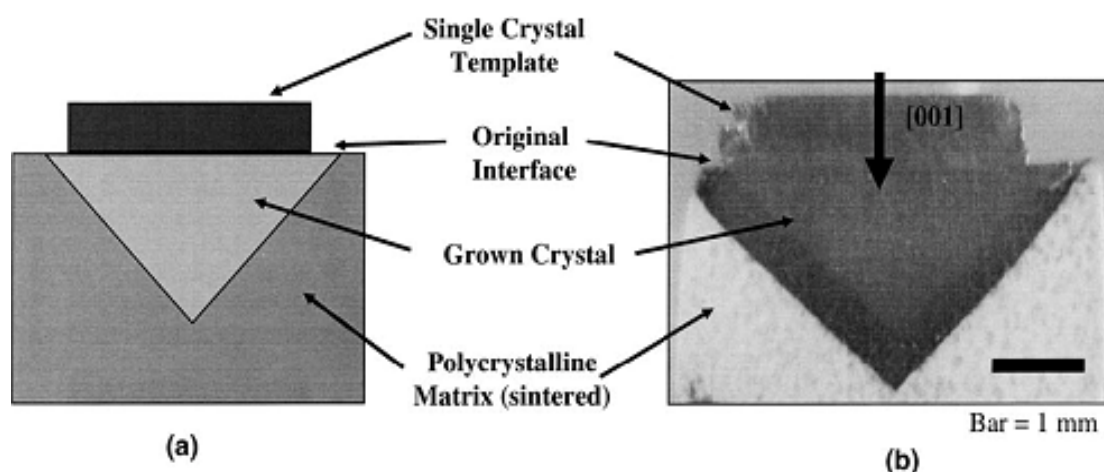


Figure 2-14: a) Schematic and b) optical image showing the faceted planes of the grown single crystal in polycrystalline BaTiO₃ from a [001] BaTiO₃ single crystal.²⁷

Unlike most single crystals prepared by flux growth, TSSG produced samples that do not necessarily have twin planes but include impurities in the final crystal. Using a doped BaTiO₃ or exploiting exaggerated grain growth can achieve single crystal samples with large dimensions, but the control over the final orientation is dependent on the starting grain's orientation. TGG approaches for fabricating BaTiO₃ single crystals are cost effective, and final control over the orientation of growth is possible. However one of the major drawbacks is the trapped porosity from the conversion of the matrix grains.

In this thesis, TGG will be employed for controlling oriented growth in BaTiO_3 , and the issues with this process will be considered.

2.2.2 Textured Ceramics

One of the methods for producing textured ceramics is Templated Grain Growth (TGG). TGG takes advantage of the preferred growth of large, oriented particles in a dense polycrystalline matrix. Initially, a few volume percent of “seed” templates are randomly dispersed in a matrix of relatively finer equiaxed particles. Alignment of the templates is typically done using shear forces during tape casting. After the cast tapes are densified, grain growth conversion from the seeded templates occurs with subsequent heating. A schematic of the alignment of templates by tape casting and the texture development during the heat treatment is shown in Figure 2-15.²⁹

Green Forming and Template Alignment

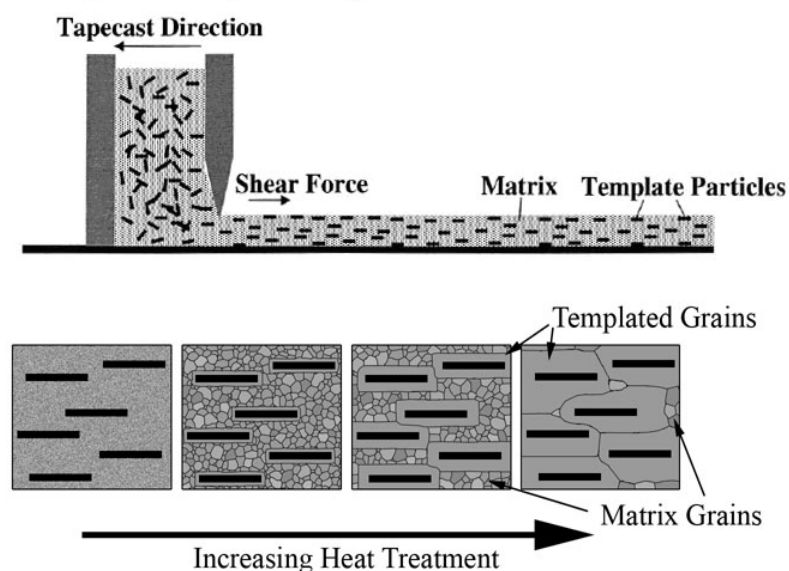


Figure 2-15: Schematic of the alignment of templates by tape casting and the texture development during the heat treatment.

There are a few criteria that are important in choosing a suitable template particle for TGG. The templates must possess a similar crystal structure to that of the matrix material and have minimal lattice mismatch between the templates and the single crystal phase being converted at the bonding and nucleation temperatures to satisfy conditions for epitaxy. The templates must have a high aspect ratio in order to be aligned during the tape casting process. Also, the templates must be thermodynamically stable at the nucleation temperature to prevent dissolution of the templates before TGG can occur.²⁹ The criteria are also similar for the top seeded TGG process outlined above.

One of the earlier works in texturing BaTiO₃ was completed by Ohara et al., where c-axis oriented BaTiO₃ fibers were used.³⁰ Only BaTiO₃ needle-like fibers were used when fabricating the compacts, and after sintering the density reached only 70% theoretical density. However, the texture fraction was roughly 27% and the measured d_{33} was 270 pC/N, an increase of 1.7 times the polycrystalline value (155 pC/N). The piezoelectric measurement was performed on a poled BaTiO₃ compact and measured by applying a load with fixed weight and recording the amplified charge generated on the surfaces of the poled specimen. The piezoelectric measurement, is however, suspect due to the extremely low density of the final compact, since it has been shown that the piezoelectric response is lowered with trapped porosity in the sample.¹

Kimura et al. used Ba₆Ti₁₇O₄₀ templates to induce <111> texture in BaTiO₃.³¹ The authors fabricated the BaTiO₃ compacts by tape casting with either 0.5 μm or 0.1 μm equiaxed grains. The samples were fired in air at 1300°C for up to 20 h; texture developed in the 0.1 μm samples but not in the 0.5 μm powder size samples. The final textured microstructure had a texture fraction of 79% (measured by XRD Lotgering factor). Kimura et al. indicated that a smaller starting equiaxed grain size and a density of >90% is required for texture development. Rehrig et al. produced millimeter sized single crystals of BaTiO₃ and Ba(Zr_{0.05}Ti_{0.95})O₃ by TGG using a ceramic with a starting grain size of 2 μm.^{9,28}

Wada et al. produced [110] oriented BaTiO₃ ceramics by TGG using [110] BaTiO₃ plate-like templates and measured the piezoelectric properties.³² The samples ranged from 0 – 100% template loading with starting BaTiO₃ powders ranging from 100

nm to 500 nm in size. With increasing template loading, the percent texture increased to 98% (by XRD analysis) but the density dropped to 90% of theoretical density (with only templates). When using either the 300 nm or the 100 nm BaTiO₃ powder, the percent texture decreased to 80%, but the density of the ceramics reached 98.6% of theoretical density. However, with a combination of both grain sizes (300 nm and 100 nm) the density stayed at ~96% theoretical density and was independent on template loading. The authors showed a peak in the d_{33} and $-d_{31}$ of 788 pC/N and 93 pC/N respectively for the 85% textured ceramics. Below and above this value the piezoelectric constants decreased; the authors did not give a reason for the peak at 85% texture.

Sato and Kimura produced textured [111] BaTiO₃ ceramics from [111] BaTiO₃ templates made by a molten salt synthesis from Ba₆Ti₁₇O₄₀.³³ Ceramic tapes were cast with 20 – 40 wt% template loading with equiaxed BaTiO₃ powder. After sintering to 1300°C for 50 h and then 1400°C for 2 h, a final microstructure with 66% texture and 96% theoretical density was fabricated for the 20 wt% template loading. With higher template loadings, the degree of texture dropped to 32% and the density to <90% of theoretical density. This trend was caused by the higher amount of templates impeding the full evolution of texture in the sintered ceramics. No dielectric or piezoelectric properties were measured.

A related process is reactive templated grain growth. The main difference is that rather than using BaTiO₃ powder, a mixture of BaCO₃ powder and templates is tape cast. Sugawara et al. used Ba₆Ti₁₇O₄₀ as templates. These were reacted with BaCO₃ powder to form [111] oriented BaTiO₃.³⁴ A 1:11 molar ratio of templates to barium carbonate was used and the compacts were sintered at temperatures from 1250°C – 1400°C. The percent texture, measured by XRD, ranged from 27% to 80% with increasing temperature. However, the highest density achieved was only 81% theoretical density for the 80% textured sample. The dielectric and piezoelectric properties were not measured due to the low sample density.

Sato et al. used a similar approach in which [001] TiO₂ needle templates were tape cast in a BaCO₃ powder matrix.³⁵ The compacts were calcined at 800 – 1200°C for 5 h then sintered at 1350°C for up to 10 h in air to form [110] oriented BaTiO₃. The final

microstructure consisted of 50 μm grains with 73% texture, calculated by XRD pole figures, and was 93% of theoretical density. No dielectric or piezoelectric properties were measured.

So, for fabricating textured or single crystal samples by the TGG method, there are several factors to consider. First a relatively high starting density is needed for the TGG of the matrix material. Generally speaking, the density should be above 90% theoretical density; however, any remaining porosity within the matrix is typically retained in the final converted single crystal. Thus care must be taken to reduce the amount of remaining porosity within the final single crystal.

For textured BaTiO_3 samples with high final density and a high texture fraction, the piezoelectric responses are improved over randomly oriented ceramics. However, the reported degrees of texture ranged from 30 - 90%. Also, in processing the textured ceramics, it is important to include some equiaxed grains with the template particles to increase the final overall density of the compacts. Typically 20 - 40% solids loading for templates are used. The main drawbacks, as mentioned in Chapter 1 are incomplete texture development and/or low final densities.

2.3 Microstructure Evolution

2.3.1 Sintering / Normal Grain Growth

Depending on the stoichiometry (Ba/Ti ratio), temperature, and atmosphere conditions, barium titanate can densify and sinter via either solid state sintering or liquid phase sintering. These two processes have different densification mechanisms, each having its own positive and negative attributes. These will be described with reference to a slightly titania rich barium titanate sample.

Below the 1332°C eutectic temperature, the material sinters by solid state diffusional processes. A typical microstructure of barium titanate sintered by solid state (Figure 2-16)³⁶ shows trapped porosity. Trapped pores are impossible to remove without

resorting to extensive grain growth for long times at high temperatures. This is one of the drawbacks of sintering barium titanate by solid state sintering. Abnormal grain growth is also seen when sintering BaTiO_3 below the eutectic temperature.³⁶

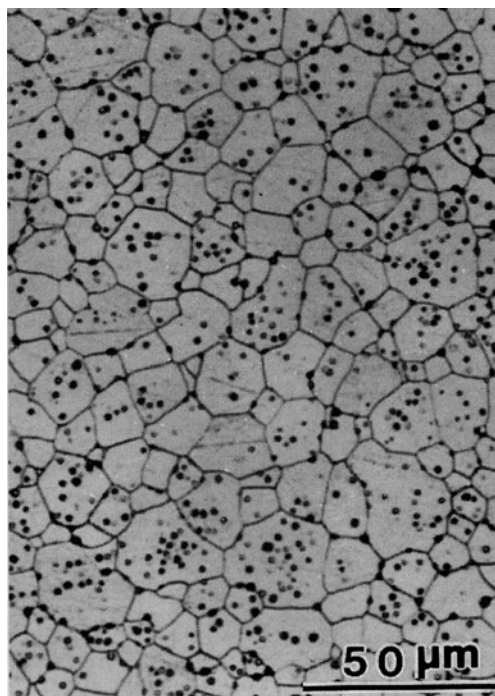


Figure 2-16: Micrograph of solid state sintered BaTiO_3 in air at 1300°C .³⁶

When the sintering temperature is increased above the eutectic temperature, a liquid phase forms and changes the dominant mechanism for densification of barium titanate. The relative amount and the effect of the liquid phase on the sintering process are governed by the solubility limits of BaTiO_3 . The solubility of the Ti ions and the amount of liquid formed is governed by either how much excess TiO_2 was added to the original barium titanate powder, or the starting stoichiometry.³⁷ It has been determined that a minimum range of 0.1 – 0.4 mol% TiO_2 is sufficient to homogeneously wet the barium titanate powder along the grain boundaries (this corresponds to roughly 6 – 13 vol% liquid).³⁸ During the intermediate sintering stage, the dominant densification mechanism is the dissolution – precipitation reaction of the barium titanate powders; the driving force for this process is a function of the solubility of the material. Liquid phase

sintering is much faster compared to solid state sintering because the diffusion coefficients are on the order of $10^{-4} - 10^{-6} \text{ cm}^2/\text{s}$ at $\sim 1200^\circ\text{C}$ compared to $10^{-8} - 10^{-12} \text{ cm}^2/\text{s}$, respectively.⁵

When fired in air, the amount of grain growth is usually much greater for liquid phase sintering than solid state sintering. Also, depending on the atmosphere and composition, abnormal or exaggerated grain growth occurs more readily in liquid phase sintered systems. A typical microstructure of a liquid phase sintered sample is shown in Figure 2-17.³⁸

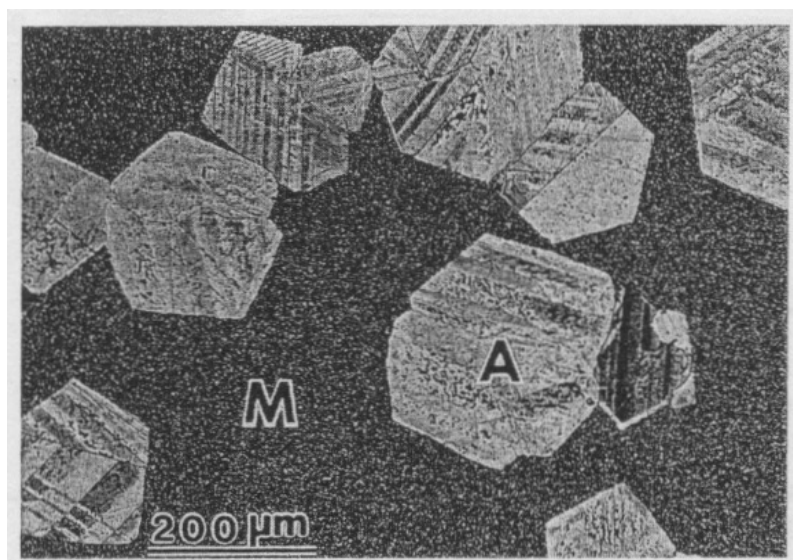


Figure 2-17: Micrograph of BaTiO_3 sintered via liquid phase sintering. The area marked M is the matrix grains ($\sim 1\mu\text{m}$), and the area marked A are the abnormal grains.³⁸

2.3.2 Exaggerated Grain Growth by Doping

Dawson et al. investigated the effect of BaTiO_3 stoichiometry on microstructure evolution in hydrothermally derived powders.³⁹ Both Ti-rich ($\text{Ba}/\text{Ti} = 0.99$) and Ba-rich ($\text{Ba}/\text{Ti} = 1.03$) powders were investigated. To adjust the stoichiometry, either barium hydroxide was added or barium was leached from the surface of the powders in HNO_3 . The resulting microstructures showed exaggerated grain growth in both Ba-rich and Ti-

rich samples. The exaggerated grain growth was attributed to either the Ti-rich amorphous layer on the surface of the leached powders, or the Ti-rich core of the barium excess powder. When sintering above 1332°C, the formation of exaggerated grain growth regions was caused by the Ti-rich liquid phase present (Figure 2-11). For Ba/Ti = 1.0, no liquid phase was formed during sintering and so exaggerated grain growth was absent.³⁹

Rios et al.³⁸ studied the effect of TiO₂ on BaTiO₃ microstructure. They added 0.1 – 0.4 mol% excess TiO₂ and sintered at temperatures ranging from 1310 – 1350°C (below and above the eutectic temperature). The final microstructures showed the presence of exaggerated grain growth at each sintering condition, with final grain sizes of 100 μm in a matrix of 1 μm grains. They showed that with increasing temperature or increasing TiO₂ concentration, the amount of exaggerated grains present increased. Kang et al. further studied the exaggerated grains formed below and above the eutectic temperature.^{40,41} For samples sintered in air below the eutectic temperature, the exaggerated grains were faceted and contained {111} twin lamellae, while the matrix grains did not coarsen. For sintering temperatures above 1332°C, exaggerated grain growth was present without the {111} twin lamellae. They also showed that as the grain boundaries of the exaggerated grains changed from faceted to a rough (rounded) structure, the additional growth of the exaggerated grains was retarded while the matrix grains coarsened during additional heat treatments.

Matsuo and Sasaki showed the presence of exaggerated grain growth in BaTiO₃ with the presence of 0.0167 mol % of Al₂O₃, 0.0375 mol % of SiO₂, and 0.0125 mol % of TiO₂.⁴² They reported that the eutectic temperature was lowered to 1240°C. The presence of the exaggerated grain growth was caused by the formation of the liquid phase during sintering. Kumar et al. observed that adding Bi₂O₃ to BaTiO₃ reduces the sintering temperature to 800°C to form pellets with 90% theoretical density and a fine grained (~ 0.2 μm) microstructure.⁴³ With increasing temperature, exaggerated grain growth was evident from liquid phase sintering.

2.3.3 Atmosphere Control

Additional microstructural control can be achieved by adjusting the oxygen partial pressure during sintering. Jung et al. studied the effect of excess Ti in BaTiO₃ compacts that were sintered in H₂ and in air.⁴⁴ The 0.4 mol% TiO₂ doped BaTiO₃ compacts were sintered in H₂ for times ranging from 30 min to 10 h, and then heated to 1250°C or 1350°C in air for times up to 100 h. Samples sintered in H₂ for 30 min showed abnormal grain growth when heated in air to either 1250°C or 1350°C. The 1250°C samples showed exaggerated grains with {111} twins, while the 1350°C samples showed exaggerated grains without any {111} twins. This observation was associated with the change from solid state sintering to liquid phase sintering. However, the samples that were sintered in H₂ for 10 h showed no exaggerated grains when sintered at 1250°C or 1350°C for times up to 100 h. This indicated that abnormal grain growth can be suppressed even for prolonged sintering times in a reducing environment.

S.-J. Kang et al.⁴⁵ observed several microstructural regions in 0.1 mol% TiO₂ doped BaTiO₃ through PO₂ ranges of 0.2 atm to 4x10⁻¹⁸ atm when sintering below 1332°C. At PO₂ = 0.2 atm, {111} twin lamellae were present in the exaggerated grains. As PO₂ decreased below 1x10⁻¹¹ atm, the formation of the {111} twins was inhibited but exaggerated grain growth still occurred. From PO₂ = 1x10⁻¹¹ atm to 1x10⁻¹⁷ atm, grain growth and exaggerated grain growth was stagnant, while below 1x10⁻¹⁸ atm exaggerated grain growth appeared but without {111} twins. The grain growth regions were attributed to the change in the driving force for grain growth caused by the change from a faceted to a rough grain boundary, shown in Figure 2-18⁴⁶ (rough) and Figure 2-19⁴⁶ (faceted).

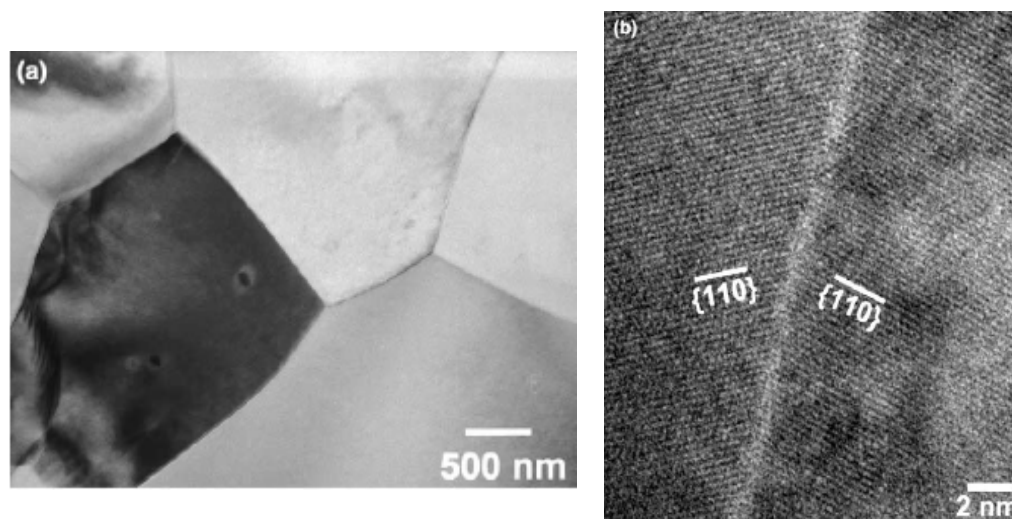


Figure 2-18: TEM images of a) low magnification image and b) high resolution image of grain boundaries in 0.4 mol% BaTiO₃ sintered at 1300°C for 8 h in H₂ after 1250°C for 30 min in H₂.⁴⁶

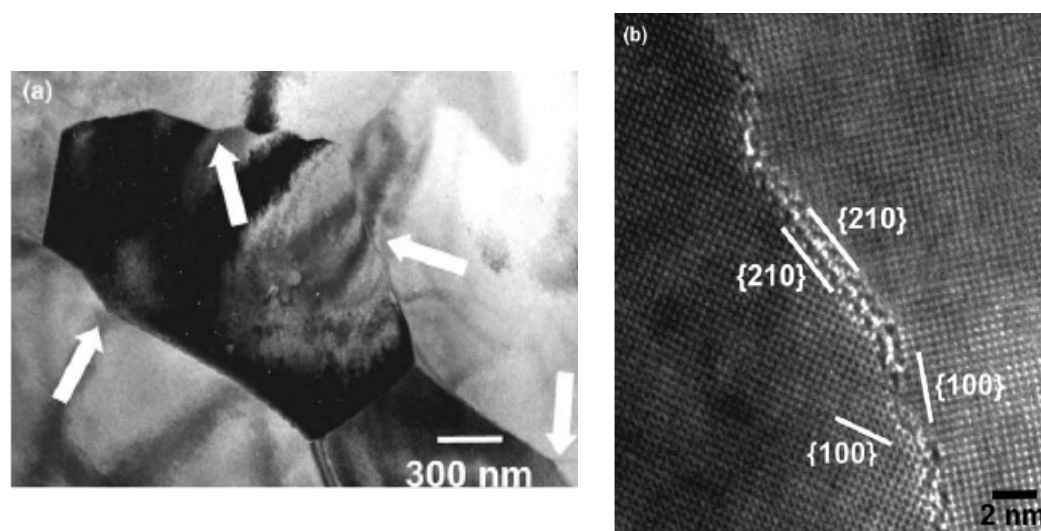


Figure 2-19: TEM images of a) low magnification image and b) high resolution image of grain boundaries in 0.4 mol% BaTiO₃ sintered at 1300°C for 8 h in air after 1250°C for 30 min in H₂.⁴⁶

Polotai et al. utilized a sintering approach combining rapid-rate sintering, rate-controlled sintering, and two-step sintering under a controlled atmosphere to produce dense nanocrystalline BaTiO₃ compacts.⁴⁷ With increasing PO₂ during sintering, the average grain size increased from 150 nm to 300 nm, while the relative density of the samples decreased. There was an inflection point in the theoretical density vs. atmosphere graph at a PO₂ of 1×10^{-13} atm, where the density was the highest with modest grain growth occurring. The relative density peaked at a heating rate 1000°C/h, while the average grain size continued to drop with increasing heating rate. For final stage sintering, the driving forces for grain boundary controlled densification and grain boundary controlled grain growth were exploited. Full density was achieved by dropping the sintering temperature to 1100°C and holding for up to 7 h after the BaTiO₃ compacts reached 94% of theoretical density.

2.3.4 Grain Growth Inhibition

Another technique to control the final grain size, other than changing the sintering profile and atmosphere, is by doping. Rahaman and Manalart studied the grain growth behavior of BaTiO₃ with Nb⁵⁺, La³⁺, and Co²⁺ dopants.⁴⁸ For the case of 0.5 at% Co²⁺ dopant, the primary mechanism of grain growth inhibition in BaTiO₃ is caused by the segregation of the doping ion to the grain boundaries. Increasing the concentration of Co²⁺ reduces the grain boundary mobility up to 50 times compared to undoped BaTiO₃. This reduction is caused by the solute drag effect.⁴⁹ Chiang and Takagi⁵⁰ also showed the segregation of acceptor dopants to grain boundaries in BaTiO₃ and SrTiO₃ and related the reduction in grain boundary mobility to the solute drag effect. Rahaman and Manalart showed that there was an increase in the concentration of titanium vacancies in BaTiO₃ with 0.3 – 0.5 at% Nb⁵⁺ doping. The titanium vacancies segregate to the grain boundaries, thus reducing the boundary mobility.⁴⁸

Brzozowski and Castro studied the effects of 0.15 at% Nb⁵⁺ doping in BaTiO₃ by electron paramagnetic resonance (EPR).⁵¹ With incomplete Nb⁵⁺ incorporation into the BaTiO₃ lattice (small concentrations of Nb⁵⁺) enhanced grain growth was observed. The

grain growth enhancement was attributed to the electronic compensation from the incorporation of Nb^{5+} ions. With increasing Nb^{5+} concentration, grain growth was inhibited. EPR results on these samples indicated that an increase in titanium vacancies resulted in the decreased grain boundary mobility, similar to what Rahaman and Manalert proposed.

Chan et al. doped BaTiO_3 with Nb^{5+} concentrations ranging from 0.25 – 6 mol%.⁵² The authors showed that grain growth was inhibited in high Nb^{5+} concentration samples. They also reported that grain growth was inhibited when the major defect compensation mechanism changed from electrons to titanium vacancies. They observed that the best dopants to limit grain growth in BaTiO_3 needed to be of a different valency than the host material, and that ionically compensated defects were the ideal grain growth inhibitors.

Grain growth inhibition is most commonly used in the multilayer ceramic capacitor industry (MLCC). For the MLCC applications, the resulting capacitors must possess a temperature stable, large dielectric response. Undoped BaTiO_3 , as shown in Figure 2-8, does not fit this criterion. There are two main factors that are used to promote a flat temperature response in the dielectric permittivity: 1) small grain sizes, and 2) chemical inhomogeneity. So, BaTiO_3 is typically doped with a combination of materials, such as iron, silica, magnesium, yttrium, holmium, dysprosium, etc. The exact compositions are company specific and are proprietary. The general result is typically a small grain size with a core-shell structure. The inside “core” is pure ferroelectric BaTiO_3 , while the “shell” is a heavily doped paraelectric BaTiO_3 phase.

2.4 Patterning Techniques

There are several different techniques that can be employed to produce a pattern on the surface of a ceramic for use in controlling the spatial placement of templates. Yin et al. demonstrated a method of selectively depositing colloids on the surface of a sintered ceramic.⁵³ By a combination of optical lithography and dry etching the surface, the ceramic was patterned. Then by capillary action, monodisperse spherical colloids

were deposited into the etched area. Figure 2-20 shows some of the various designs developed. This process produces a high degree of uniformity and control over the location of the colloids deposited on the surface with few defects (missing colloids). However, the main issue is that this method has only been successfully applied to spherical particles and not plate-like or needle-like particles.

As stated in Chapter 1, the careful control of the templates is required to optimize texture, as well as to maintain the exact spacing and location of each template site to produce high aspect ratio textured grains. Typically, the templates used are plate-like in nature, and due to the anisotropy associated with the elongated platelets, controlled deposition by this method is difficult.

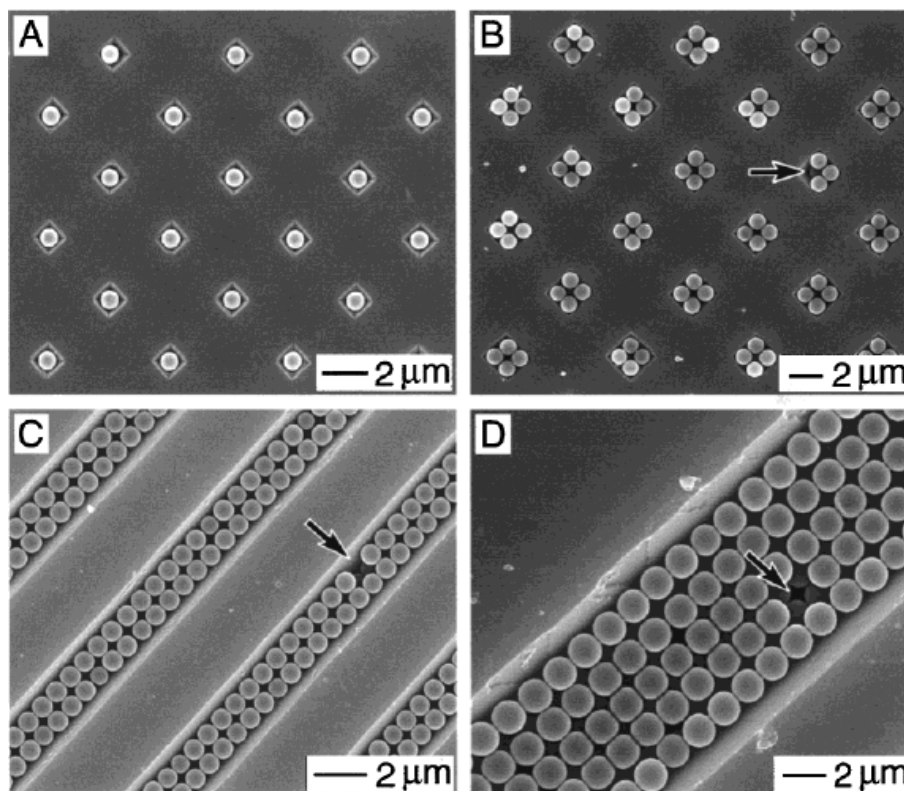


Figure 2-20: SEM images of colloidal alignment with different geometries produced by Yin et al. The arrows indicate missing particles.⁵³

The deposition of a liquid or polymeric solution onto the surface of a substrate by Inkjet Printing (IJP) has also been used to deposit patterned liquids or suspensions on ceramic surfaces. Figure 2-21 shows a few methods of inkjet printing where a small amount of liquid can be deposited on the surface. This process has a high degree of spatial control, but the smallest achievable written size using current technology ranges from 20 – 50 μm .⁵⁴ The droplet resolution is limited by the in-flight direction of droplets (the nozzle does not touch the surface for patterning) and by the wetting behavior with respect to the substrate.

Although this process is ideal for depositing liquids or dopants on the surface, using the ink-jet process with solid plate-like templates, and controlling the orientation of a single plate-like template at each location, seems to be difficult.

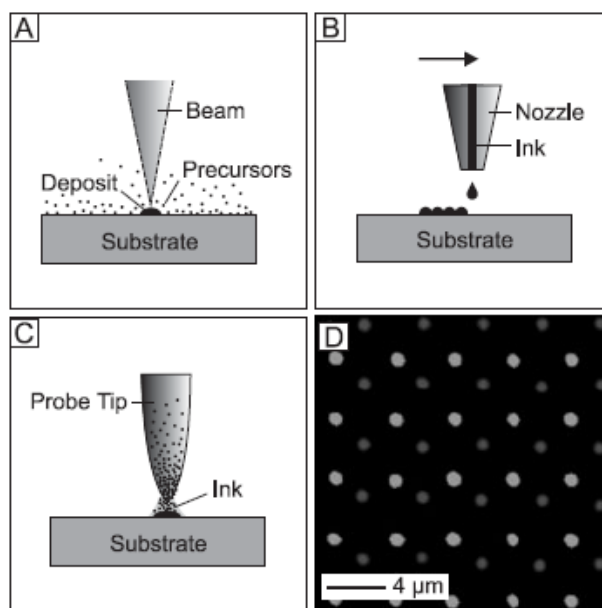


Figure 2-21: Schematics of different writing schemes, A) Precursor solution are decomposed near the focal point of a beam to deposit material on the surface. B) Ink Jet Printing, where liquids are ejected from a nozzle and deposited on the surface of the substrate. C) Direct writing of particles or a liquid onto a substrate. D) Fluorescence microscopy of an array of hybridized DNA sequences produced by dip-pen nanolithography.⁵⁴

Soft lithography has been shown to have better resolution control (nanometer scale resolution) and higher control over the template designs than the methods described above. Figure 2-22 shows a typical pattern produced by the soft lithography technique using a poly(dimethyl siloxane) (PDMS) mold to deposit liquid precursors of polymeric and ceramic materials.⁵⁴ The process involves creating a master mold (negative of the required PDMS stamp) by optical lithography with the use of non-reactive photoresists (such as the SU8 series produced by MicroChem, Newton, MA). Once the master mold is completed, PDMS is coated over the master mold and cured at room temperature, under vacuum to prevent any air entrapment for 24 h. The PDMS is then carefully removed and used for depositing the polymeric or ceramic materials. This is done by spin-coating the solution on the PDMS stamp, and with pressure “stamping” the substrate and transferring the spin-coated solution.

This process can produce various patterns with ranges of complexity, as indicated in Figure 2-22, with feature sizes ranging from 300 nm to several millimeters. With repeated stamping, heights can be achieved up to 1 μm .⁵⁴ Nagata et al. fabricated BaTiO_3 thin film capacitors by microcontact printing with a PDMS stamp. This method successfully produced capacitors with a dielectric layer of 0.2 μm , with a relative permittivity >800 .⁵⁵ The major drawbacks to microcontact printing via PDMS molds are: a) finding materials to deposit that are compatible with the PDMS stamp, and b) maintaining image retention on the substrate after the mold has been removed, and c) producing samples with a height above 1 μm .⁵⁴ This process is ideal for depositing precursor solutions in a patterned array, but would be difficult to deposit a single template for textured growth.

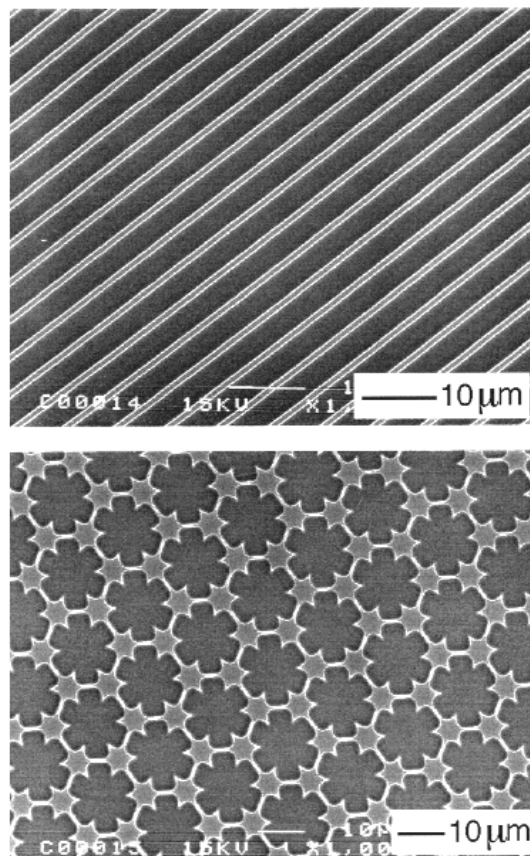


Figure 2-22: SEM images of different patterns produced by soft-lithography.⁵⁴

Optical lithography uses photosensitive polymeric materials (resins) deposited on a substrate. The resins are spin coated on the surface of the substrate and the thicknesses range from 0.5 μm (AZ 1800 series resist by Rohm & Haas Electronic Materials) to 50 μm (SU-8 series resists by MicroChem).⁵⁴ When exposed to UV light through a patterned chrome mask, the relative solubility of the resist in a developer can be changed, enabling transfer of that pattern into the resist. This can subsequently be transferred to the substrate by etching processes.⁵⁴ Optical lithography has a resolution limit near 0.6 microns, and has excellent pattern retention.⁵⁶

Jiang, et al.⁵⁷ utilized a combination of photolithography and dry etching to produce pillared single crystal $\text{Pb}(\text{Mg}_{1/3}\text{Nb}_{2/3})\text{O}_3\text{-PbTiO}_3$ (PMN-PT). The process involved transferring the pattern through a chrome mask onto the PMN-PT surface that

has the resist spun on it. A nickel mask was electrodeposited on the surface of the polished PMN-PT single crystal in the pattern of the required size and distribution of the ceramic pillars (transferred from the chrome mask). A nickel hard mask was required to withstand the dry etching process, since the photoresist is removed during the etching process.⁵⁴ Using reactive ion etching on the exposed single crystal areas produced a pillar height of 60 μm . The spacing at the top of the pillars was roughly 2 microns, and the final single crystal pillar geometry had a 4:1 aspect ratio.⁵⁷ This method can produce high aspect ratio templates, with good lateral resolution. Thus optical lithography with reactive ion etching has been chosen as the primary method of producing the templates from the initial [001] and [110] BaTiO₃ single crystals.

2.5 References

1. Jona, F. and G. Shirane, Barium Titanate, in *Ferroelectric Crystals*. 1962, Pergamon Press: New York, NY. p. 108-215.
2. Frazer, B.C., H.R. Danner, and R. Pepinsky, "Single-Crystal Neutron Analysis of Tetragonal BaTiO₃," *Phys. Rev.*, **100**[2]: 745-6 (1955).
3. Jaffe, B., W.R. Cook, and H. Jaffe, Piezoelectric Ceramics. 1971, Marietta, OH: R.A.N. Publishers.
4. Wemple, S.H., J. M. Didomenico, and I. Camlibel, "Dielectric and Optical Properties of Melt-Grown BaTiO₃," *J. Phys. Chem. Solids*, **29**[10]: 1797-1803 (1968).
5. Kingery, W.D., H.K. Bowen, and D.R. Uhlmann, Introduction to Ceramics. 2nd Edition ed. 1976, New York: John Wiley & Sons. 368.
6. Megaw, H.D., Ferroelectricity in Crystals. 1957: Methuen & Co. Ltd.
7. Moulson, A.J. and J.M. Herbert, Electroceramics. 2003, West Sussex, England: John Wiley & Sons Ltd.
8. Li, Y.L., L.E. Cross, and L.Q. Chen, "A Phenomenological Thermodynamic Potential for BaTiO₃ Single Crystals," *J. Appl. Phys.*, **98**[6]: 064101, 1-4 (2005).
9. Rehrig, P.W., S.-E. Park, S. Trolrier-McKinstry, G.L. Messing, B. Jones, and T.R. ShROUT, "Piezoelectric Properties of Zirconium-Doped Barium Titanate Single Crystals grown by Templated Grain Growth," *J. Appl. Phys.*, **86**[3]: 1657-61 (1999).

10. Lyddane, R.H., R.G. Sachs, and E. Teller, "On the Polar Vibrations of Alkali Halides," *Phys. Rev.*, **59**: 673-6 (1941).
11. A.S. Barker, J., "Long-Wavelength Soft Modes, Central Peaks, and the Lyddane-Sachs-Teller Relation," *Phys. Rev. B*, **12**[10]: 4071-84 (1975).
12. Newnham, R.E., Properties of Materials: Anisotropy, Symmetry, Structure. 2005: Oxford University Press.
13. Du, X.-H., Q.-M. Wang, U. Belegundu, A. Bhalla, and K. Uchino, "Crystal Orientation Dependence of Piezoelectric Properties of Single Crystal Barium Titanate," *Mater. Let.*, **40**: 109-13 (1999).
14. Wada, S., H. Kakemoto, and T. Tsurumi. *Domain Wall Engineering in Lead-free Piezoelectric Materials*. in *International Conference on Electroceramics*. 2007. Arusha, Tanzania.
15. Wada, S., K. Yako, H. Kakemoto, T. Tsurumi, and T. Kiguchi, "Enhanced Piezoelectric Properties of Barium Titanate Single Crystals with Different Engineered-Domain Sizes," *J. Appl. Phys.*, **98**: 014109, 1-7 (2005).
16. Kirby, K.W. and B.A. Wechsler, "Phase Relations in the Barium Titanate - Titanium Oxide System," *J. Am. Ceram. Soc.*, **74**[8]: 1841-7 (1991).
17. Lee, S. and C.A. Randall, "Modified Phase Diagram for the Barium Oxide-Titanium Dioxide System for the Ferroelectric Barium Titanate," *J. Am. Ceram. Soc.*, **90**[8]: 2589-94 (2007).
18. Filimonov, D.S., Z.-K. Liu, and C.A. Randall, "Phase Relations in the BaO - TiO_{2-δ} System Under Highly Reducing Conditions," *Mater. Res. Bull.*, **38**: 545-53 (2003).
19. Lee, S., C.A. Randall, and Z.-K. Liu, "Comprehensive Linkage of Defect and Phase Equilibria Through Ferroelectric Transition Behavior in BaTiO₃-Based Dielectrics: Part 2. Defect Modelin Under Low Oxygen Partial Pressure Conditions," *J. Am. Ceram. Soc.*, **91**[6]: 1753-1761 (2008).
20. Rameika, J.P., "A Method for Growing Barium Titanate Single Crystals," *J. Am. Ceram. Soc.*, **76**[2]: 940-1 (1954).
21. Brown, F. and W.H. Todt, "Floating-Zone BaTiO₃: Preparation and Properties," *J. Appl. Phys.*, **35**[5]: 1594-8 (1964).
22. Belruss, V., J. Kalnajs, A. Linz, and R.C. Folweiler, "Top-Seeded Solution Growth of Oxide Crystals from Non-Stoichiometric Melts," *Mater. Res. Bull.*, **6**[10]: 899-906 (1971).

23. Yoo, Y.S., M.K. Kang, J.H. Han, H. Kim, and D.Y. Kim, "Fabrication of BaTiO₃ Single Crystals by Using Exaggerated Grain Growth Method," *J. Euro. Ceram. Soc.*, **17**[14]: 1725-7 (1997).
24. Saldana, J.M., B. Mullier, and G.A. Schneider, "Preparation of BaTiO₃ Single Crystals Using the Modified SiO₂-Exaggerated Grain Growth Method," *J. Euro. Ceram. Soc.*, **22**[5]: 681-8 (2002).
25. Lee, H.-Y., J.-S. Kim, and D.-Y. Kim, "Fabrication of BaTiO₃ Single Crystals Using Secondary Abnormal Grain Growth," *J. Euro. Ceram. Soc.*, **20**: 1595-7 (2000).
26. Yamamoto, T. and T. Sakuma, "Fabrication of Barium Titanate Single Crystals by Solid-State Grain Growth," *J. Am. Ceram. Soc.*, **77**[4]: 1107-1109 (1994).
27. Rehrig, P.W., G.L. Messing, and S. Trolier-McKinstry, "Templated Grain Growth of Barium Titanate Single Crystals," *J. Am. Ceram. Soc.*, **83**[11]: 2654-60 (2000).
28. Rehrig, P.W., *Templated Grain Growth of BaTiO₃-Based Perovskite Single Crystals*, PhD. in *Materials Science and Engineering*. 1999, the Pennsylvania State University. p. 129.
29. Messing, G.L., S. Trolier-McKinstry, E.M. Sabolsky, C. Duran, S. Kwon, B. Brahmaroutu, P. Park, H. Yilmaz, P.W. Rehrig, K.B. Eitel, E. Suvaci, M. Seabaugh, and K.S. Oh, "Templated Grain Growth of Textured Piezoelectric Ceramics," *Critical Reviews in Solid State and Materials Sciences*, **29**: 45-96 (2004).
30. Ohara, Y., K. Koumoto, and H. Yanagida, "Barium Titanate Ceramics with High Piezoelectricity Fabricated from Fibrous Particles," *J. Am. Ceram. Soc.*, **68**[4]: C108-C109 (1985).
31. Kimura, T., Y. Miura, and K. Fuse, "Texture Development in Barium Titanate and PMN-PT Using Hexabarium 17 Titanate Heterotemplates," *Int. J. Appl. Ceram. Technol.*, **2**[1]: 15-23 (2005).
32. Wada, S., K. Takeda, T. Muraishi, H. Kakemoto, T. Tsurumi, and T. Kimura, "Preparation of [110] Grain Oriented Barium Titanate Ceramics by Templated Grain Growth Method and Their Piezoelectric Properties," *Jap. J. Appl. Phys.*, **46**[10B]: 7039-43 (2007).
33. Sato, T. and T. Kimura, "Preparation of <111> Textured BaTiO₃ Ceramics by Templated Grain Growth Method Using Novel Template Particles," *Ceram. International*, **34**: 757-760 (2008).
34. Sugawara, T., Y. Nomura, T. Kimura, and T. Tani, "Fabrication of <111> Oriented BaTiO₃ Bulk Ceramic by Reactive Templated Grain Growth," *J. Ceram. Soc. Jap.*, **109**[10]: 897-900 (2001).

35. Sato, T., Y. Yoshida, and T. Kimura, "Preparation of <110> Textured BaTiO₃ Ceramics by the Reactive-Templated Grain Growth Method Using Needlelike TiO₂ Particles," *J. Am. Ceram. Soc.*, **90**[9]: 3005-8 (2007).
36. Yamamoto, T., "Influence of Small Ba/Ti Non-Stoichiometry on Grain Growth Behavior in Barium Titanate," *Brit. Ceram. Trans.*, **94**[5]: 196-200 (1995).
37. Hu, Y.H., M.P. Harmer, and D.M. Smyth, "Solubility of BaO in BaTiO₃," *J. Am. Ceram. Soc.*, **68**[7]: 372-6 (1985).
38. Rios, P.R., T. Yamamoto, T. Kondo, and T. Sakuma, "Abnormal Grain Growth Kinetics of BaTiO₃ with an Excess of TiO₂," *Acta. Mater.*, **46**[5]: 1617-23 (1998).
39. Dawson, W.J., J.C. Preston, and S.L. Swartz, Processing Issues of Hydrothermal Synthesis of Dielectric Powders, in *Ceramic Powder Science IV*. 1991, American Ceramic Society: Westerville, OH. p. 27-32.
40. Lee, B.-K., S.-Y. Chung, and S.-J. Kang, "Grain Boundary Faceting and Abnormal Grain Growth in BaTiO₃," *Acta. Mater.*, **48**: 1575-80 (2000).
41. Lee, B.-K. and S.-J. Kang, "Second-Phase Assisted Formation of {111} Twins in Barium Titanate," *Acta. Mater.*, **49**: 1373-81 (2001).
42. Matsuo, Y. and H. Sasaki, "Exaggerated Grain Growth in Liquid-Phase Sintering of BaTiO₃," *J. Am. Ceram. Soc.*, **54**[9]: 417 (1971).
43. Kumar, U., S.F. Wang, U. Selvaraj, and J.P. Dougherty, "Densification and Dielectric Properties of Hydrothermal BaTiO₃ with Different Sources of Bi₂O₃," *Ferroelectrics*, **154**: 283-8 (1994).
44. Jung, Y.-I., S.-Y. Choi, and S.-J. Kang, "Grain-Growth Behavior During Stepwise Sintering of Barium Titanate in Hydrogen Gas and Air," *J. Am. Ceram. Soc.*, **86**[12]: 2228-30 (2003).
45. Jung, Y.-I., S.-Y. Choi, and S.-J.L. Kang, "Effect of Oxygen Partial Pressure on Grain Boundary Structure and Grain Growth Behavior in BaTiO₃," *Acta. Mater.*, **54**[10]: 2849-55 (2006).
46. Choi, S.-Y. and S.-J. Kang, "Sintering Kinetics by Structural Transition at Grain Boundaries in Barium Titanate," *Acta. Mater.*, **52**: 2937-43 (2004).
47. Polotai, A., K. Breece, E. Dickey, C. Randall, and A. Ragulya, "A Novel Approach to Sintering Nanocrystalline Barium Titanate Ceramics," *J. Am. Ceram. Soc.*, **88**[11]: 3008-12 (2005).
48. Rahaman, M.N. and R. Manalart, "Grain Boundary Mobility of BaTiO₃ Doped with Aliovalent Cations," *J. Euro. Ceram. Soc.*, **18**: 1063-71 (1998).

49. Cahn, J.W., "The Impurity-Drag Effect in Grain Boundary Motion," *Acta. Mater.*, **10**[9]: 789-98 (1962).
50. Chiang, Y.-M. and T. Takagi, "Grain Boundary Chemistry of Barium Titanate and Strontium Titanate," *J. Am. Ceram. Soc.*, **73**[11]: 3278-85 (1990).
51. Brzozowski, E. and M.S. Castro, "Grain Growth Control in Nb-Doped BaTiO₃," *J. Mater. Proc. Tech.*, **168**: 464-70 (2005).
52. Chan, H.M., M.P. Harmer, and D.M. Smyth, "Compensating Defects in Highly Donor-Doped BaTiO₃," *J. Am. Ceram. Soc.*, **69**[6]: 507-10 (1986).
53. Yin, Y., Y. Lu, B. Gates, and Y. Xia, "Template-Assisted Self-Assembly: A Practical Route to Complex Aggregates of Monodispersed Colloids with Well-Defined Sizes, Shapes, and Structures," *J. Am. Chem. Soc.*, **123**: 8718-29 (2001).
54. Geissler, M. and Y. Xia, "Patterning: Principles and Some New Developments," *Adv. Mater.*, **16**[15]: 1249-69 (2004).
55. Nagata, H., S.W. Ko, E. Hong, C.A. Randall, S. Trolier-McKinstry, P. Pinceloup, D. Skamser, M. Randall, and A. Tajuddin, "Microcontact Printing BaTiO₃ and LaNiO₃ Thin Films for Capacitors," *J. Am. Ceram. Soc.*, **89**[9]: 2816-21 (2006).
56. Eichfeld, C., *Personal communication*. December 2008: State College, PA.
57. Jiang, X., J.R. Yuan, A. Cheng, K. Snook, P.J. Cao, P.W. Rehrig, W.S. Hackenberger, G. Lavallee, X. Geng, and T.R. Shrout, "Microfabrication of Piezoelectric Composite Ultrasound Transducers (PC-MUT)," *IEEE Ultrasonics Symposium Proceedings*, **2**: 918-21 (2006).

Chapter 3

Enhanced BaTiO₃ Grain Growth by Surface Doping

3.1 Introduction

Control over microstructure evolution in BaTiO₃ is important, since the piezoelectric and dielectric properties of BaTiO₃ are strongly dependent on microstructural characteristics. The grain size and morphology, amount of porosity, and the orientation and distribution of aligned grains in the microstructure all affect the properties of BaTiO₃.^{1,2}

Arlt et al. studied the effect of grain size on the dielectric constant in BaTiO₃ ceramics for samples with grain sizes ranging from 0.3 μm – 100 μm. They showed that decreasing the grain size to 1 μm resulted in an increase in the room temperature dielectric constant to 5000 from values of 1500 – 2000 for coarse-grained BaTiO₃. The increase in the dielectric constant was attributed to a decrease in the width of the 90° domains resulting from higher internal stresses in the grains.³

Frey and Payne studied the changes in dielectric constant and phase transitions in fine grained BaTiO₃. They reported that at a grain size of ~ 0.4 μm the macro-symmetry becomes a mixture of orthorhombic, rhombohedral, and cubic.⁴ The local symmetry was still be non-centrosymmetric below this grain size. They determined that there was no loss of ferroelectricity in fine-grained BaTiO₃ for grain sizes above 40 nm.⁵

Demartin and Damjanovic studied the effect of dynamic and static pressure on the piezoelectric coefficient in both coarse and fine-grained BaTiO₃. The longitudinal piezoelectric coefficient, d_0 (relative to the initial value), was higher for coarse-grained samples compared to fine-grained materials (110 pC/N vs. 50 pC/N, respectively). The reduction in piezoelectric response with pressure was attributed to a) greater restriction of domain wall movement and b) the presence of internal stresses in the fine-grained samples.⁶

The orientation and distribution of textured grains within the microstructure can lead to improvements in the piezoelectric response compared to randomly oriented ceramics. Wada et al. prepared [110] textured BaTiO₃ samples by tape casting a mixture of nano-sized BaTiO₃ powder with [110] BaTiO₃ plate-like templates. The relative densities of the samples were 96%, with texture fractions ranging from 0 – 98%, as measured by the XRD Lotgering method. They reported that d_{31} remained constant at -50 pC/N for all texture levels, but the d_{33} reached a value of 788 pC/N at 85% texture (4 times the random ceramic value).⁷ It is not at all clear why the ratio of d_{33}/d_{31} should change in this way, as no similar anisotropy is developed in other textured ceramics or, indeed, in single crystals with engineered domain structures.

Du et al. determined the effect of crystal orientation on the piezoelectric properties of BaTiO₃ single crystals.⁸ They poled tetragonal BaTiO₃ single crystals along the [001] direction, then cut the crystal at various angles in reference to the poled direction. The measured d_{33} , k_{33} , ϵ_{33} , and s_{33} constants as a function of crystal orientation along the angles: 0°, 45°, 50°, and 60° are summarized in Table 3-1. They showed that there is a peak in the responses at 50° from the [001] poled direction, which corresponds approximately to the [111] pseudocubic direction.

Damjanovic et al. also calculated the orientation dependence of the longitudinal and transverse piezoelectric properties of BaTiO₃.^{9,10} The authors indicated that an increase in the piezoelectric constants can develop at an angle to the spontaneous polarization direction, when there is a near-by phase transition that leads to a large transverse dielectric constant. For the tetragonal phase, the maximum d_{33} occurred 51.6° away from the polar axis.⁹ This is in good agreement with Du et al.'s experimental work.⁸ Damjanovic et al. calculated the maximum piezoelectric coefficients in the other BaTiO₃ crystal symmetries and determined a peak in the d_{33} at 53° and 60.3° for the orthorhombic and the rhombohedral symmetries, respectively.⁹ These values are in good agreement with the engineered domain states described by Wada et al.⁷

Table 3-1: Constants d_{33} , k_{33} , ϵ_{33} , and s_{33} in different BaTiO₃ single crystal cut directions.⁸

Constants	0°	45°	50°	60°
d_{33} (pC/N)	24.69	85.72	129.44	95.4
k_{33}	0.2	0.264	0.33	0.246
ϵ_{33}	103	1795	2873	2263
s_{33} ($\times 10^{-3}$ / GPa)	17.56	6.63	5.94	7.47

Thus, it is clear from the literature that controlled orientation is very useful in optimizing the piezoelectric response of perovskite ferroelectrics such as BaTiO₃. As described in Chapter 1, new methods of preparing ceramics and single crystals with improved orientations are needed. Thus, the objective of this chapter is to understand the kinetics of localized grain growth for use in subsequent templated grain growth studies. From the work outlined in Section 2.2.2, additives such as TiO₂ and SiO₂ can be used to form a liquid phase and cause enhanced grain growth in BaTiO₃. In this study, both TiO₂ and SiO₂ surface doping were studied as a means to initiate the grain growth enhancement. Photolithographic processes were used to control the location of the doped region. Use of a patterned dopant enables fundamental studies on the effect of dopant diffusion on the vertical and lateral growth of BaTiO₃. Also, to gain an understanding of the matrix evolution in the patterned microstructure, the kinetics of the grain growth was studied as a function of the TiO₂ or SiO₂ concentration, temperature and atmospheric conditions.

3.2 Experimental Procedure

Polycrystalline BaTiO₃ samples were prepared by a non-aqueous tape casting approach. BaTiO₃ powder (MBT-02 from Sakai Chemical Industry, (Sakai, Osaka, Japan) with a Ba/Ti = 0.996, 200 nm particle size) was ball milled for 24 h with 3.5 wt% menhaden fish oil in ethanol and xylenes (50/50 wt. ratio). 1.3 wt% each of polyalkylene

glycol (Tape Casting Warehouse (Yardley, PA), Molecular Weight (MW) = 2,000) and butyl benzyl phthalate (S-160, Tape Casting Warehouse, MW = 312), and 2.8 wt% poly(vinyl) butyral (B98, Tape Casting Warehouse, MW = 40,000-70,000) were added to the mixture and it was ball milled for an additional 24 h. The slurry was de-aired under vacuum for 15 min and cast with 200 μm blade height (100 μm dried tape thickness) and cut into 30 mm x 30 mm sections. The 30 mm x 30 mm sections were then stacked to a green thickness of 1.25 mm and isostatically laminated (Pacific Trinetics Corporation, PTC IL-4004-D, Carlsbad, CA) at 75°C at 20 MPa for 1 h.

The organics were removed by heating the sample at 650°C for 2 h in air. The samples were then isostatically pressed at 200 MPa and sintered at 1300°C for 1.25 h with a PO_2 of 1×10^{-13} atm using a combination of 120 sccm wet N_2 , 368 sccm dry N_2 and 12 sccm H_2 gases. The wet N_2 gas was bubbled through deionized water to achieve the required oxygen level. The densities of the sintered samples were measured by Archimedes method and the average grain size was measured by the linear intercept method.¹¹

The surfaces of the BaTiO_3 sintered samples were polished with progressively finer grit sizes with a final polish with 0.25 μm diamond suspension ((Glycol based, Allied High Tech Products, Inc., Rancho Dominguez, California) with Green Lube (Allied High Tech Products, Inc.) as a lubricating medium on a MetPrep 4 series manual polisher (Allied High Tech Products, Inc.)).

To surface pattern the sintered samples with TiO_2 , they were spin coated (PWM32, Headway Research, Garland, TX) with a 0.25 M TiO_2 sol-gel layer. The solution was prepared by mixing titanium (IV) isopropoxide (Sigma Aldrich, St. Louis, MO) with 2-methoxyethanol (2-MOE) (Sigma Aldrich) under vacuum at room temperature for 2 h. Two ml acetyl acetone (Sigma Aldrich) was added to 2.8 g titanium (IV) isopropoxide for stabilization. The TiO_2 sol was spin coated at 4000 rpm for 30 s to produce a 25 nm thick layer on the polished polycrystalline BaTiO_3 surface. Additional layers were added to achieve thicknesses ranging from 50 nm to 150 nm. The samples were heated to 150°C for 120 s, then 350°C for 360 s on a hot plate to pyrolyze the film.

The sol-gel layer was patterned by photolithography using a mask consisting of 1000 μm lines with a pitch of 1000 μm to produce the TiO_2 dopant pattern shown in Figure 3-1. A photoresist (AZ-1827, Rohm & Haas Electronic Materials, LLC, Philadelphia, Pa) was spin coated onto the densified BaTiO_3 at 4000 rpm for 40 s. The sample was then soft baked at 100°C for 30 s on a hotplate. The sample was then exposed by UV light (Karl Suss MA6 Contact Aligner, Karl Suss America, Inc., Waterbury Center, VT) for 6 s, and developed (MF-CD-26, Rohm & Haas Electronic Materials, LLC) for 40 s and washed with deionized water. Afterwards, the sample was hard baked at 100°C for 120 s, and a 6:1 buffered oxide etch (10% HF, Transene Company, Inc., Rowley, MA) was used for 30 s – 120 s to remove the exposed TiO_2 . A visual stop process was used to determine when the TiO_2 etching process was completed. During the etching the TiO_2 would change colors due to optical interference effects. When the color became a dark blue (the color of the polished BaTiO_3 surface) the sample was then removed from the HF solution and cleaned with deionized water. The sample was then dried with N_2 and the remaining photoresist was then washed off using acetone. Profilometry (Tencor P10, KLA Tencor, Milpitas, California) was conducted across the BaTiO_3 / TiO_2 boundary and the average etch depth of the BaTiO_3 ceramic was 100 nm.

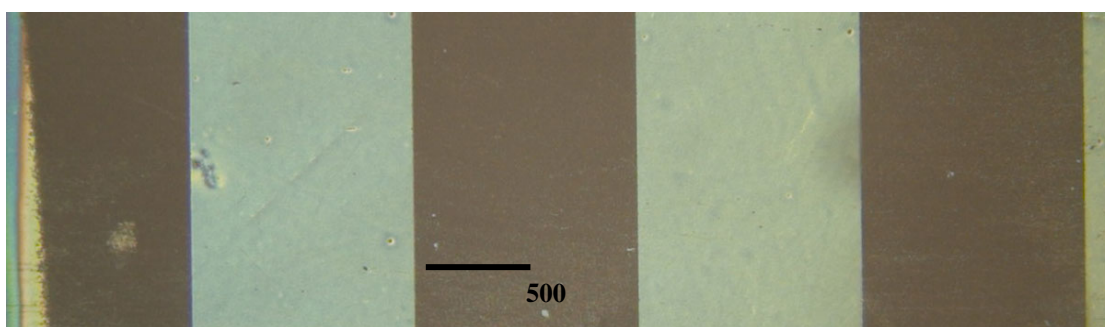


Figure 3-1: Optical Image of the 1000 μm TiO_2 line pattern (light region) on a polished polycrystalline BaTiO_3 sample (dark region).

SiO_2 patterned BaTiO_3 samples were prepared by mixing tetraethoxysilane (Alfa Aesar, Ward Hill, MA) in 2-MOE to a 0.25M concentration. The deposition and

patterning of SiO₂ was accomplished by the same procedures described for the TiO₂ solution.

The patterned samples were heated between 1250°C and 1400°C in air and 1×10^{-5} atm PO₂, and were characterized by optical (BX60M, Olympus America Inc., Center Valley, PA with AxioCam by Carl Zeiss Inc., Thornwood, NY) and scanning electron microscopy (S-3500N and S-3000H, Hitachi Ltd., Tokyo, Japan).

For electron backscattered diffraction analysis (EBSD, Hitachi S3500N with TSL/EDAX OIM, Mahwah, NJ) the samples were polished with progressively finer grit sizes with final polishes with 0.05 μm diamond then alumina suspensions. The sample was mounted on a 20° conductive sample holder with carbon tape. The sample was then oriented at 70° to the detector and the orientation analysis was conducted.

3.3 Results and Discussion

3.3.1 BaTiO₃ Matrix Fabrication

Initial work was undertaken to track the evolution of the BaTiO₃ matrix grain size. This was done since the thermodynamic driving force for the growth of the large grains is inversely proportional to the average matrix grain size. Thus, in order to maximize the growth of particular grains at the sample surface, it is important to produce a dense polycrystalline matrix with the smallest grain size possible.

Initial sintering of BaTiO₃ ceramics was conducted either in an air or in a reducing atmosphere at a PO₂ ~ 10⁻¹¹ atm. It has been shown that by sintering at low PO₂ (1 × 10⁻¹¹ to 1 × 10⁻¹⁷ atm), grain boundary motion is retarded and exaggerated grain growth is avoided.¹²⁻¹⁴ Samples were heated to 1300°C at 5°C/min with a dwell time of 1.5 h and cooled at the same rate.

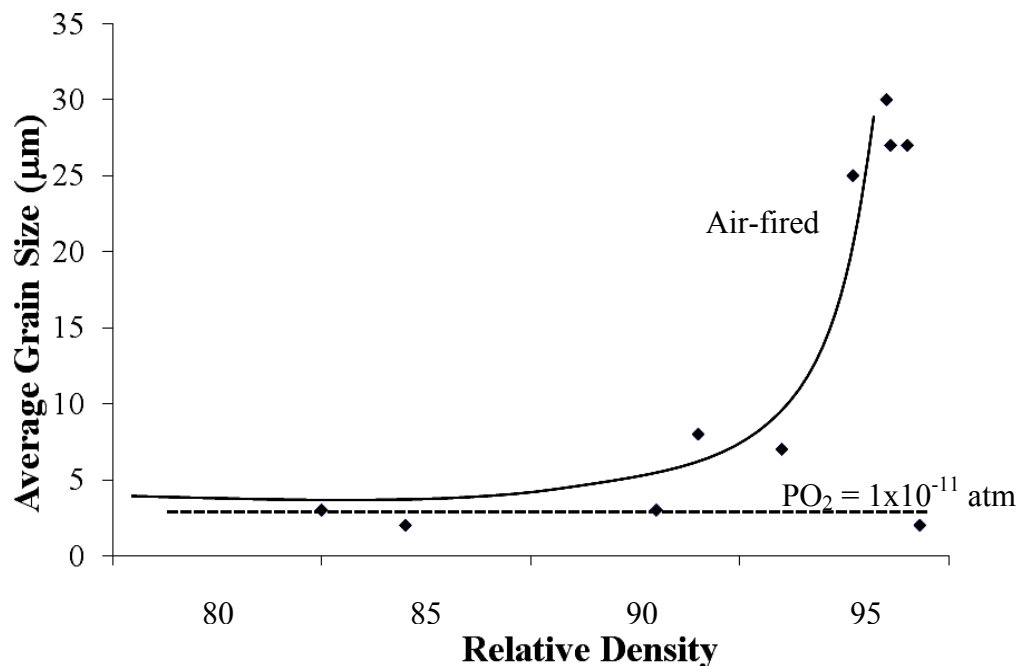


Figure 3-2: Average grain size as a function of relative density for air sintering (solid line) and reducing sintering at $\text{PO}_2 = 1 \times 10^{-11}$ atm of BaTiO_3 ceramics (dotted line).

The solid line in Figure 3-2 shows the typical behavior of Ti-rich BaTiO_3 sintered in air,^{15,16} while the dashed line indicates the samples fired in the reducing environment. As the density approaches 100%, the grain size dramatically increases for the samples fired in air and large exaggerated grains ($\sim 100 \mu\text{m}$) are observed. The air-fired samples have too large a grain size in the matrix for any subsequent surface patterning runs because the thermodynamic driving force for patterned growth was reduced too much. In contrast, a dense ($>99\%$ theoretical density) compact with an average grain size of $3 \mu\text{m}$ (Figure 3-3) was obtained with the reducing sintering atmosphere (red line in Figure 3-2). Ceramics fired under these conditions were used for subsequent studies on localized grain growth induced by patterned surface modification.

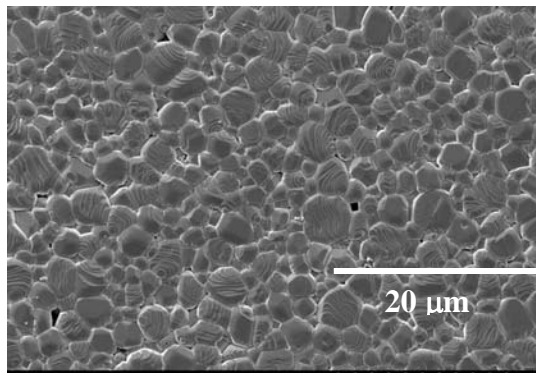


Figure 3-3: SEM image showing a polished and thermally etched (1200°C, 10 min, in air) surface of the BaTiO₃ sample fired in PO₂ = 1×10⁻¹¹ atm at 1300°C for 1.25 h.

3.3.1 Grain Growth in TiO₂ and SiO₂ Surface Patterned BaTiO₃

Figure 3-4 shows the extent of grain growth when a 300 nm thick layer of either TiO₂ or SiO₂ was spin coated over the entire surface of the BaTiO₃ compact. The samples were then fired for 10 min in air at 1300°C. Both samples showed a significant amount of enhanced grain growth from the surface (i.e. the diffusion affected zone). The boundary between the diffusion affected zone and the unaffected matrix grains was ~360 μm and over 1000 μm (measured from the BaTiO₃ surface) for the TiO₂ and SiO₂ dopants, respectively (Figure 3-4). The grain size of TiO₂ doped BaTiO₃ was 100 – 150 μm in the diffusion affected zone, while the grains of the SiO₂ doped BaTiO₃ in the diffusion affected zone were as large as 300 μm. The matrix grain size far from the surface was ~25 μm for both conditions. In both cases, diffusion affected zone was several grains thick. From previous reports,¹⁷ the greater extent of exaggerated grain growth achieved using the SiO₂ dopant can be attributed to the formation a liquid phase. The XRD pattern in Figure 3-5 revealed the presence of a Ba₂TiSi₂O₈ second phase in the SiO₂ doped BaTiO₃ samples. However, no second phases were detected in the TiO₂

doped BaTiO_3 . The presence of a second phase is known to inhibit single crystal conversion.¹⁸ Thus, TiO_2 doping of BaTiO_3 was selected for further study.

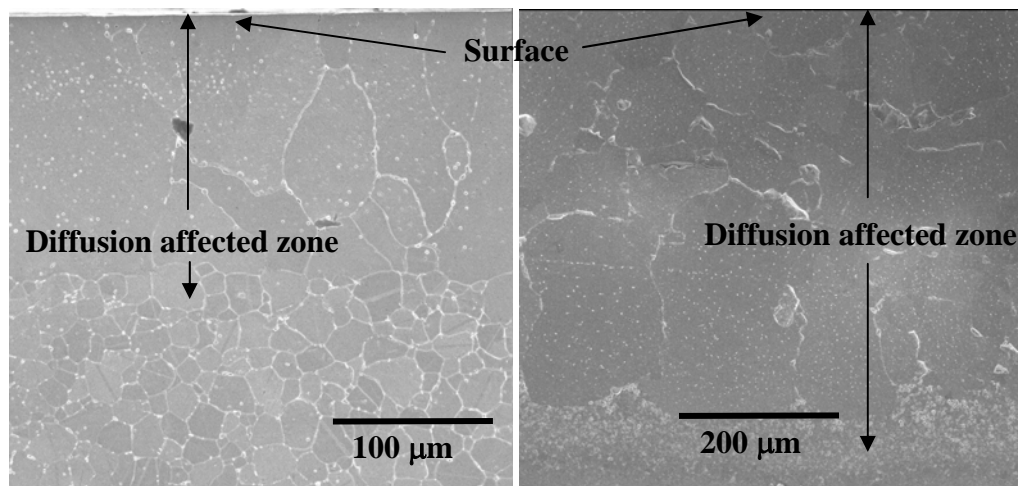


Figure 3-4: SEM micrographs showing the diffusion affected zone was observed using 300 nm of a) TiO_2 and b) SiO_2 fired in air at 1300°C for 10 min.

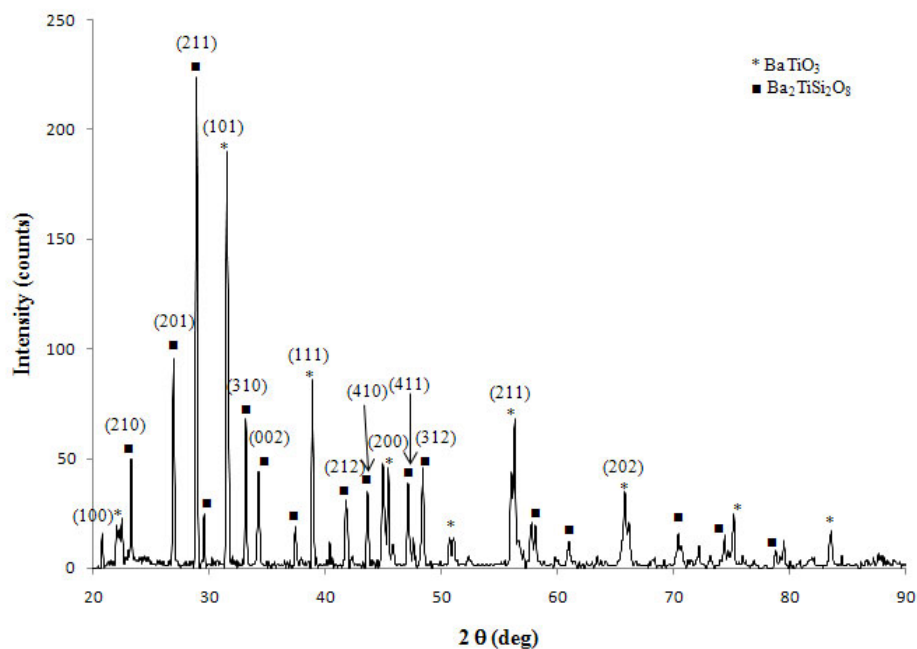


Figure 3-5: XRD analysis of the surface of the 300 nm SiO_2 doped BaTiO_3 sample fired in air at 1300°C for 10 min. (JCPDS Card #'s 00-005-0626 for BaTiO_3 and 00-022-0513 for $\text{Ba}_2\text{TiSi}_2\text{O}_8$).

BaTiO₃ samples were prepared with 50 nm, 100 nm, and 150 nm thick TiO₂ film coatings which were patterned into a 1000 μm line array with 1000 μm spacing between each line. The patterned samples were fired in air from 1250 – 1350°C for 0.5 h to 2 h. There was no grain growth enhancement in samples fired below 1300°C. Likewise, no grain growth enhancement was evident in samples doped with 50 nm and 100 nm TiO₂ that were fired at 1300°C. The absence of enhanced grain growth below 1300°C is attributed to too low a firing temperature for liquid phase formation. The microstructure (Figure 3-6) of the 150 nm TiO₂ layer when fired to 1300°C for 1 h shows enhanced growth on the order of 100's of microns for each condition. This indicates that there is a critical TiO₂ amount required to induce enhanced grain growth on the surface of BaTiO₃.

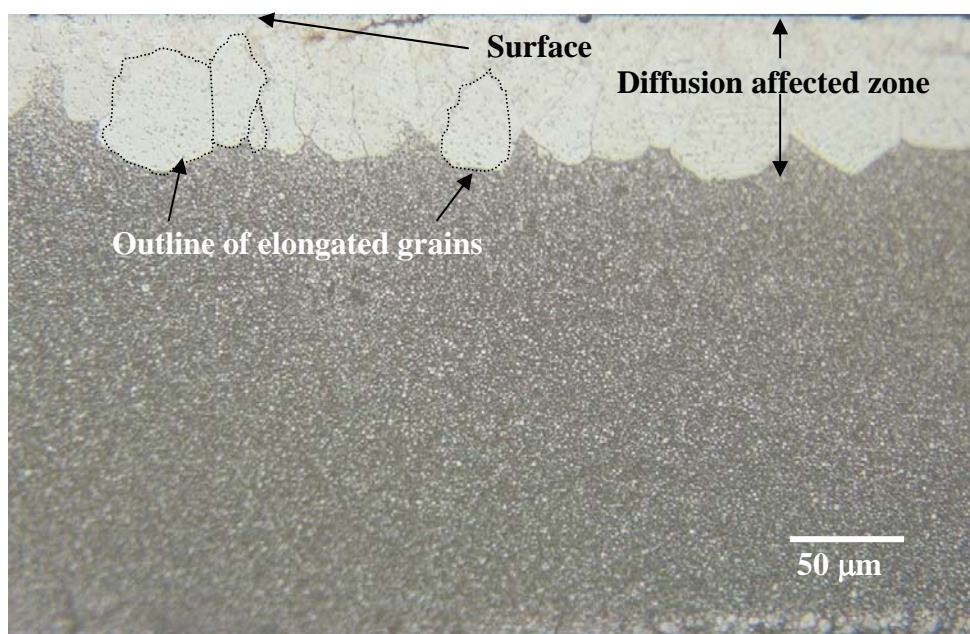


Figure 3-6: An optical image of the enhanced growth region (light gray) in contrast to the remaining matrix grains (dark gray) for a 150 nm TiO₂ doped BaTiO₃ sample fired in air at 1300°C for 1 h.

Figure 3-7 shows the vertical and lateral growth distances plotted as a function of heat treatment time for the 150 nm TiO₂ doped BaTiO₃ sample at 1300°C. With increasing time, the vertical growth distance increases linearly and approaches 300 μm after 2 h in air. The lateral growth distance approaches 200 μm after 2 h in air. The difference in growth results in an elongated grain shape (Figure 3-6). Also shown in Figure 3-7 is the matrix coarsening as a function of time for these samples.

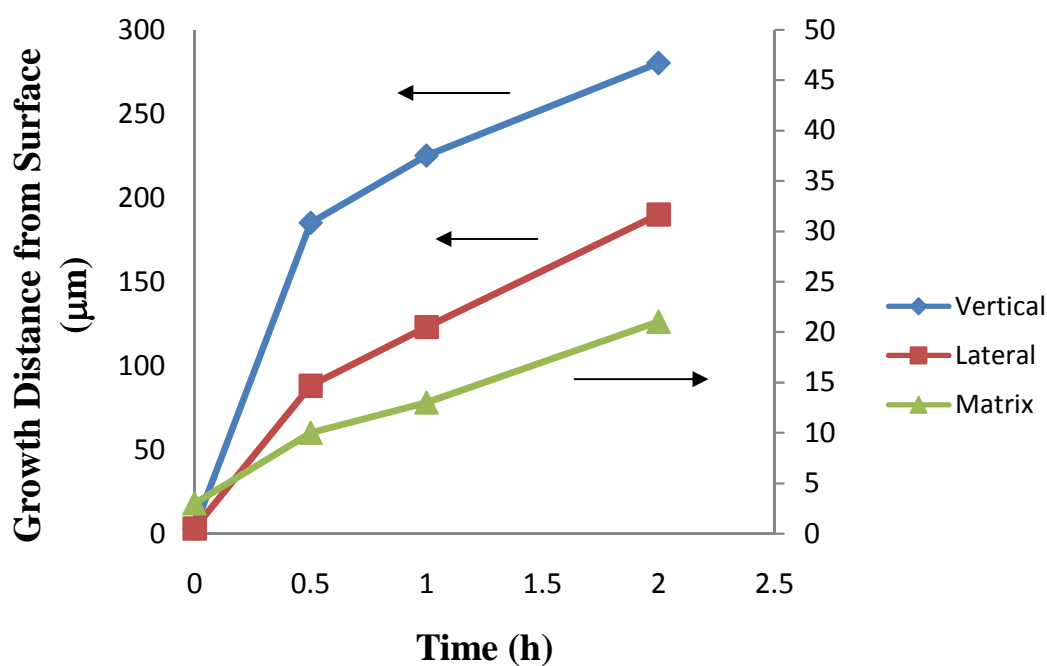


Figure 3-7: Vertical and lateral growth distances as a function of time at 1300°C in air for 150 nm TiO₂ doped BaTiO₃ sample from 0.5 to 2 h.

Figure 3-8 shows the kinetics of the matrix coarsening as a function of time plotted according to the general grain growth law:¹⁸

$$G^n - G_0^n = kt \quad 3.1$$

where G is the grain size at time t , G_0 is the original matrix grain size, k is a material constant (derived from the slope of the lines), and n is the grain growth exponent. In this case, $G \gg G_0$ therefore the equation can be reduced to: $G^n = kt$. A plot of $\log G$ vs. $\log t$ (Figure 3-8) yields a slope, $1/n = 0.535$; therefore $n \sim 2$. For typical ceramic systems the value of n ranges from 2 – 4. An n value of 2 corresponds to the matrix coarsening in a pure system (no second phases) under solid state sintering conditions.¹⁸

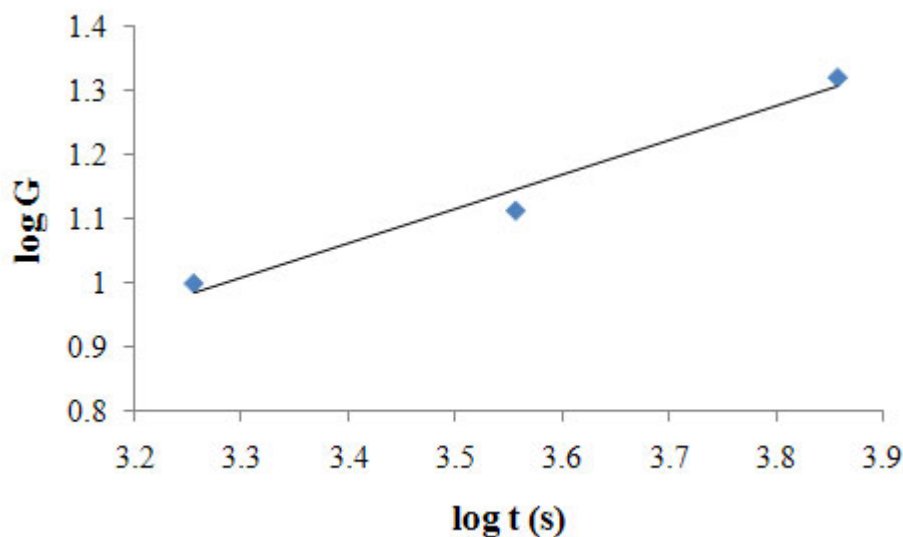


Figure 3-8: Grain growth kinetics of matrix coarsening in BaTiO_3 plotting $\log G$ vs. $\log t$ to determine the value of n .

It is interesting to note that there were no $\{111\}$ twin lamella observed within the large grains (Figure 3-6). This is contrary to the observation of Jung et al. for exaggerated grains in BaTiO_3 samples fired below the eutectic temperature.¹² Instead, the data collected here are more similar to that reported by Dillon et al. for the coarsening behavior of doped alumina. In that work, localized grain growth was found in Al_2O_3 samples fired under solid state sintering conditions. They attributed this effect to the

diffusion of the dopants along the grain boundaries and the formation of a second phase that caused an enhanced boundary mobility.^{19,20} A comparable phenomenon apparently occurs in BaTiO₃ with localized TiO₂ doping. The diffusion along the grain boundaries and the coarsening of the matrix grains apparently reduces the dominance of grains with [111] twins in the microstructure.

The microstructure of a BaTiO₃ sample with a 150 nm thick TiO₂ surface layer that was fired in air at 1350°C for 30 min is shown in Figure 3-9. The diffusion affected zone for the 150 nm, 1350°C sample increased compared to samples with 150 nm TiO₂ fired at 1300°C. It was found that the large grains increased in size from 170 μm at 1300°C to 280 μm at 1350°C. The amount and size of the abnormal grains is consistent with observations by Rios et al.,¹⁶ who studied the effect of excess TiO₂ on exaggerated grain growth in BaTiO₃.

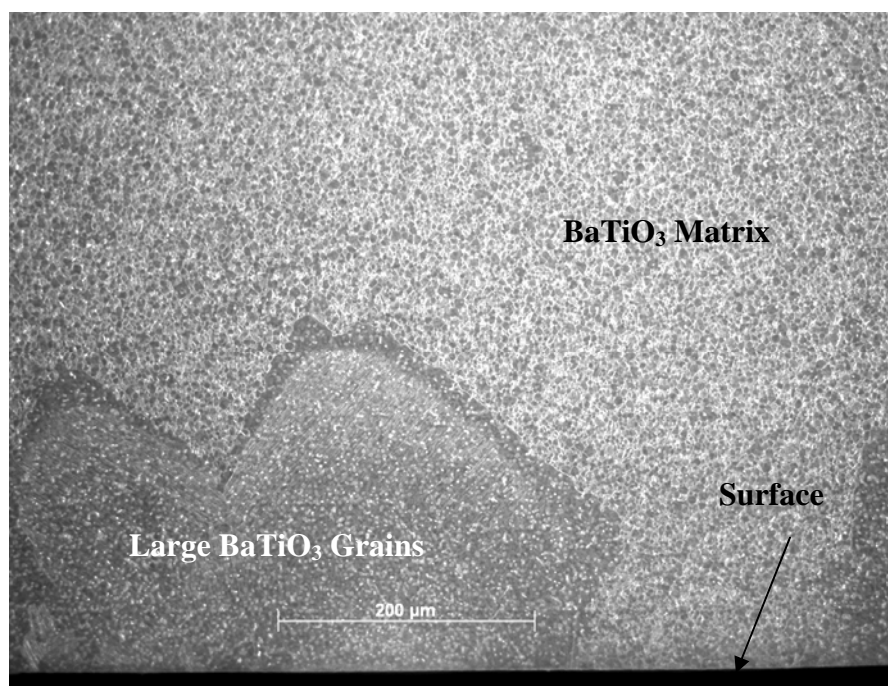


Figure 3-9: Optical image of 150 nm TiO₂ surface doped BaTiO₃ fired in air to 1350°C for 0.5 h.

To control matrix coarsening and the extent of enhanced grain growth, the experiment was repeated in a lower oxygen atmosphere, since Polatai et al.¹⁴ showed that firing BaTiO₃ in a reducing environment limits grain growth. Thus greater control of surface enhanced grain growth could be possible by avoiding matrix coarsening.

BaTiO₃ samples prepared with 50 nm, 100 nm, and 150 nm thick TiO₂ layers were fired between 1250°C and 1300°C in a PO₂ of 1x10⁻⁵ atm. Similar to the air-fired samples, no enhanced grain growth occurred in the 1250°C samples. However, there were some differences in the 1300°C samples fired at the lower oxygen partial pressure. Figure **3-10** shows representative SEM micrographs of the samples with 50 nm, 100 nm, and 150 nm TiO₂ layers fired to 1300°C for 0.5 h. The 50 nm and 100 nm samples showed diffusion affected zones indicative of accelerated coarsening. The diffusion affected zone is less than 40 μm, this indicates that less than 100 nm TiO₂ does have an effect on grain growth, even though no diffusion affected zone was observed for the samples fired in air for the same amount of TiO₂.

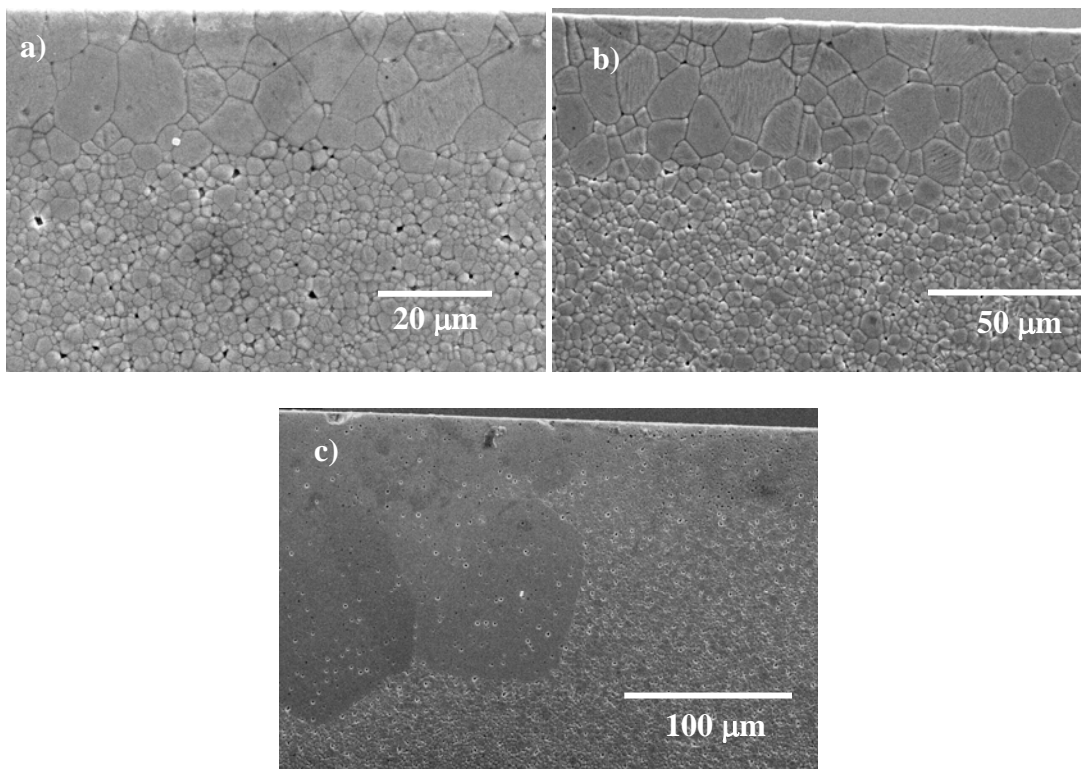


Figure **3-10**: SEM micrographs of the samples with a) 50 nm, b) 100 nm, and c) 150 nm thick TiO_2 layers fired to 1300°C for 0.5 h in a PO_2 of 1×10^{-5} atm.

When comparing the ceramics with a 150 nm thick TiO_2 layer fired in the reducing environment (Figure **3-10c**) and air (Figure **3-6**), the microstructure shows about the same diffusion affected zone. The 150 nm TiO_2 doped BaTiO_3 samples fired in both atmospheres produced large elongated grains (~ 100 's of microns) with about the same layer thicknesses of enhanced grain growth for short firing times, as shown in Figure **3-11**. The onset of the larger grains corresponds well with the samples fired in air, where the onset of the grain enhancement began above a TiO_2 thickness of 100 nm. The diffusion affected zone is comparable to the samples fired in air. Figure **3-11** shows the vertical grain growth enhancement distance as a function of time for the samples fired in air and in the reduced oxygen atmosphere. As the concentration of TiO_2 increased, the size of the enhanced grains increased as did the thickness of the diffusion affected zone. This corresponds well with previous reports on TiO_2 doping of BaTiO_3 by Rios et al.¹⁶

The remaining matrix grains did not significantly coarsen even after to 2 h at 1300°C in PO_2 of 1×10^{-5} atm. This may be explained by the reduction of grain boundary mobility in the lower oxygen content.¹³ The 50 nm and 100 nm TiO_2 layers samples fired in a PO_2 of 1×10^{-5} atm showed no significant lateral growth (on the order of 5 μm after 2 h at 1300°C) and illustrated in Figure 3-12; however for the 150 nm thick TiO_2 layer, the amount of lateral growth was the same as the air fired samples. The anisotropy in the diffusion affected zone between the <100 nm TiO_2 samples and the 150 nm TiO_2 samples heated in 1×10^{-5} atm PO_2 could be caused by the change in grain boundary diffusion. When the concentration of TiO_2 is above 100 nm, the results in Figure 3-10 indicate an increase in grain boundary diffusion resulting in exaggerated grain growth (the large anisotropic grains in Figure 3-10c). Below this concentration isotropic matrix coarsening occurs, resulting in a smaller diffusion affected zone.

For all the conditions when a diffusion affected zone was observed, there are several layers of grains that have coarsened due to the TiO_2 doping (i.e. the large grain size layers are *not* a single grain in thickness). This indicates that the TiO_2 diffuses along the grain boundaries several layers deep into the BaTiO_3 as the grains are coarsening. The final boundary between the enhanced grains and the remaining matrix grains can then be related to the diffusion depth of the TiO_2 .

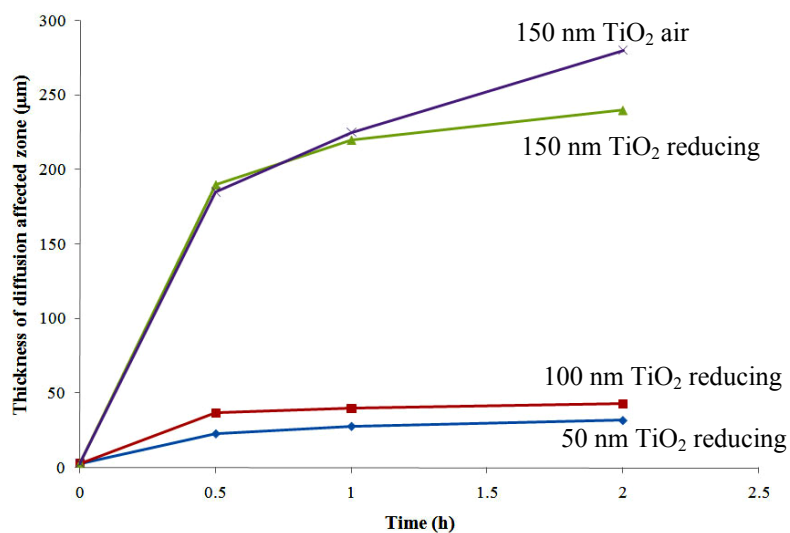


Figure 3-11: Growth of diffusion affected zone as a function of time for the samples fired in air at 1300°C and PO_2 of 1×10^{-5} atm (red.).

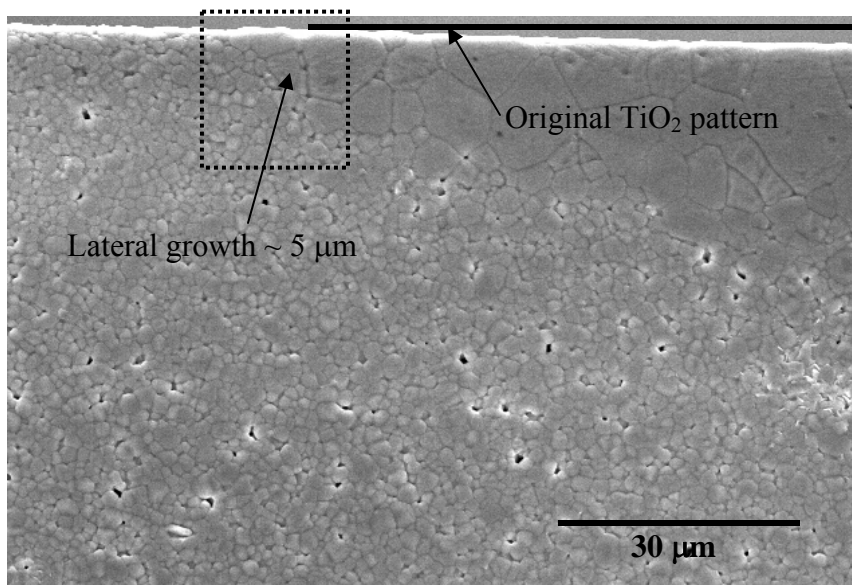


Figure 3-12: SEM micrograph of the sample with 100 nm thick TiO₂ layer fired to 1300°C for 2 h in a PO_2 of 1×10^{-5} atm.

A 150 nm thick patterned TiO_2 layer on a BaTiO_3 was fabricated and fired at 1350°C for 0.5 h. The cross section by optical microscopy is shown in Figure 3-13. Each patterned area shows several elongated grains across the enhanced region (as was previously seen from Figure 3-9). The rectangular boxes on the top of the image (surface of the sample) show the original location of the TiO_2 dopant.

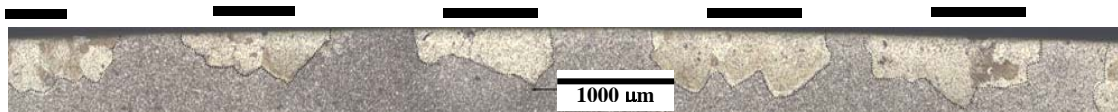


Figure 3-13: Cross section of a 150 nm TiO_2 surface patterned BaTiO_3 fired at 1350°C for 0.5 h in PO_2 of 1×10^{-5} atm. The black bars on the top indicate the position of the original TiO_2 patterns.

To test whether the large grains show preferred orientation for the growth direction, the diffusion affected zone was characterized by electron backscatter diffraction (EBSD). Figure 3-14 shows the EBSD pattern and the corresponding section of the BaTiO_3 sample. The EBSD pattern shows that the grains are randomly oriented and that there is no preferred orientation for the large grains at the surface.

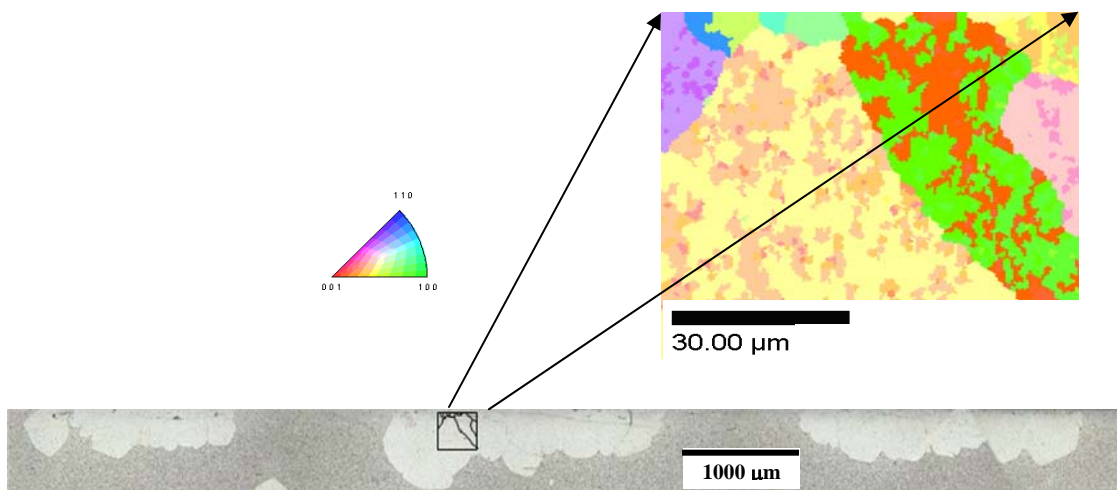


Figure 3-14: EBSD image of 150 nm TiO_2 surface patterned BaTiO_3 fired at 1350°C for 1 h in air showing the orientation of the diffusion affected zone.

3.4 Conclusions

Conditions for producing localized enhanced grain growth were determined for TiO₂-doped BaTiO₃. The magnitude of the diffusion affected zone was directly related to the amount of the TiO₂ deposited on the surface of the dense BaTiO₃, and the growth atmosphere. For TiO₂ concentrations below 100 nm there was no noticeable diffusion affected zone when fired in air at 1300°C. However, for the same concentrations of TiO₂ (below 100 nm) the thickness of the diffusion affected zone was ranged from 20 – 50 μm for samples fired in a PO₂ of 1x10⁻⁵ atm. For samples fired in both air and in the PO₂ of 1x10⁻⁵ atm, with TiO₂ concentrations above 150 nm the thickness of the diffusion affected zone reached ~100's μm. For all TiO₂ concentrations, when the samples were fired to 1350°C, the diffusion affected zone was indistinguishable from the rest of the matrix, due to a high average matrix grain size. The coarsening of the matrix away from the diffusion affected zone was reduced for all samples fired in a PO₂ of 1x10⁻⁵ atm. The patterned diffusion affected zone grain structure did not result in a preferred orientation of the large surface – nucleated BaTiO₃ grains.

3.5 References

1. Henry, E.C. and A.V. Illyn, "Some Relations Between Grain Size and Properties in High-Purity Barium Titanate Ceramics," *J. Can. Ceram. Soc.*, **34**: 137-41 (1965).
2. Jaffe, B., W.R. Cook, and H. Jaffe, Piezoelectric Ceramics. 1971, Marietta, OH: R.A.N. Publishers.
3. Arlt, G., D. Hennings, and G. de With, "Dielectric Properties of Fine-Grained Barium Titanate Ceramics," *J. Appl. Phys.*, **58**[4]: 1619-25 (1985).
4. Frey, M.H. and D.A. Payne, "Grain-Size Effect on Structure and Phase Transformations for Barium Titanate," *Phys. Rev. B: Condensed Matter*, **54**[5]: 3158-68 (1996).

5. Frey, M.H., Z. Xu, P. Han, and D.A. Payne, "The Role of Interfaces on Apparent Grain Size Effect on the Dielectric Properties for Ferroelectric Barium Titanate Ceramics," *Ferroelectrics*, **206**[1-4]: 337-53 (1998).
6. Demartin, M. and D. Damjanovic, "Dependence of the Direct Piezoelectric Effect in Coarse and Fine-Grained Barium Titanate Ceramics on Dynamic and Static Pressure," *Appl. Phys. Lett.*, **68**[21]: 3046-8 (1996).
7. Wada, S., K. Takeda, T. Muraishi, H. Kakemoto, T. Tsurumi, and T. Kimura, "Preparation of [110] Grain Oriented Barium Titanate Ceramics by Templated Grain Growth Method and Their Piezoelectric Properties," *Jap. J. Appl. Phys.*, **46**[10B]: 7039-43 (2007).
8. Du, X.-H., Q.-M. Wang, U. Belegundu, A. Bhalla, and K. Uchino, "Crystal Orientation Dependence of Piezoelectric Properties of Single Crystal Barium Titanate," *Mater. Lett.*, **40**: 109-13 (1999).
9. Damjanovic, D., M. Budimir, M. Davis, and N. Setter, "Piezoelectric Anisotropy: Enhanced Piezoelectric Response along Nonpolar Directions in Perovskite Crystals," *J. Mater. Sci.*, **41**: 65-76 (2006).
10. Davis, M., D. Damjanovic, D. Hayem, and N. Setter, "Domain Engineering of the Transverse Piezoelectric Coefficient in Perovskite Ferroelectrics," *J. Appl. Phys.*, **98**: 1-9 (2005).
11. Fullman, R.L., "Measurement of Particle Sizes in Opaque Bodies," *J. Metals*, **3**: 447-52 (1953).
12. Jung, Y.-I., S.-Y. Choi, and S.-J. Kang, "Grain-Growth Behavior During Stepwise Sintering of Barium Titanate in Hydrogen Gas and Air," *J. Am. Ceram. Soc.*, **86**[12]: 2228-30 (2003).
13. Jung, Y.-I., S.-Y. Choi, and S.-J.L. Kang, "Effect of Oxygen Partial Pressure on Grain Boundary Structure and Grain Growth Behavior in BaTiO₃," *Acta. Mater.*, **54**[10]: 2849-55 (2006).
14. Polotai, A., K. Breece, E. Dickey, C. Randall, and A. Ragulya, "A Novel Approach to Sintering Nanocrystalline Barium Titanate Ceramics," *J. Am. Ceram. Soc.*, **88**[11]: 3008-12 (2005).
15. Park, E.T., "Grain Growth of BaTiO₃," *J. Mater. Sci. Letters*, **18**: 163-5 (1999).
16. Rios, P.R., T. Yamamoto, T. Kondo, and T. Sakuma, "Abnormal Grain Growth Kinetics of BaTiO₃ with an Excess of TiO₂," *Acta. Mater.*, **46**[5]: 1617-23 (1998).

17. Matsuo, Y. and H. Sasaki, "Exaggerated Grain Growth in Liquid-Phase Sintering of BaTiO₃," *J. Am. Ceram. Soc.*, **54**[9]: 417 (1971).
18. Rahaman, M.N., Ceramic Processing and Sintering. 1995, NY: Marcel Dekker Inc.
19. Dillon, S.J. and M.P. Harmer, "Relating Grain-Boundary Complexion to Grain-Boundary Kinetics I: Calcia-Doped Alumina," *J. Am. Ceram. Soc.*, **91**[7]: 2304-13 (2008).
20. Dillon, S.J. and M.P. Harmer, "Relating Grain-Boundary Complexion to Grain-Boundary Kinetics II: Silica-Doped Alumina," *J. Am. Ceram. Soc.*, **91**[7]: 2314-20 (2008).

Chapter 4

Patterned Solid State Growth of BaTiO₃ Crystals

4.1 Introduction

As reviewed in Chapter 3, textured BaTiO₃ ceramics have improved piezoelectric properties of BaTiO₃ ceramics. Both the work of Wada et al.¹ in producing textured BaTiO₃, and the previous studies aimed at producing BaTiO₃ single crystals,²⁻⁶ utilized a liquid phase to facilitate grain growth. It was shown in Chapter 3 that enhanced growth of BaTiO₃ can be accomplished locally by surface doping with TiO₂, without influencing the remaining matrix. This enables the TiO₂ doped BaTiO₃ to coarsen locally by diffusion of the TiO₂ along the grain boundaries while the matrix coarsens by solid state sintering during heat treatments. However, the surface doping process described in Chapter 3 does not enable control over the *orientation* of the growing grains.

This chapter reviews studies to tailor orientation development from the surface in BaTiO₃ by the control over the shape, distribution and orientation of the templates. The orientation was accomplished by using BaTiO₃ single crystals as templates. Optical photolithography was employed to pattern the BaTiO₃ crystals which were then bonded to a dense BaTiO₃ ceramic to control the orientation and distribution of grains in BaTiO₃. The kinetics of single crystal growth in both the vertical and lateral directions from the patterned crystal into the ceramic was measured. This information provides an understanding of the range of microstructures that can be produced using this approach.

4.2 Experimental Procedure

4.2.1 Patterned Single Crystal Template Fabrication

Matrices for patterned growth are the same as those described in Chapter 3. For template formation, BaTiO₃ single crystal (Deltronics Co., Dover, NJ, or Dr. Haosu Luo, Shanghai Institute of Ceramics, Shanghai, China) were cut and polished along the [100] or [110] directions. The polishing procedure was identical to that used for the matrix samples. The polished single crystals were measured by back reflection Laue (Multiwire Laboratories, Ltd., Ithaca, NY) to confirm that the correct orientation was achieved. This provided orientation within ± 2 degrees.

The polished BaTiO₃ crystal substrate was cleaned in acetone and a 25 nm thick amorphous TiO₂ sol-gel layer was applied by spincoating. The 0.25 M TiO₂ solution was prepared by mixing titanium (IV) isopropoxide with 2-methoxyethanol (2-MOE) under argon at room temperature for 2 h. Two ml acetylacetone was added to 2.8 g titanium (IV) isopropoxide for stabilization. The TiO₂ solution was spin coated at 4000 rpm for 30 s to produce a 25 nm thick layer on the polished single crystal BaTiO₃ surface. This was the smallest thickness able to be produced with the 0.25 M solution for crystal growth experiments.

The removal of the solvents in the TiO₂ sol-gel layer was accomplished by heating the BaTiO₃ single crystals in air (Thermolyne 47900, Barnstead Thermolyne, Dubuque, IA). To avoid cracking the single crystals, the samples were heated at 2°C/min to 100°C, 0.1°C/min to 140°C, 5°C/min to 350°C and cooled in the reverse order.

The TiO₂ coated single crystal substrates were then sputter coated with a 100 nm nickel seed layer (Kurt Lesker CMS-18, Clairton, PA) using the conditions listed in Table 4-1. A photoresist (AZ-1827) was spin coated on the nickel seed layer at 4000 rpm for 40 s to produce a photoresist layer 3 microns thick. The sample was soft-baked at 100°C for 1 min on a hotplate, then exposed to UV light for 6 s (Karl Suss MA6 Contact Aligner). The photoresist was developed (MF-CD-26) to produce the 1000 μm line pattern (similar to Figure 3-1) for 40 s, and then hard-baked at 100°C for 2 min.

Table 4-1: Conditions for nickel sputter deposition.

	Ni 1000 Å gun 1 (or 2)
Temperature	25°C
Dwell to Reach Temperature	600 s
Forward Power	199 W
Reflected Power	6 W
DC Bias	249 V
Pressure	5 mTorr
Atmosphere	Ar
Target to Substrate Distance	20 cm
Deposition Time	1060 s

Nickel was then electroplated onto the exposed nickel seed layer by suspending the BaTiO₃ single crystal, housed in a copper home-made basket, into the nickel salt solution. An AC power source (Agilent HP 8662 signal generator, Santa Clara, CA) was attached and set to a current of 0.2 milliamps for the first 5 minutes. The initial low current for the first 5 minutes was to promote adhesion of the deposited nickel to the nickel seed layer. The current was increased to 0.5 milliamps for 25 – 30 min. The electroplated sample was washed with deionized water and removed from the copper housing. This produced a total nickel thickness of 3 μm.

After nickel electroplating, the photoresist was removed with acetone and the sample was etched via inductively coupled plasma – reactive ion etching (ICP-RIE, Applied Materials DPS, Santa Clara, CA). The BaTiO₃ single crystal was bonded to an 8” silicon carrier wafer with silver conductive paint (Electron Microscopy Sciences, Hatfield, PA) for loading and etching in the ICP-RIE using the conditions listed in Table 4-2. Etching for 8 h produced a 1 μm template relief. The etch rates for the BaTiO₃ were 0.125 μm/h and the nickel mask was 0.3 μm/h. This resulted in ~ 0.5 μm of remaining nickel on the surface of the BaTiO₃ after the 8 h of ICP-RIE etching. After etching, the silver paste was dissolved using acetone and the etched BaTiO₃ single crystal was removed from the silicon wafer. The remaining nickel was removed with a combination of HNO₃ (70%, J.T. Baker, Phillipsburg, NJ) and HCl (38%, J.T. Baker) in a

3:1 ratio, then diluted with deionized water in the ratio of 10:1 for a total of 10 s. The removal of the nickel by the acids did not etch or leach the patterned BaTiO₃ single crystal.

Table 4-2: ICP-RIE conditions for producing single crystal templates.

Parameter	Conditions
Temperature	25°C
ICP Power	800 W
Bias (RF Power)	50 W
Gases	Cl ₂ at 20 sccm
Pressure	10 mTorr
Wafer cooling (He)	6 Torr
Etching time	8 h

Figure 4-1 shows a schematic of the overall procedure for processing the single crystal templates. Figure 4-2 shows the top surface of an etched single crystal template with a pattern consisting of 1000 μm lines separated by 1000 μm.

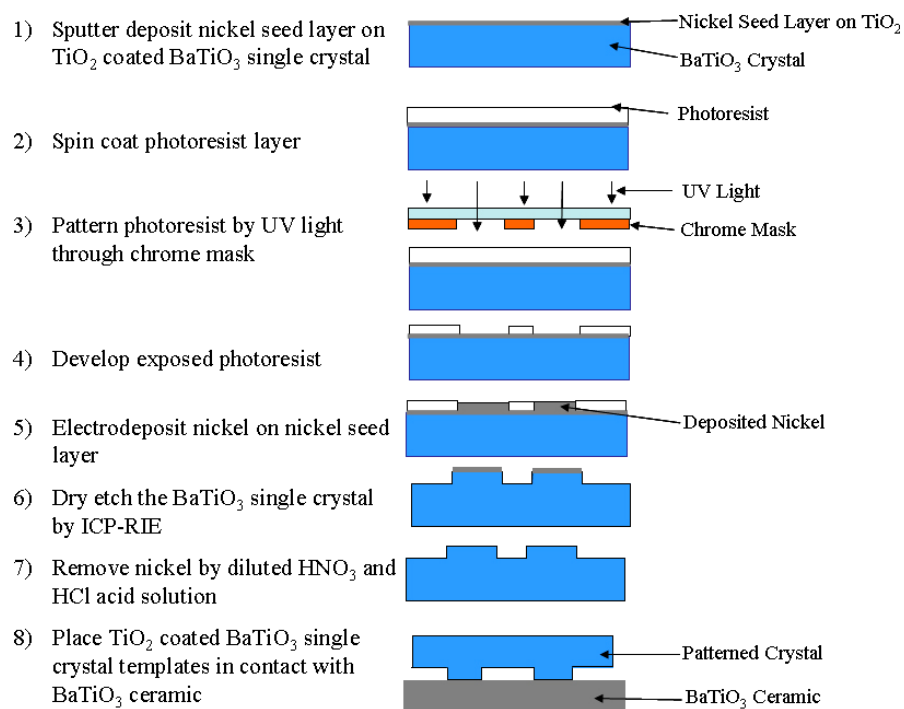


Figure 4-1: Schematic of the template fabrication process.

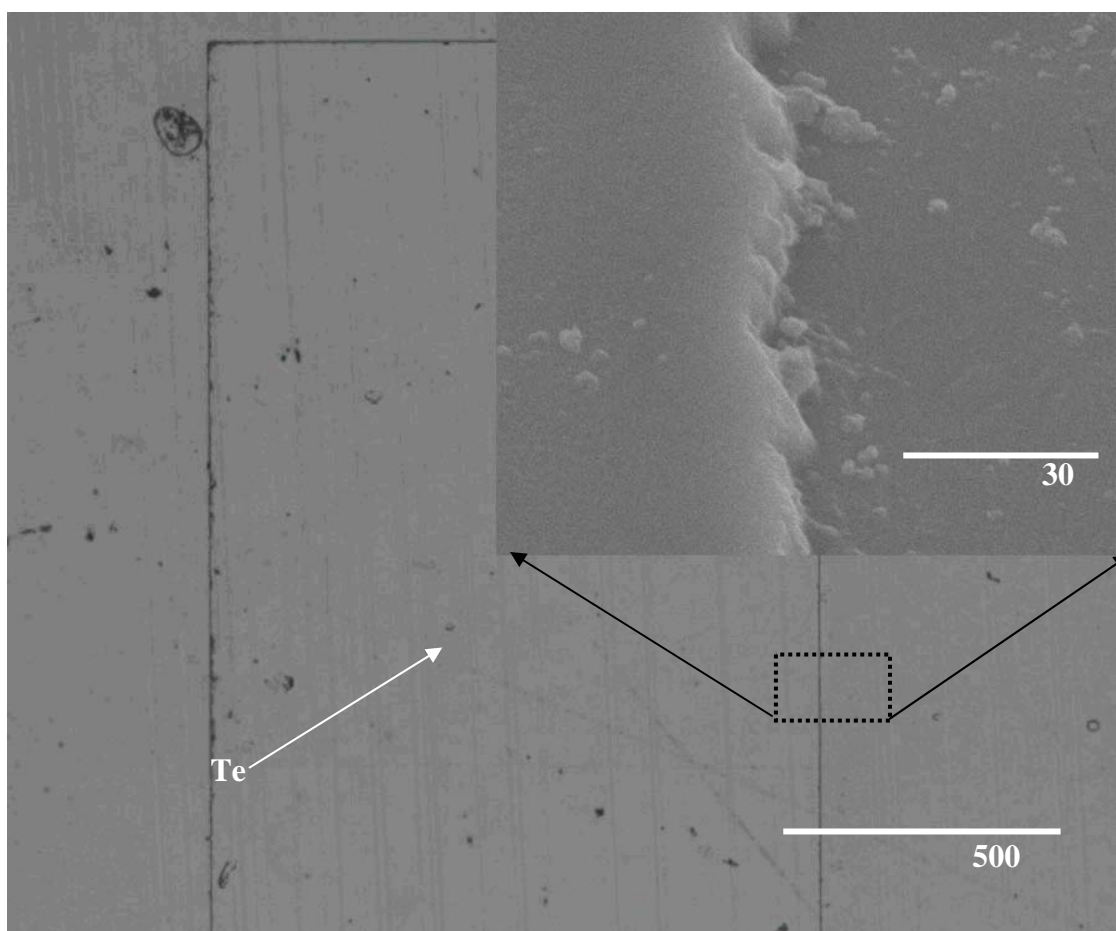


Figure 4-2: Optical image of the etched single crystal showing a line pattern.

4.2.2 Bonding and Growth of BaTiO₃ Template Crystals

The patterned BaTiO₃ single crystal was bonded to the polycrystalline BaTiO₃ matrix of 2 μm grain size between 1250°C – 1350°C for 2 h in air and in a controlled atmosphere ranging from a PO₂ of 1×10^{-5} atm to 1×10^{-18} atm. In order to maintain contact between the single crystal and matrix during bonding, a 40 gram mass was placed on top of the single crystal. The setup, including the placement of the single crystal, polycrystalline matrix, the platinum foils and weight is shown in Figure 4-3.

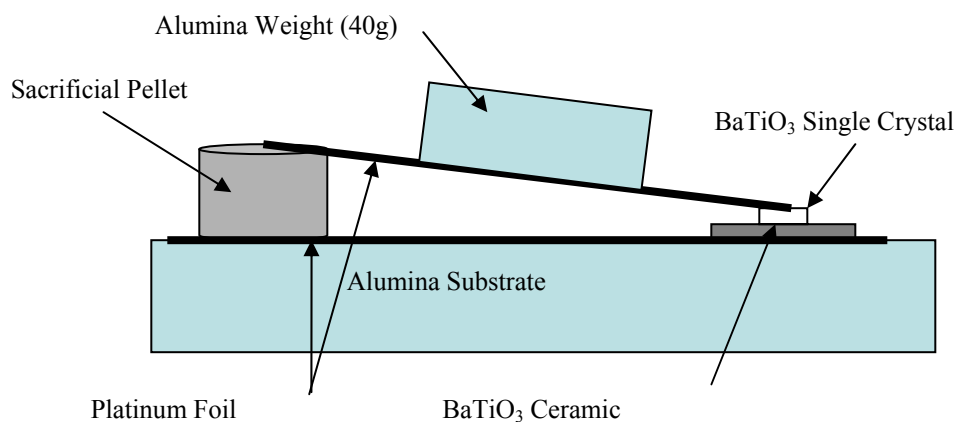


Figure 4-3: Schematic of the setup for bonding the BaTiO₃ polycrystalline matrix to the patterned single crystal.

The platinum foils were used to prevent the BaTiO₃ samples from adhering to the alumina substrates and alumina weight. For this set up, the BaTiO₃ ceramic was roughly 10 mm x 10 mm x 2 mm. For each bonding run, the etched BaTiO₃ single crystals were placed on top of the polycrystalline ceramic. The etched single crystal dimensions were roughly 9 mm x 3 mm with a thickness of 2 – 3 mm. Based on the length and the pattern dimensions (Figure 4-2), there were approximately 4 line patterns per etched single crystal sample.

Single crystal growth was conducted between 1250°C – 1300°C for dwell times up to 10 h in PO₂ ranging from 1x10⁻⁵ atm – 1x10⁻¹⁸ atm. The patterned samples were characterized by optical microscopy (BX60M, Olympus with AxioCam by Carl Zeiss), scanning electron microscopy (S-3500N and S-3000H, Hitachi), and electron backscattered diffraction (EBSD).

4.3 Results and Discussion

Initial experiments to determine the optimal conditions for bonding a single crystal BaTiO₃ (with either [100] or [110] orientation) to the polycrystalline matrix were examined. The bonding attempts were conducted with a polished BaTiO₃ single crystal and a polycrystalline BaTiO₃ ceramic at 1350°C for 2 h in air. Attempts were made to induce crystal growth with and without a 25 nm TiO₂ interface layer. This was done to determine what effect the matrix coarsening from the TiO₂ additions has on the growth rate of single crystal conversion.

Figure 4-4 shows examples of bonding a [100] BaTiO₃ single crystal to the matrix material (a) with and (b) without a 25 nm thick TiO₂ layer. The samples were heated to 1350°C in air and show more area bonded and converted for the case with a TiO₂ interface layer after a 2 h dwell. In both images, the regions where bonding and conversion of the matrix material was achieved are circled. The more successful bonding and growth run was with the TiO₂ addition, indicating that the interfacial layer between the two materials aids in maintaining contact at the interface and promotes a more intimate contact for bonding and single crystal growth to occur. It should be noted that in previous work by Rehrig et al.,⁴ bonding and growth of the single crystal was accomplished without an interfacial layer and with no applied load. The difference between this study and Rehrig et al.'s is the Ba/Ti ratio of the BaTiO₃ matrix. Rehrig et al. used a Ba/Ti ratio of 0.95, which would be expected to produce a significant amount of liquid phase above the eutectic temperature. In this work, the Ba:Ti ratio in the BaTiO₃ matrix is 0.996. Elimination of the excess Ti throughout the matrix helps to keep the liquid phase localized, and so improves the control of the process (though at the expense of single crystal growth rate). The addition of a TiO₂ interface layer is used to compensate for the lower Ti content in the matrix.

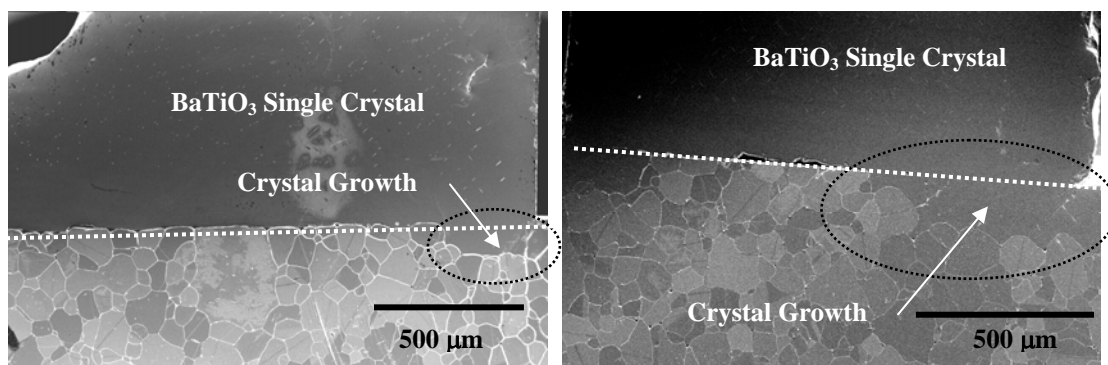


Figure 4-4: SEM images of a BaTiO₃ single crystal bonded in air at 1350°C for 2 h (a) without and (b) with a TiO₂ interface layer. The dotted line indicates the initial interface between the single crystal and ceramic.

Growth in air (Figure 4-4) at 1350°C yielded significant matrix coarsening, with an average grain size approaching 50 – 100 μm. This significantly reduced the driving force for crystal conversion and limited the single crystal growth to only 200 μm in depth.

To minimize matrix coarsening during sintering, additional bonding and growth experiments were conducted as a function of atmosphere. Figure 4-5 shows the vertical growth rate for the single crystal conversion in BaTiO₃ as a function of PO₂ using a [001] BaTiO₃ crystal. All samples were heated at 1300°C for 2 h at each PO₂ level. The general trend shows that with decreasing oxygen partial pressure in the ambient, the crystal conversion rate decreases non-linearly from a PO₂ of 0.2 atm to 1x10⁻¹³ atm. This can be attributed to the decrease in the diffusion of titanium due to a reduction in oxidation state from Ti⁴⁺ (~10⁻¹² cm²/s)⁷ to Ti³⁺ (~10⁻¹⁵ cm²/s)⁸ at 1200°C. Also, below a PO₂ of 1x10⁻¹³ atm there is no detectable single crystal growth after the 2 h dwell. This partial pressure of oxygen (i.e. PO₂ of 1x10⁻¹³ atm) corresponds well with Kang et al., where no abnormal growth occurs in a Ti-rich matrix below 1x10⁻¹³ atm. For all growth runs of 2 h at PO₂ below 1x10⁻⁵ atm, there was no detectable change in the grain size of the BaTiO₃ ceramic.

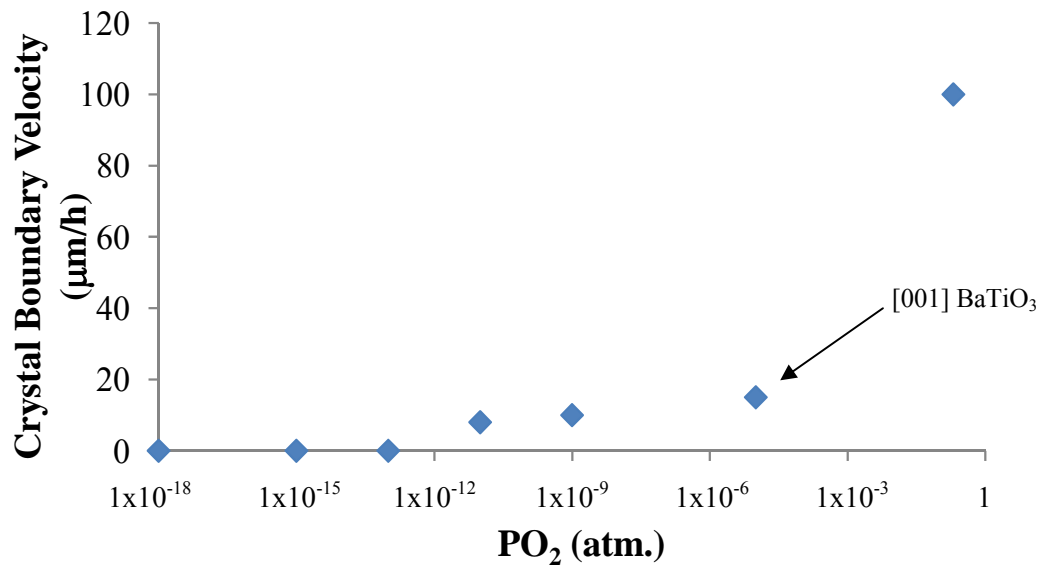


Figure 4-5: Crystal boundary velocity as a function of atmosphere for [001] BaTiO₃ single crystal conversion at 1300°C for 2 h dwell at each PO₂ level.

From the results shown in Figure 4-5, a PO₂ of 1x10⁻⁵ atm was chosen for crystal conversion times longer than 2 h since this oxygen partial pressure gave the highest crystal conversion rate without significant matrix coarsening. Growth runs with longer dwell times are needed to determine how the matrix coarsens for prolonged heating runs, and how single crystal conversion is affected. Figure 4-6 shows a dark field optical image of a [100] BaTiO₃ single crystal bonded to the polycrystalline matrix (with a 25 nm TiO₂ interfacial layer), with the inset image being an SEM image of the matrix material. The sample was heated at 1300°C in a PO₂ of 1x10⁻⁵ atm for 9 h. The conversion of the single crystal is clearly shown and has reached 600 μm, with complete bonding across the entire BaTiO₃ single crystal / ceramic interface. The SEM inset image shows the matrix material after the 9 h dwell is ~ 7 μm in size.

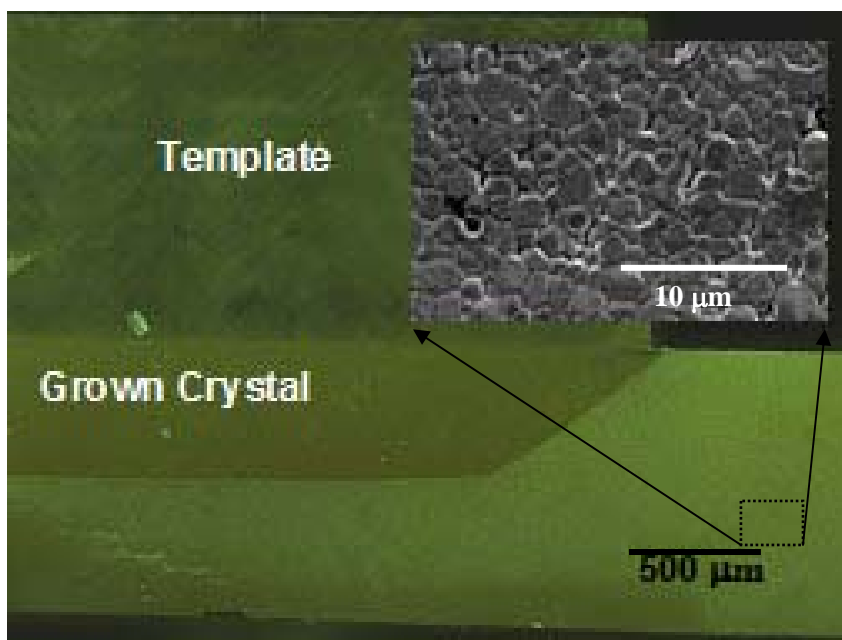


Figure 4-6: Optical image of the crystal grown from a [100] BaTiO₃ single crystal fired at 1300°C for 9 h in PO₂ of 1×10^{-5} atm, with an inset SEM image of the matrix material.

It is interesting to note that the matrix material has an average grain size of 7 μm after 9 h at 1300°C, which is significantly smaller than the ~100 μm grain size of samples heated in air after 2 h. The starting matrix material had a 2 – 3 μm average grain size (Figure 3-3). The fact that the single crystal boundary reached up to 600 μm indicates that the diffusion affected zone shown in Figure 3-10a,b from the TiO₂ deposited on the polycrystalline BaTiO₃ surface does not hinder the single crystal boundary growth. From Figure 3-10a,b using the depth of the diffusion affected zone with 50 nm and 100 nm TiO₂ the rate of the depth of the diffusion affected zone can be approximated as 40 μm/h and 80 μm/h, respectively. Since only 25 nm was used to bond the single crystal to the BaTiO₃ ceramic, then the rate of the diffusion affected zone's depth can be extrapolated to ~20 μm/h. After 9 h the diffusion affected zone would only reach ~180 μm. Thus, the conversion of the BaTiO₃ matrix to the single crystal orientation occurred before any

coarsening of the matrix from the TiO_2 took place since the converted matrix reached a distance greater than what the diffusion affected zone would indicate.

4.3.1 Patterned Single Crystal Growth

Crystal growth was measured on patterned single crystal templates using [100] and [110] BaTiO_3 single crystals with the same line pattern shown in Figure 3-1. This pattern was chosen to study the vertical and lateral growth rates for each template orientation in order to understand the kinetics involved with oriented crystal growth. Crystal and ceramic were bonded at 1300°C in PO_2 of 1×10^{-5} atm for 0.5 h. Subsequent growth runs were conducted at 1300°C in a PO_2 of 1×10^{-5} atm at various dwell times to measure the vertical and lateral growth rates, and observe the single crystal morphology. The combination of optical images in Figure 4-7 shows a patterned [110] single crystal bonded to the matrix material with the other images showing the amount of growth before and after an additional 3 h crystal growth run.

After the initial bonding run was accomplished, the single crystal / polycrystalline sample was cut lengthwise in half down the center of the etched single crystal. This corresponded to roughly 1.5 mm from the edge of the etched and bonded single crystal. This cross section surface was polished (in the same manner as outlined earlier) and thermally etched at 1200°C for 10 min to determine the initial growth achieved off of the templates from the bonding run. The grown distance became the starting point for all subsequent growth rate measurements. Also, by starting the analysis near the center of the etched and bonded single crystal, the subsequent vertical and lateral growth rates measured would not be influenced by already faceted boundaries of the converted crystal. After each single crystal growth run, the new converted crystal growth distance was measured by optical microscopy and SEM. This was accomplished since the boundary between the starting point, and the subsequent growth runs were observable optically due to differences in the surface roughness. The starting point (the initial grown crystal from bonding) would be smooth after the thermal etch process, while the subsequent grown

crystal would retain the thermally etched surface roughness from the individual grains prior to being converted.

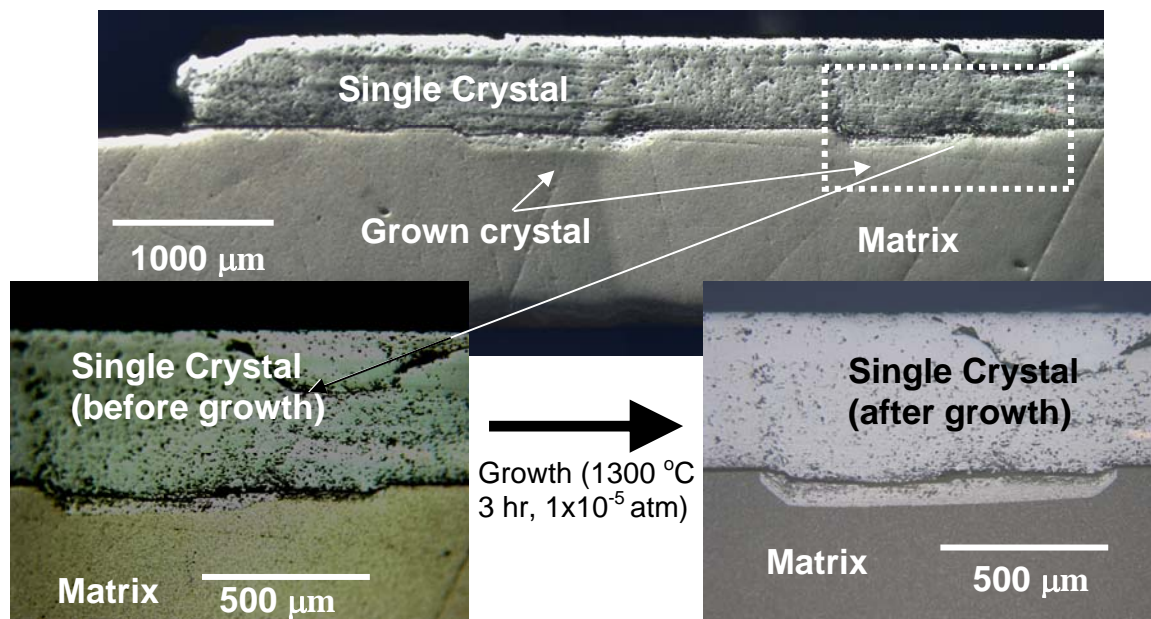


Figure 4-7: Optical images showing the patterned [110] BaTiO₃ crystal before and after a 3 h growth run at 1300°C in a PO₂ of 1x10⁻⁵ atm.

From the before and after images in Figure 4-7, it is clear that nucleation from the template was not homogeneous. This can be seen from the uneven growth front on the image just after the bonding run was completed. The inhomogeneous nucleation could have an effect on the final distribution of the oriented grown crystal in the matrix. The shape of the oriented growth from the templates would be different. For example, the grown converted crystal pattern will not consist of the “line” pattern (or any other potential patterned crystal shape). This will produce a pattern with only a portion of the templated sites oriented, with remaining matrix grains in areas where the templates did not initiate nucleation of the converted crystal. Work should be conducted in the future to achieve a more laterally homogenous nucleation.

From Figure 4-7, the vertical and lateral growth rates were measured from cut and polished cross sections after dwell times ranging from 0.5 h to 4 h at 1300°C in a PO₂ of

1×10^{-5} atm. Figure 4-8 shows the distance of the crystal conversion as a function of time at 1300°C in a PO_2 of 1×10^{-5} atm. The vertical growth rates were on the order of $10 - 15$ $\mu\text{m}/\text{h}$ and independent of the crystal orientation. The lateral growth rates, however, were dependent on the orientation of the single crystal ($10 - 15$ $\mu\text{m}/\text{hr}$ for $[100]$ and $5 - 10$ $\mu\text{m}/\text{h}$ for $[110]$). The reported growth rates are significantly slower than reported in literature. For example, Rehrig et al. showed that the initial growth rate of $[100]$ single crystal was $590 - 790$ $\mu\text{m}/\text{h}$, and after the equilibrium morphology is achieved it dropped to 30 $\mu\text{m}/\text{h}$.⁴ The major differences are that the $10 - 15$ $\mu\text{m}/\text{h}$ growth rates are observed for solid state sintering. Previous single crystal growth has been achieved in the presence of a liquid phase above 1332°C .^{2, 4, 9, 10} The diffusion rates for sintering in a liquid phase (i.e. $10^{-5} - 10^{-6}$ cm^2/s) are significantly faster compared to solid state growth (i.e. $10^{-9} - 10^{-12}$ cm^2/s) at 1200°C . In addition, the single crystal growth was not completed in air, as previous authors have done, but in a reducing atmosphere. The increase in Ti^{3+} concentration has been shown to reduce the grain boundary diffusion, thus slowing the single crystal conversion. Choi et al. showed that the excess Ti-excess doping would move with the single crystal boundary during liquid phase single crystal growth. The authors indicate that the growth kinetics of the single crystal would be affected by the presence of the excess Ti.¹¹ Thus, in the solid state single crystal growth the single crystal boundary kinetics could be slowed due to the excess amount of Ti^{3+} concentration centered around the growth boundary from the 25 nm TiO_2 layer.

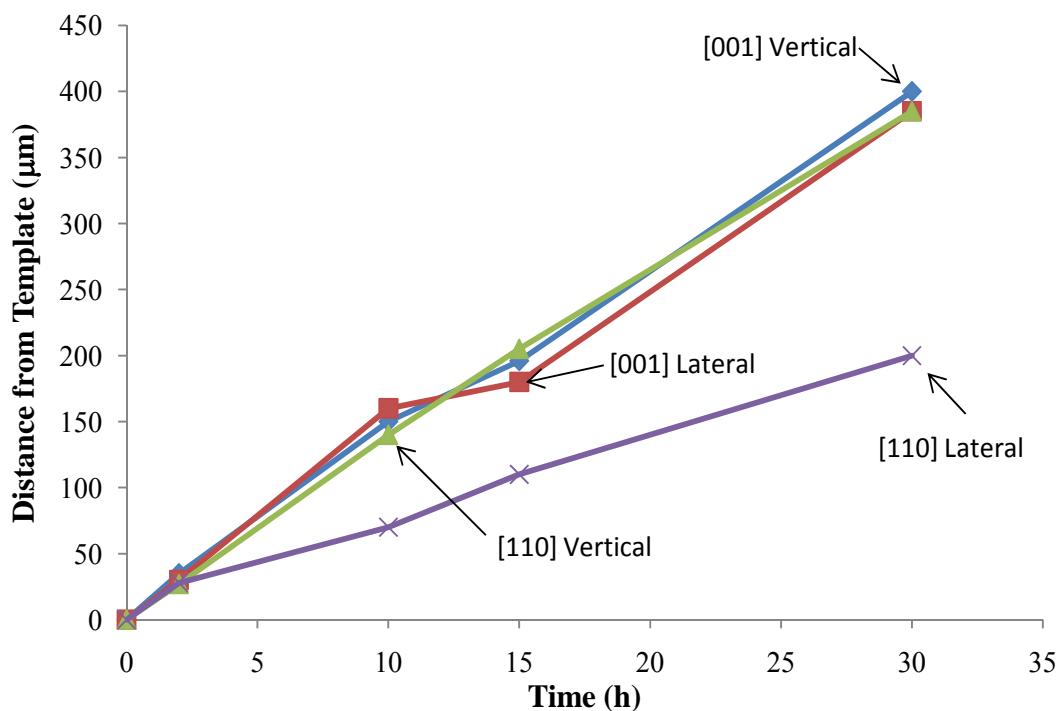


Figure 4-8: Distance of the crystal conversion as a function of time for the lateral and vertical directions with [001] and [110] single crystal templates at 1300°C in a PO_2 of 1×10^{-5} atm.

Continued growth runs were conducted at 1300°C in a PO_2 of 1×10^{-5} atm for 25 h, until the single crystal boundary equilibrium shape was obtained (Figure 4-9). This sample was cut, polished, and thermally etched at 1200°C for 10 min in PO_2 of 1×10^{-5} atm to show the converted crystal boundary (triangular shape growth). An additional 2 h dwell at 1300°C in a PO_2 of 1×10^{-5} atm was conducted to measure the change in boundary growth rate of the faceted planes. Figure 4-11 shows the dark field optical image of the same sample after the 2 h growth run. The brighter region along the faceted planes is the additional single crystal growth which occurred at an average rate of 10 $\mu\text{m}/\text{h}$. Unfortunately, the sample cracked near the single crystal / grown crystal boundary during cooling. This was most likely caused by the stress induced with the phase change at the Curie temperature. The observed needle-like structures (Figure 4-10) in the

BaTiO₃ single crystals are believed to be rutile crystallites from the excess TiO₂. The dark areas in Figure 4-10 are due to charging. The dark spot in the polycrystalline matrix is a defect from when the polycrystalline matrix was fabricated.

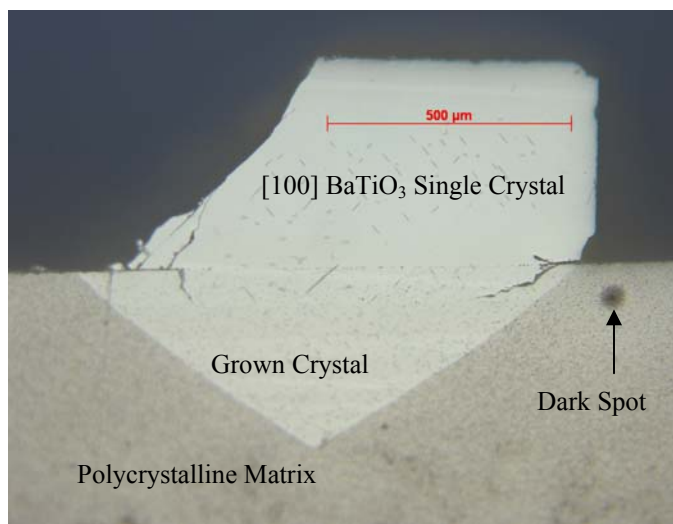


Figure 4-9: Optical image of the equilibrium morphology of the grown crystal from a [100] BaTiO₃ single crystal grown at 1300°C, PO₂ of 1x10⁻⁵ atm for 25 h.

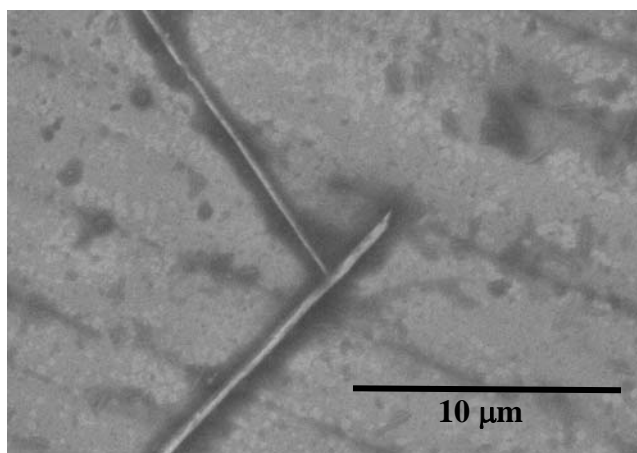


Figure 4-10: SEM image of the needle-like structures in the single crystal from the growth at 1300°C, PO₂ of 1x10⁻⁵ atm for 25 h run outlined in Figure 4-9.

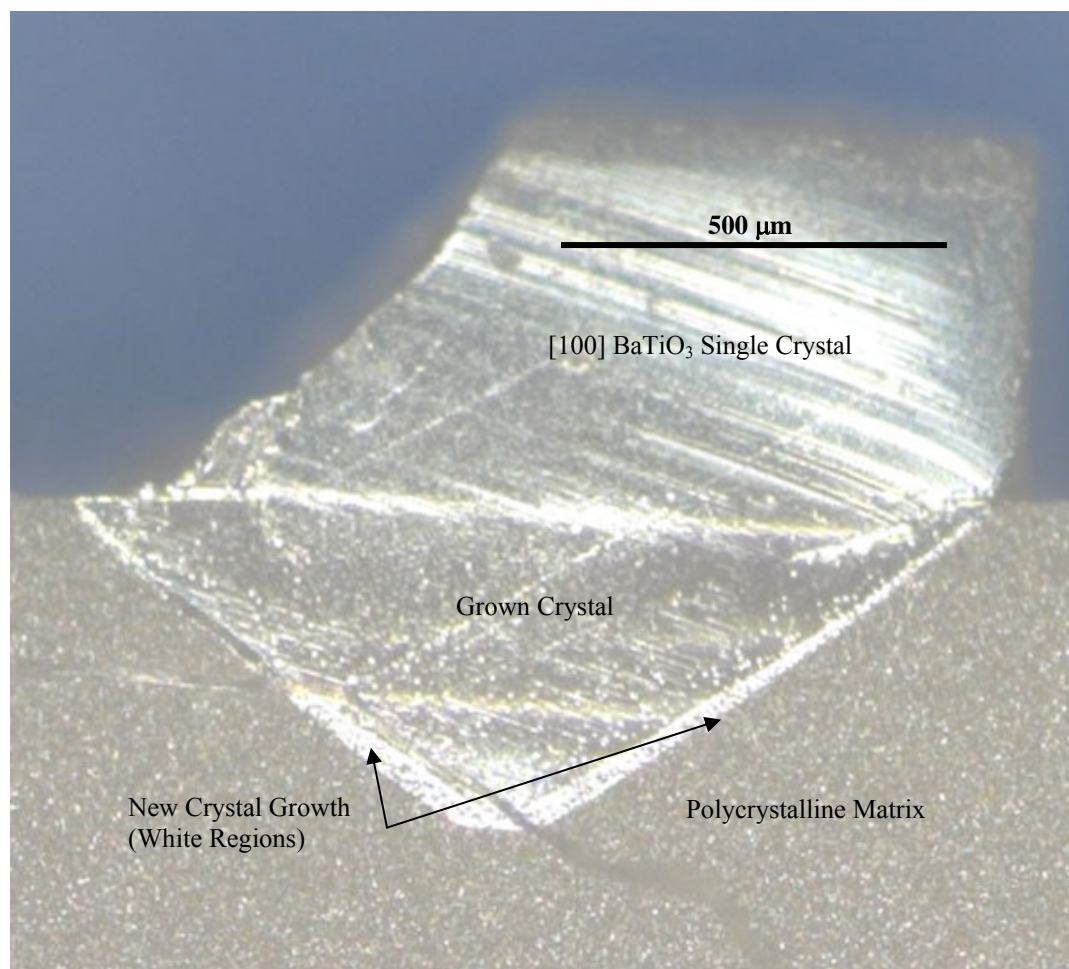


Figure 4-11: Optical image of the growth from the equilibrium morphology of the grown crystal from a [100] BaTiO₃ single crystal grown at 1300°C, PO₂ of 1x10⁻⁵ atm for an additional 2 h.

The growth rate of the single crystal boundary is the same (10 – 15 μm/h) after the equilibrium morphology has been achieved when grown at 1300°C and a PO₂ of 1x10⁻⁵ atm. This is in contrast to what has been previously observed by Rehrig et al., where the growth rate decreased substantially to 30 μm/h after the equilibrium morphology of the grown crystal is achieved.

Electron backscattered diffraction (EBSD) was conducted on the patterned single crystal growth sample from Figure 4-7 after an additional 25 h growth run at 1300°C in a

PO_2 of 1×10^{-5} atm. The image shown in Figure 4-12 indicates that the grown crystal boundary in the matrix is the same orientation as that of the single crystal template. The multi-coloration (indicative of matrix grains) in the bottom left of the EBSD image shows the random distribution of the matrix grains. The multiple colors shown in both the original single crystal and the grown crystal are due to a combination of 1) an artifact due to surface roughness of the polished sample and 2) the indexing of [110] or [101] domains from referencing to a tetragonal unit cell. It was found that the software analysis, when matching diffraction patterns, determined an incorrect orientation at the higher surface roughness locations based on SEM images (Figure 4-13). There are no matrix grains located in the grown single crystal.

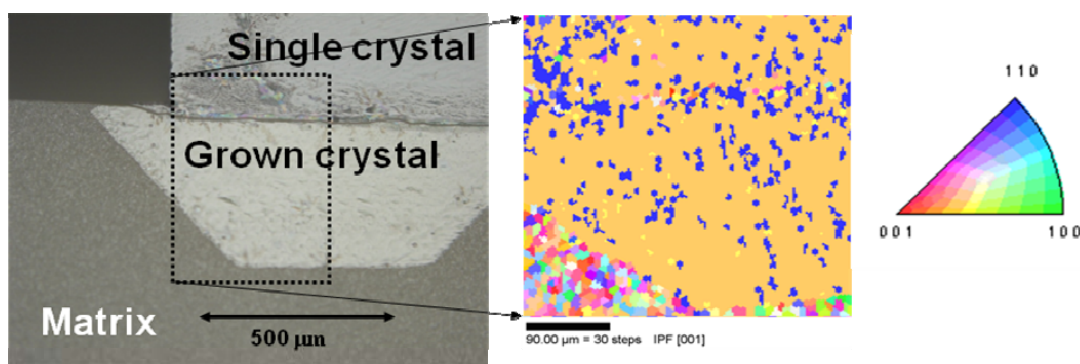


Figure 4-12: EBSD image showing the orientation of the grown crystal relative to the [100] template single crystal when heated to 1300°C for 25 h in PO_2 of 1×10^{-5} atm.

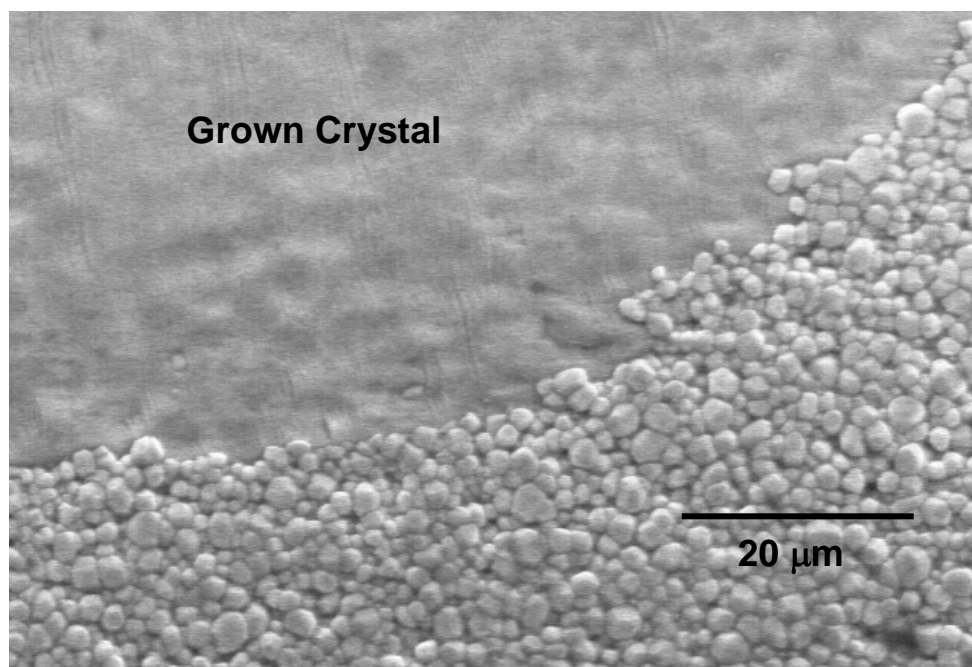


Figure 4-13: SEM image showing the surface roughness of the grown crystal when heated to 1300°C for 25 h in PO_2 of 1×10^{-5} atm.

4.4 Conclusions

A processing technique has been developed to control the spacing, and orientation for oriented crystal growth in BaTiO_3 by solid state conversion. A patterned single crystal with a 1000 μm line pattern array with a template relief of 1 μm was used to template crystal growth. Although the 1 μm template relief was successful, a deeper relief of at least 5 μm would be ideal. This would prevent any unwanted bonding and growth off of the etched single crystal into the polycrystalline matrix.

Orientation control was obtained with [100] and [110] BaTiO_3 single crystals. Conditions for bonding the single crystal templates to the matrix and optimal single

crystal growth with minimal matrix coarsening were determined to be at 1300°C in a PO₂ of 1x10⁻⁵ atmospheres. Various degrees of textured growth were developed and the grown crystal boundary velocity was measured. The grown crystal boundary growth rates were determined to be 10 – 15 μm/h for the vertical growth rates for both [100] and [110] orientations, while the lateral growth rates were 10 – 15 μm/h and 5 – 10 μm/h for [100] and [110] orientations respectively. There were no detectable changes in the growth rates after the equilibrium morphology of the single crystal growth was achieved. Orientation control of the enhanced growth regions was confirmed with EBSD.

There are a few drawbacks to this technique for inducing orientation grain growth control into a polycrystalline matrix. The first issue, indicated from Figure 4-7, is inhomogeneous nucleation at the template surface. This non-uniformity of texture development can alter the final distribution of oriented grains when the templates are removed. Also, the maximum ratio of vertical to lateral growth rates was 2:1 using the approach and conditions studied here. Thus, it would not be possible to produce high aspect ratio single crystal grains. Furthermore, this process can be scaled down to smaller template sizes; however, there is a lower limit on template sizes. Since this process is driven inversely by the starting matrix grain size, template sizes of a few microns would not be successful. In order to attempt this process using micron to sub-micron template sizes, a different approach for fabricating the starting matrix material is needed.

4.5 References

1. Wada, S., K. Takeda, T. Muraishi, H. Kakemoto, T. Tsurumi, and T. Kimura, "Preparation of [110] Grain Oriented Barium Titanate Ceramics by Templated Grain Growth Method and Their Piezoelectric Properties," *Jap. J. Appl. Phys.*, **46**[10B]: 7039-43 (2007).
2. Lee, H.-Y., J.-S. Kim, and D.-Y. Kim, "Fabrication of BaTiO₃ Single Crystals Using Secondary Abnormal Grain Growth," *J. Euro. Ceram. Soc.*, **20**: 1595-7 (2000).

3. Remeika, J.P., "A Method for Growing Barium Titanate Single Crystals," *J. Am. Ceram. Soc.*, **76**[2]: 940-1 (1954).
4. Rehrig, P.W., G.L. Messing, and S. Trolier-McKinstry, "Templated Grain Growth of Barium Titanate Single Crystals," *J. Am. Ceram. Soc.*, **83**[11]: 2654-60 (2000).
5. Yamamoto, T. and T. Sakuma, "Fabrication of Barium Titanate Single Crystals by Solid-State Grain Growth," *J. Am. Ceram. Soc.*, **77**[4]: 1107-1109 (1994).
6. Yoo, Y.S., M.K. Kang, J.H. Han, H. Kim, and D.Y. Kim, "Fabrication of BaTiO₃ Single Crystals by Using Exaggerated Grain Growth Method," *J. Euro. Ceram. Soc.*, **17**[14]: 1725-7 (1997).
7. Yoo, H.-I. and C.-E. Lee, "Two-Fold Diffusion Kinetics of Oxygen Re-Equilibration in Donor-Doped BaTiO₃," *J. Am. Ceram. Soc.*, **88**[3]: 617-23 (2005).
8. Park, M.-B., C.-D. Kim, and N.-H. Cho, "Determination of Diffusion Coefficients and Grain Boundary Potential Barrier Heights of Semiconducting BaTiO₃ Ceramics," *Mater. Sci. Eng.*, **B99**: 15-19 (2003).
9. Messing, G.L., S. Trolier-McKinstry, E.M. Sabolsky, C. Duran, S. Kwon, B. Brahmaroutu, P. Park, H. Yilmaz, P.W. Rehrig, K.B. Eitel, E. Suvaci, M. Seabaugh, and K.S. Oh, "Templated Grain Growth of Textured Piezoelectric Ceramics," *Critical Reviews in Solid State and Materials Sciences*, **29**: 45-96 (2004).
10. Saldana, J.M., B. Mullier, and G.A. Schneider, "Preparation of BaTiO₃ Single Crystals Using the Modified SiO₂-Exaggerated Grain Growth Method," *J. Euro. Ceram. Soc.*, **22**[5]: 681-8 (2002).
11. Choi, S.-Y., S.-J.L. Kang, S.-Y. Chung, T. Yamamoto, and Y. Ikuhara, "Change in Cation Nonstoichiometry at Interfaces During Crystal Growth in Polycrystalline BaTiO₃," *Appl. Phys. Lett.*, **88**[1]: 011909 (3 pages) (2006).

Chapter 5

Fabrication of a 2-2 Ultrasound Transducer Array by Metal – Mediated Single Crystal Growth in BaTiO₃

5.1 Background

There are numerous applications for ceramic composites where precise control of the dimensions and spacings of elements is required. Among these are piezoelectric transducer arrays,^{1,2} thermoelectric module devices,^{3,4} and photonic bandgap crystals⁵.

High frequency ultrasound transducer arrays of high aspect ratios are of interest in medical applications for high resolution imaging. The resolution of transducer arrays depends on the element thickness and the kerf (spacing) between the elements. It is difficult to fabricate transducer arrays for frequencies $\geq 30\text{MHz}$,⁶ since dicing ceramics or crystals with diamond saws typically produce kerfs in excess of $30\ \mu\text{m}$ (too large to enable spacing of the elements at half the acoustic wavelength). Spacing the piezoelectric elements at half of the acoustic wavelength is needed to avoid reduction in image quality from grating lobes and maintaining the largest beam steering possible. The grating lobes are related to the wavelength and pitch of the composite by the following equation:⁷

$$\sin \phi = \sin \theta + \lambda/p \quad (1)$$

where ϕ is the angle of the grating lobe, θ is the angle of the main beam, λ is the wavelength, and p is the pitch (the center to center distance between the adjacent elements). The pitch is equal to the sum of the width of the ceramic element and the kerf. Thus with increasing frequency (lower λ) the kerf must be reduced in order to avoid degrading the image quality.⁷ For a transducer array that operates at 50 MHz, acoustic beam steering and focusing requires ceramic elements less than $10\ \mu\text{m}$ wide, $30\ \mu\text{m}$ high, and with a kerf below $5\ \mu\text{m}$.⁸ The kerf is then back-filled with a polymer to make 2-2 or 1-3 composites. With this set of requirements for the ceramic / polymer composites,

available processing techniques for fabricating transducers are evaluated and the current limitations discussed. A review of methods of composite fabrication is given elsewhere.⁹

Ultrasonic transducers have been fabricated by several methods: a) dice-and-fill techniques in which bulk ceramics or single crystals are cut into individual elements, backfilled with a polymer, then lapped and thinned to the desired thickness, b) approaches in which lithographic patterning is combined with dry etching of bulk ceramics or single crystals to produce the required ceramic size and kerf and c) methods employing a fugitive or passive phase to prepare 2-2 composite structures by laminating in alternating layers.

Cannata et al.¹⁰ fabricated a 64 element 2-2 composite transducer array by the dice-and-fill process. For this method, a polycrystalline PZT ceramic was mechanically cut into the 64 elements with a pitch of 25 μm . The sample was backfilled with an epoxy containing 17 vol% alumina particles. The composite was then lapped to a final thickness of 50 μm . In the center section of the sample, the final kerf was 14 μm . The average center frequency of the fabricated transducer was 34 MHz. Michau et al.¹¹ fabricated a 128 element array 1-3 composite transducer by the dice-and-fill process with a center frequency of 27.3 MHz. After dicing, backfilling with epoxy, and lapping, the final thickness of the transducer was 47 μm with a pitch of 100 μm and a kerf width of 12 μm .

It can be seen from both the Cannata et al. and Michau et al. reports that fabrication of a kerf less than 5 μm by the conventional process of dice-and-fill is extremely difficult. The major limitations of current dice-and-fill technology are the final composite pitch and kerf, thus limiting the maximum frequency of the final transducers (Equation 1).

Lukacs et al.¹² produced a linear 64 element transducer array from a $\text{Pb}(\text{Zr},\text{Ti})\text{O}_3$ (PZT) bar by laser machining. The 64 element array consisted of a 74 μm pitch with a kerf of 8 μm . Each of the elements had a matching layer and was attached to an aluminum backing layer. The average center frequency of the fabricated transducer was 28.1 MHz. As shown by the authors, the kerf is significantly lower than can be achieved using a diamond saw for the dice-and-fill technique. However, additional complications

arise from the need to machine at a lower power to avoid degradation of the ceramic, thus increasing the machining time.⁸

Similar to the dice-and-fill technique is the Interdigital phase bonding (IPhB) method. Yin et al.⁶ used this method to fabricate a 20 – 40 MHz transducer that has a smaller pitch and kerf than can be obtained via a standard dice-and-fill process. The IPhB method involves taking two individually diced ceramic sheets and interweaving the ceramic “teeth”. While holding them in place, the voids are backfilled with epoxy. The top and bottom sections of the ceramic plates are lapped away, exposing a 2-2 composite structure where the pitch is on the order of the saw blade thickness. Alternately, if only one side of the ceramic plates is lapped away, the IPhB process can be repeated to produce a fine 2-2 composite structure. The final dimensions of the transducer consisted of 19 μm wide ceramic layers, a 24 μm pitch, and a kerf of 4 μm . Initial reports of this technique showed that there were difficulties in correctly maintaining the alignment and spacing of each of the piezoelectric elements.

Jiang, et al.¹³ utilized a combination of photolithography and dry etching to produce 1-3 composites with single crystal $\text{Pb}(\text{Mg}_{1/3}\text{Nb}_{2/3})\text{O}_3\text{-PbTiO}_3$ (PMN-PT). The process involved using a nickel mask electrodeposited on the surface of the polished PMN-PT single crystal in the pattern of the required size and distribution of the ceramic pillars. Reactive ion etching the exposed single crystal produced a pillar height of 60 μm . This was then backfilled with epoxy. The final 1-3 transducer design consisted of pillars with a high aspect ratio (height to width of four). The top portion of the 1-3 composite consisted of a 2 μm kerf, but the bottom portion of the composite had gaps of 5.2 μm , given the sidewall angle of 87° . Although this is better than the $<80^\circ$ sidewall angles that have been previously reported,^{14, 15} the tapering of the sidewall becomes a problem for higher aspect ratio transducers for higher frequency composites.¹⁵ As shown by Equation 1, with a reduction in wavelength, the pitch of the elements must decrease to avoid grating lobes. If the thickness of the sample is reduced (to increase frequency) the ceramic elements must be reduced in size and have a higher aspect ratio to maintain the half the acoustic wavelength rule to avoid the grating lobes’ influence.²

Another processing technique to produce 2-2 composite transducers involves laminating the piezoelectric ceramic with passive or filler layers to form a 2-2 connectivity structure. The patent by Zola^{16 1985, 1985} was first to describe the lamination of discrete piezoceramic plates and a passive material to form 2-2 composite structures. Stevenson et al.¹⁷ produced a 2-2 transducer composite via a similar approach using tape cast PZT ceramics and heat-laminated thermoplastic films. Ritter et al.¹⁸ fabricated a 30 MHz 2-2 composite transducer by lapping polycrystalline PZT ceramics to 28 μm and then bonding the ceramic layers with an epoxy loaded with 5.5 μm polystyrene spheres. The overall structure was then lapped to 150 μm . The final 48 element array consisted of a pitch of 33 μm , a final kerf of 5 μm and an average center frequency of 30.6 MHz.

Hackenberger et al.¹⁹ constructed a 2-2 composite transducer using a fugitive carbon phase to produce the final passive layer thickness. Green PZT ceramic powder was dispersed in a polymer matrix and tape cast to a thickness ranging from 25 – 50 μm . These layers were then stacked with alternating layers of carbon. The compact was then heated to remove the organics and the carbon layer. When the carbon layer was removed, the kerf space was defined. Hackenberger et al. produced two different 2-2 composite structures, one with a 38 μm ceramic thickness and a 7 μm kerf and a second with a 22 μm ceramic thickness and a 4.5 μm kerf. The 38 μm ceramic element transducer produced an average center frequency of 21 MHz.

Button et al. constructed piezoelectric transducers, both ceramic and composite structured, by viscous polymer processing.²⁰ The fabrication process entailed creating a ceramic paste with high molecular weight binders for increased strength during green state handling. Thin PZT ceramic disks of 50 – 100 μm thickness with a diameter around 5 mm have been produced with a center frequency around 50 MHz. 1-3 piezoelectric / polymer composites have been fabricated with PZT and lithium niobate with element diameters around 100 μm . The thicknesses were 100 μm and 77 μm , respectively, which produced a center frequency around 20 MHz and 50 MHz, respectively.

A summary of the current processing techniques and the resolution limits is given in Table 5-1. Most of the processing techniques to produce small ceramic layers and a low kerf, such as tape casting are limited to producing polycrystalline ceramic layers,

rather than single crystal transducers. The dice-and-fill and reactive ion etching techniques have been applied to bulk single crystals to form the transducers but the smaller scale of kerf is limited. As stated earlier, the transducers produced by mechanical dicing are limited as a result of the inability to produce a kerf less than 12 μm . The uniformity of etching during the patterning and ion etching process is limited as a result of the inability to produce a constant kerf from the top to the bottom of the ceramic pillars.

Table 5-1: Processing techniques and current resolution limits for composite transducers.

Method [ref]	Pitch (μm)	Ceramic Width (μm)	Kerf width (μm)
IPhB ⁶	25	15	4
Tape Lamination ¹⁸	33	28	5
Laser Cutting ²¹	33	25	8
VPP ²⁰	120	100	20
Dice and Fill ¹⁰	25	11	14

5.2 Introduction

From Chapter 4, the conditions for single crystal growth in a patterned array with limited matrix coarsening were developed. By firing at 1300°C in 1×10^{-5} atm PO_2 , the crystal boundary was shown to produce a 2:1 height to width aspect ratio crystal in the BaTiO_3 matrix. Extensive lateral growth resulted in crystal merging during long growth runs thus losing control over the crystal pattern. To limit lateral growth and produce single crystal structures with a higher aspect ratio, a new approach has been developed to mediate lateral single crystal growth in the matrix.

Below, a novel processing method is reported to produce 2-2 single crystal (or polycrystalline ceramic) / polymer composite for transducer applications. The process involves using metal layers to mediate single crystal growth into a 2-2 composite with a designed crystallographic orientation. The metal layers are then removed (for example,

using an acid etch) and the final 2-2 composite structure has single crystal (or polycrystalline ceramic) layer widths ranging from 3 μm to 70 μm . After backfilling with epoxy, a kerf ranging from 1.5 μm to 5 μm was produced.

5.3 Experimental Procedure

5.3.1 Matrix Fabrication

$\text{Ba}(\text{Zr}_{0.05}\text{Ti}_{0.95})\text{O}_3$ powders were prepared by ball milling a mixture of 93.2 wt% BaTiO_3 , 2.6 wt% ZrO_2 (Sigma Aldrich), and 4.2 wt% BaCO_3 (Sigma Aldrich) in ethanol for 24 h. The powder was dried overnight in a glass dish and calcined in a platinum crucible at 1100°C for 4 h in air with heating and cooling rates of 5°C/min. The calcined powder was ground and sieved through a 90 μm mesh and phase purity was checked by XRD (Figure 5-1).

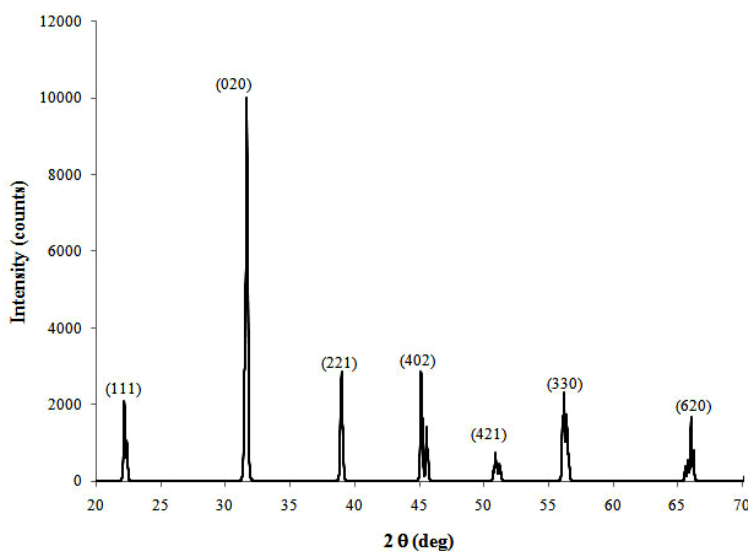


Figure 5-1: XRD scan of the $\text{Ba}(\text{Zr}_{0.05}\text{Ti}_{0.95})\text{O}_3$ powder calcined at 1100°C for 4 h in air. Indexed using an orthorhombic cell. (JCPDS Card # 00-056-1034).

For the ceramic layers in the 2-2 composites, polycrystalline BaTiO₃ or Ba(Zr_{0.05}Ti_{0.95})O₃ samples were prepared by the non-aqueous tape casting approach described in Chapter 3.

The screen printing process for making the metal layers is the same as that used commercially for fabricating BaTiO₃ based multilayer ceramic capacitors (MLCC) and is illustrated in Figure 5-2. The cut green tapes were screen printed (MSP645, Affiliated Manufacturers Inc., North Branch, NJ) with a nickel based ink (Keck Smart Materials Integration Lab., Penn State University) to produce 2 mm x 4 mm rectangles on each green tape layer (the black rectangles in Figure 5-2). The ink consisted of nickel powder of 0.3 μm diameter with ethyl cellulose in a terpineol solution. The nickel ink was screen printed and dried for 3 min at 65°C. The dried thickness of the nickel ink was 7 μm. The screen printed tapes were then stacked and isostatically laminated at 75°C for 1 h with 20 MPa. The compact was then diced to separate the 25 individual pattern stacks. The compact was then diced to separate the 25 individual pattern stacks.

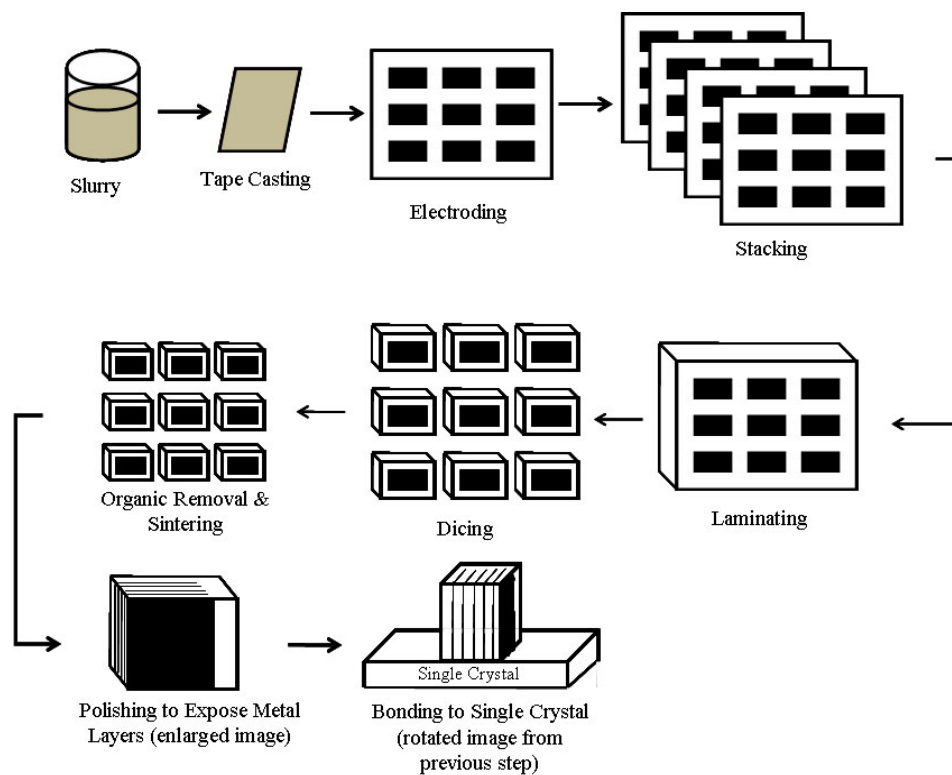


Figure 5-2: Schematic of the screen printing and composite fabrication process.

The organic removal and sintering were completed in a controlled atmosphere furnace to avoid the oxidation of the nickel. The organics were removed by heating the sample at 650°C for 70 h in a PO_2 of 1×10^{-19} atm. The samples were then isostatically pressed at 200 MPa and sintered at 1300°C for 1.25 h with a PO_2 of 1×10^{-13} atm using a combination of 100 sccm wet N_2 , 387 sccm dry N_2 and 12 sccm H_2 . The wet N_2 was bubbled through deionized water to achieve the required oxygen level.

5.3.2 Single Crystal / Polymer Composite Fabrication

The BaTiO_3 single crystals used for bonding were cut along either the $\langle 001 \rangle$ or the $\langle 110 \rangle$ orientations. The surfaces were polished with progressively finer grit sizes to a final 0.25 μm diamond suspension. A 0.25M TiO_2 sol gel layer was spin coated on the surface of the BaTiO_3 single crystals at 4000 rpm for 30 s. This layer was then heated in a furnace to 350°C to remove the solvents and obtain a 25 nm thick amorphous TiO_2 layer.

After sintering, the multilayer was polished until the nickel inner layers were exposed on three sides of the composite, followed by polishing with a 0.25 μm diamond suspension. The BaTiO_3 – Ni 2-2 composite was bonded to the BaTiO_3 single crystal by contacting the polished surface of the BaTiO_3 single crystal and loading with 50 g to maintain contact. This ensemble was then placed in the furnace and heated to 1250°C at a PO_2 of 1×10^{-11} atm for times up to 70 h to induce single crystal conversion through the BaTiO_3 layers (shown schematically in Figure 5-3).

In addition to the above samples, commercially available MLCCs (Kemet, Greenville, SC) were used. The nickel inner layers were exposed on one side (perpendicular to the metal layers) of the MLCCs by grinding and polishing with a diamond grit size of 0.25 μm . The MLCCs were then bonded to the BaTiO_3 single crystals using the same method outlined above. The ensemble was heated for times up to 40 h.

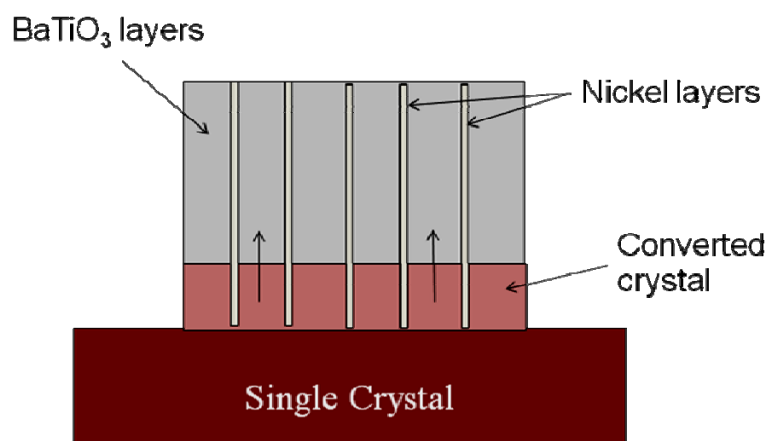


Figure 5-3: Schematic of single crystal conversion into BaTiO₃ / nickel 2-2 composite.

The ceramic / epoxy composites were fabricated by etching away the nickel metal layer in a 10:1 diluted HNO₃ solution. HNO₃ was chosen based on the results of Kim et al.,²² who studied the dissolution of nickel from MLCC BaTiO₃ capacitors as a function of different acid solutions, temperature, concentration, and nickel layer thickness. They showed the highest Ni etch rates for HNO₃ at 90°C with constant agitation. The activation energy of the nickel leaching was determined to be 37.6 kJ/mol and the main rate-determining factor was the nickel layer thickness and the path depth of the nickel through the BaTiO₃ layers. However, no analysis was done on the etching effects on BaTiO₃.²²

The etching process was modified by first polishing the samples to expose the metal on 3 of the 4 sides for adequate exposure and removal of the nickel. The samples were then placed in the nitric acid solution and constantly agitated for 5 minutes, and then cleaned using deionized water. This process was repeated for up to 4 h depending on the total width of the ceramic / nickel composites. Leaving the composites to etch longer than the 5 minute intervals would cause excessive etching of the BaTiO₃ layers, as shown in Figure 5-4a. Figure 5-4b is an optical cross section of a backfilled ceramic / epoxy composite sample after etching for 4 h without the intermittent deionized water washing

procedure. The surface pitting is due to polishing, and not from the etching procedure. As the local concentration of nickel in the HNO_3 solution (between the BaTiO_3 layers) increased, the nickel etching rate would decrease. In response, longer exposures to the etching solution were required to enable complete Ni removal. By periodically interrupting the etching to completely rinse the parts, the nickel etch rate could be increased by avoiding locally high Ni concentrations in the solution. As a result, the intermittent washing step significantly limited the etching of the BaTiO_3 (since shorter total acid exposure times were enabled), and the nickel was completely removed in between the BaTiO_3 layers.

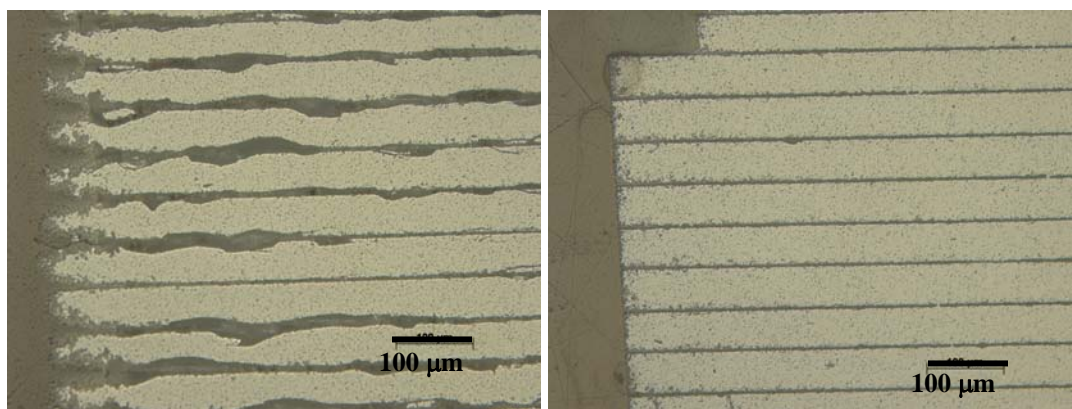


Figure 5-4: Optical micrographs of the cross section of the etched and backfilled ceramic / epoxy composites etched using HNO_3 for a) a continuous 4 h etch and b) removal and washing after 5 minute etch intervals.

Another issue associated with the etching of the nickel is the barium leaching from the surface of the BaTiO_3 compacts. Anderson et al. showed that there is significant barium leaching from the surface of BaTiO_3 in water, particularly at low pH.²³ Thus, it is likely that the BaTiO_3 surface chemistry is significantly altered by the repeated etching process. The surface Ba/Ti ratio will be different, and point defects, such as barium and the compensating oxygen vacancies could be present. Erhart and Karsten modeled the electrical conductivity of BaTiO_3 as a function of defect concentration. They showed that with an increase in both barium and oxygen vacancies, the electrical conductivity increases.²⁴ During the HNO_3 acid etching procedure, any additional point defects induced at the interface could produce conduction pathways through the final ceramic /

epoxy composites, thus affecting the ability to pole the sample, and hence the final dielectric and piezoelectric properties.

Polotai et al. also showed that when co-firing BaTiO₃ with nickel in heavily reducing atmospheres, an inter-metallic alloy is formed. This phase develops when the barium in BaTiO₃ is reduced to metallic Ba, and thus forms an intermediate (Ba,Ti,Ni) metal alloy.²⁵ Again, this could lead to a change in the BaTiO₃ surface chemistry. It is recommended that in future work, an alternative Ni removal scheme should be developed to minimize these problems.

5.3.3 Dielectric and Piezoelectric Property Measurements

The samples' top and bottom surfaces were polished using progressively finer grit sizes with a final polish with 0.25 μm diamond suspension. 100 nm of gold was sputtered (Bal-Tec SCD 050 Sputter Coater) for 90 s onto the polished surfaces. The edges were ground with 1800 grit SiC paper to prevent any shorting between the top and bottom electrodes (Figure 5-5).

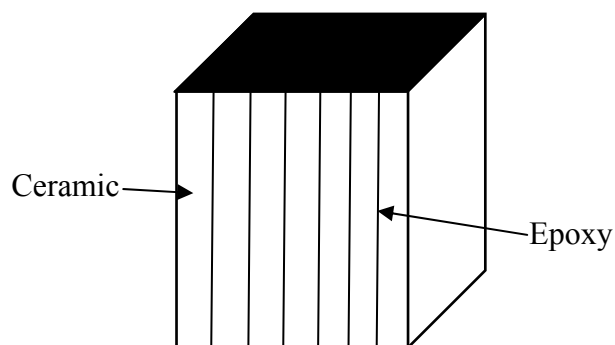


Figure 5-5: Schematic showing the ceramic and epoxy layers of the composite with respect to the gold electrodes (colored black).

A multifrequency meter (HP 4284A LCR meter) was used in conjunction with a computer controlled temperature chamber (Model MK 9023, Delta Design Inc., Poway,

CA) to measure the relative permittivity and loss from 100 Hz to 1 MHz from 25°C to 140°C.

The samples were poled at 75°C at 2.5 times the coercive field for 20 min and field cooled to room temperature. The high field measurements (1 – 50 kV/cm) on the samples include the polarization vs. field, unipolar strain vs. electric field, and bipolar strain vs. electric field. These were obtained using a computer controlled modified Sawyer – Tower system and a linear variable displacement transducer (LVDT) sensor driven by a lock in amplifier (Model SR830, Stanford Research Systems, Sunnyvale, CA). The voltage was supplied by a Trek 609C-6 high voltage DC amplifier. The polarization hysteresis and bipolar strain measurements were conducted on un-poled samples. The value of the d_{33} coefficients were estimated from the slope of the unipolar strain vs. electric field curves. The d_{31} and electromechanical coupling were measured by using the IEEE resonance technique (ANSI/IEEE Std. 176-1978).

5.4 Results and Discussion

The final microstructure of the BaTiO₃/nickel starting matrix material is shown in Figure 5-6. The dielectric layers consist of an average grain size of 3 μm for both the BaTiO₃ and Ba(Zr_{0.05}Ti_{0.95})O₃ composites with 98% and 96% theoretical density, respectively. The ceramic layers are roughly 70 μm thick with the nickel on average 4 μm thick. The screen printed nickel layers are continuous and consist of a single grain across the entire thickness.

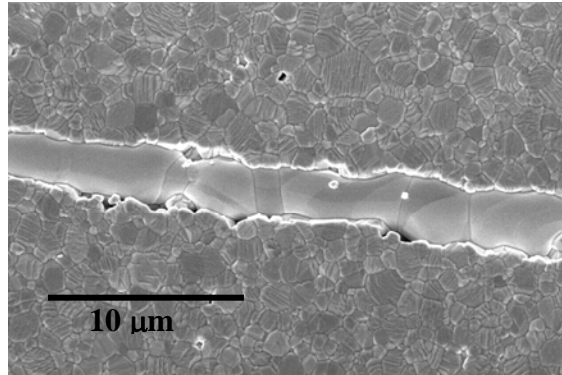


Figure 5-6: SEM image showing the nickel layer (middle) separating the polycrystalline BaTiO₃ ceramic layers fired to 1300°C in a 1×10^{-13} atm PO₂ for 1.25 h.

Initially, polycrystalline/polymer transducer composites were fabricated from both commercially available MLCCs (Kemet series A capacitor) and the previously described tape-casting/electroding route described above to test the validity of the etching and backfilling process. The commercial MLCC used in this study is shown in Figure 5-7. Figure 5-7a illustrates the polished and etched composite with the nickel layers present and Figure 5-7b shows the backfilled transducer composite after the nickel was removed by HNO₃ etching. The final transducer composite consists of an average ceramic thickness of 4 μm and an average kerf of 1.5 μm. Thus, the process of fabricating polycrystalline/polymer transducers by this method can be achieved on a finer scale than is possible using available commercial processes used to make composite piezoelectric transducers (Table 5-1). The technological approach is also economically scalable to production quantities.

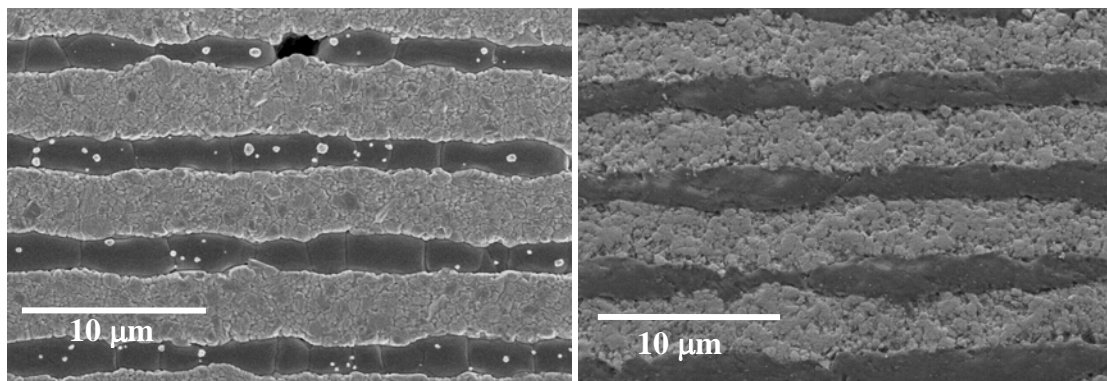


Figure 5-7: SEM images showing a) polished and etched composite with the nickel layers and b) a composite sample after removing the nickel layers and backfilling with epoxy.

Figure 5-8 shows the vertical growth distance from a bonded [001] BaTiO₃ single crystal as a function of PO₂ levels for both Ba(Zr_{0.05}Ti_{0.95})O₃ and the BaTiO₃ samples (from Figure 4-5) fired to 1300°C for a 2 h dwell. When the samples are fired in air, the BaTiO₃ growth rate was ~100 μm/h, while the Ba(Zr_{0.05}Ti_{0.95})O₃ single crystal growth rate was slower at ~70 μm/h. The growth rate is faster than what has been previously reported,²⁶ where an average growth rate of 28 μm/h was achieved after a 30 h dwell at 1350°C. The main reason for the difference in growth rate could be the large amount of porosity in the ceramic in Rehrig's work. In Figure 5-8, it is seen that at lower oxygen levels the growth rates for both materials are similar; the growth rate drops to zero for PO₂ below 1x10⁻¹³ atm. The drop in growth is probably related to the observation by Kang et al.²⁷ that there is no abnormal grain growth below this PO₂ level. In this work, a PO₂ of 1x10⁻¹¹ atm was chosen for subsequent growth studies in order to prevent the oxidation of the nickel inner layers while enabling finite growth rates.

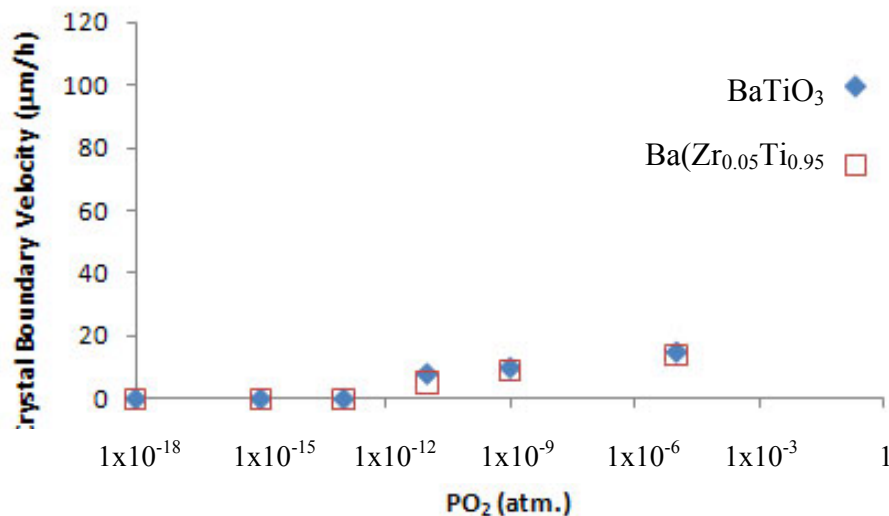


Figure 5-8: Graph of grain boundary velocity using a [001] BaTiO₃ single crystal as a function of atmosphere for BaTiO₃ and Ba(Zr_{0.05}Ti_{0.95})O₃ samples fired at 1300°C for 2 h.

Commercial MLCC's were first used to test the idea of mediating lateral growth during solid state crystal conversion. Figure 5-9 shows the extent of growth of a <001> single crystal boundary in a commercial MLCC (Kemet series M capacitor). The sample was heated to 1300°C in PO₂ of 1x10⁻¹¹ atm for up to 40 h. The maximum single crystal growth was 30 µm (Figure 5-10). This limit was due to a combination of the coarsening of the remaining matrix grains (~20 µm) and the grain growth - inhibiting dopants used in the commercial MLCC. However, this sample illustrates that the single crystal boundary can be regulated by the nickel layers, and thus discrete single crystal elements could be fabricated. It also demonstrates the very fine kerfs that can be achieved.

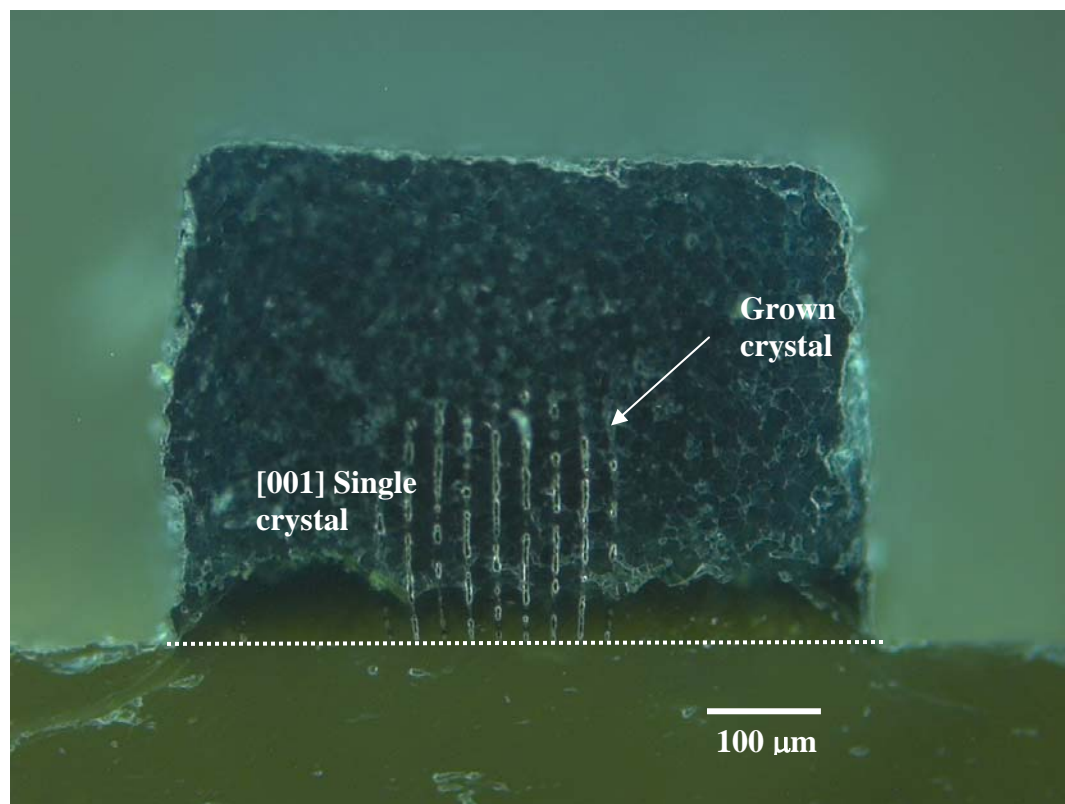


Figure 5-9: Optical image of the growth of a [001] single crystal boundary through the commercial MLCC at 1300°C in PO_2 of 1×10^{-11} atm for 40 h. The dotted line indicates the original boundary between the single crystal and the capacitor.

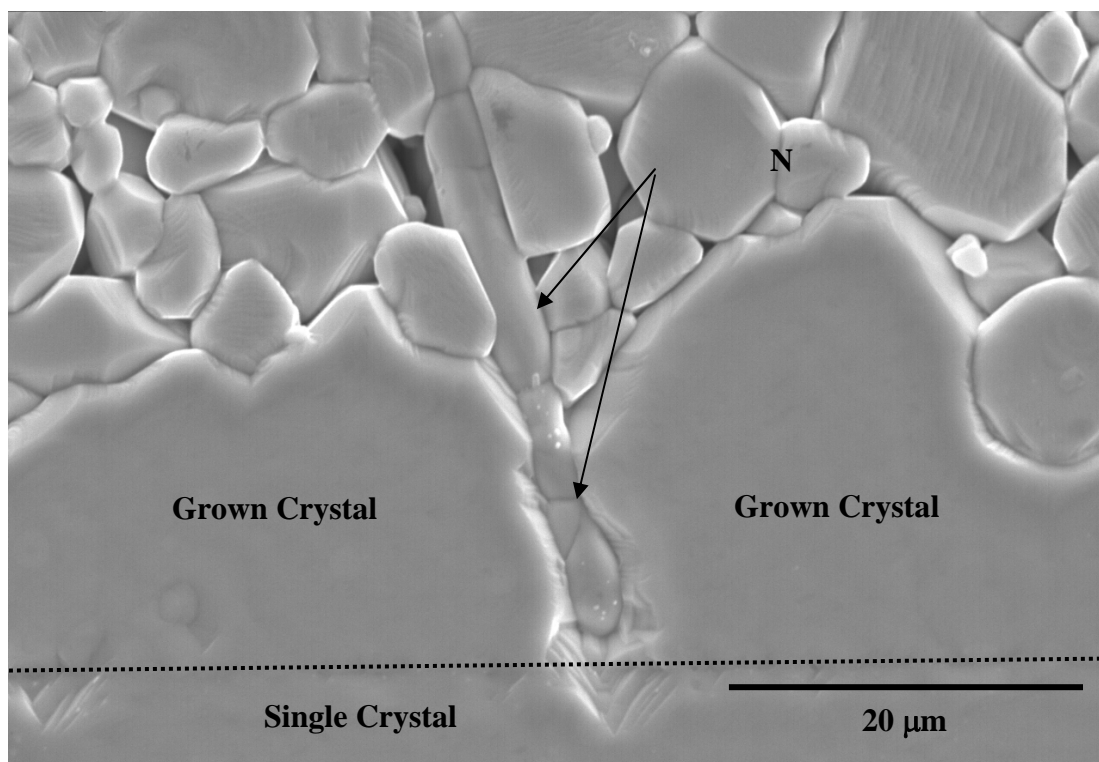


Figure 5-10: SEM image of the grown crystal with the lateral growth mediated by the nickel layers in the MLCC at 1300°C in PO_2 of 1×10^{-11} atm for 40 h. The dotted line indicates the original boundary between the single crystal and the MLCC.

To obtain greater single crystal boundary growth distances, BaTiO_3 / nickel composites were fabricated without any grain growth - inhibiting dopants. Figure 5-11 shows an optical image of a [001] BaTiO_3 single crystal bonded to the 2-2 composite and grown at 1300°C in PO_2 of 1×10^{-11} atm for 80 h. The grown crystal is $\sim 400 \mu\text{m}$ high and roughly 1 mm deep (i.e. into the plane of the picture). As shown in Figure 5-11, the nickel layers are still present but have not limited the lateral growth of the converted single crystal layers, thus the equilibrium single crystal boundary appears not to be regulated by the nickel layers.

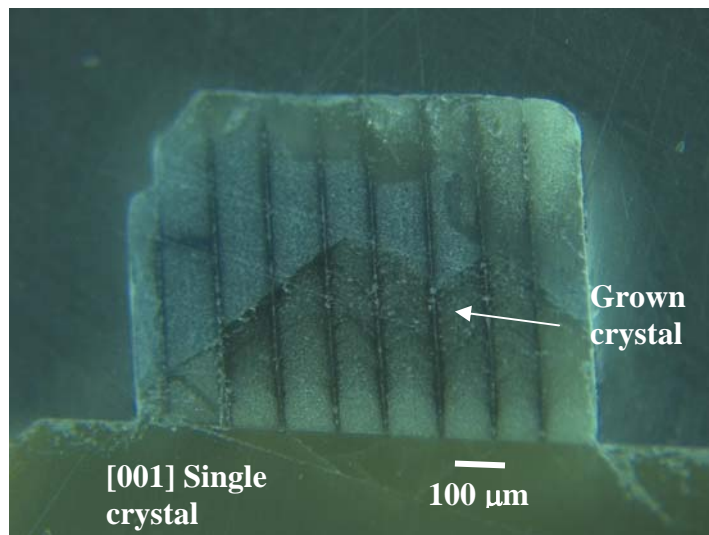


Figure 5-11: Optical image of a [001] BaTiO₃ single crystal bonded to the 2-2 composite matrix at 1300°C in PO₂ of 1x10⁻¹¹ atm for up to 80 h.

Figure 5-12a shows an optical micrograph of the polished BaTiO₃ sample after 70 h dwell at 1300°C in 1x10⁻¹¹ atm PO₂. The nickel layers show a large amount of discontinuity, which is the primary reason the equilibrium single crystal morphology was not limited within the nickel layers since the continuity of the nickel layers is important to mediating the lateral single crystal growth. The metal continuity was previously studied for BaTiO₃ / nickel multilayers and is in good agreement with the results for heating at high temperatures for a prolonged time.²⁵ The continuity of the nickel layer was studied as a function of temperature and time. It was learned that the nickel becomes discontinuous between 60 and 70 h at 1300°C (Figure 5-12a), while the nickel remained continuous at 1250°C and 1200°C more than 100 h (Figure 5-12b); all runs were completed in a PO₂ of 1x10⁻¹¹ atm. However, no bonding and thus single crystal growth was achieved for samples heated at 1200°C in a PO₂ of 1x10⁻¹¹ atm. Thus, for subsequent single crystal growth studies, 1250°C was chosen to ensure bonding and continuity of the nickel mediating layers. The single crystal growth rates were then re-measured for the 1250°C and 1x10⁻¹¹ atm PO₂ for each crystal orientation and are given in Table 5-2. The growth rate at 1300°C is given in parentheses as a reference.

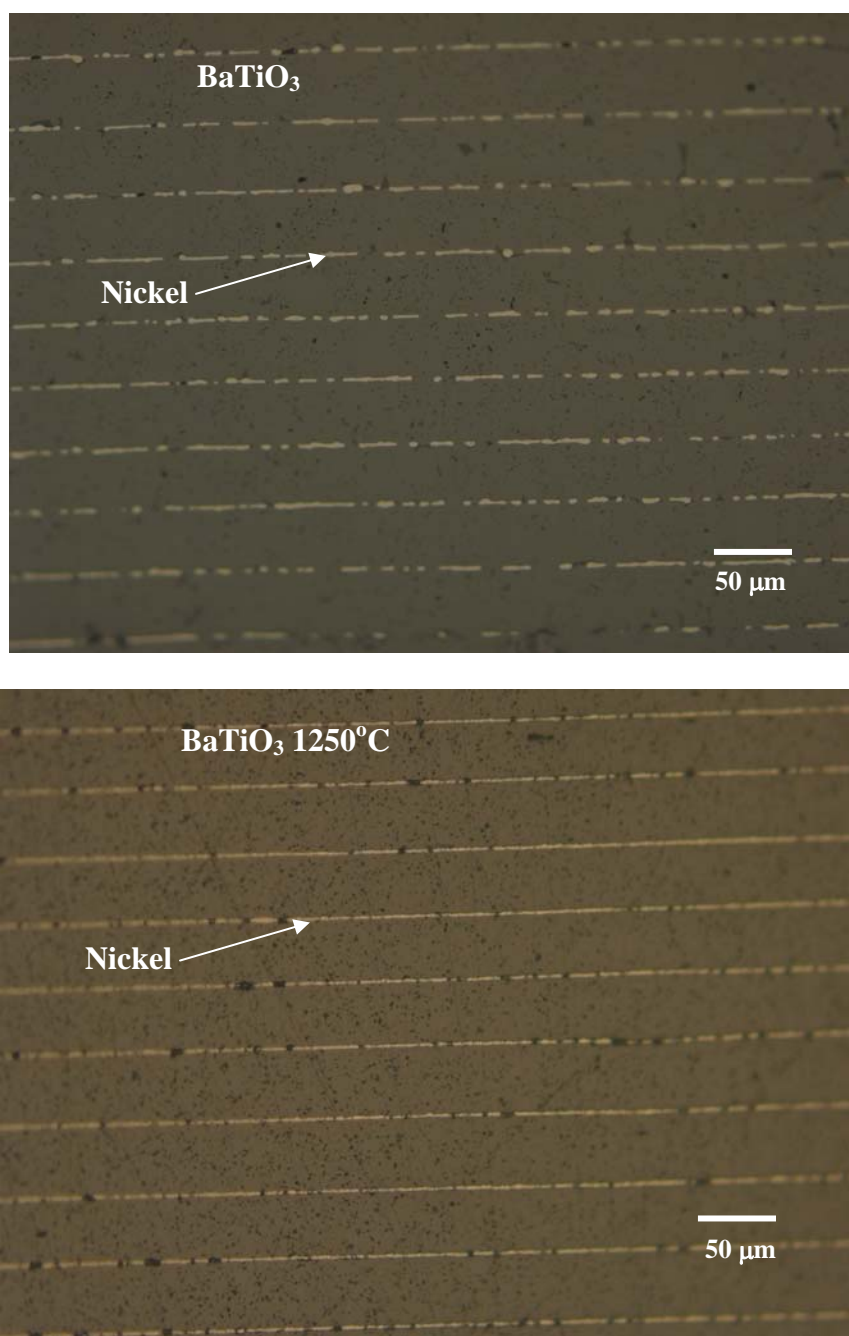


Figure 5-12: a) Optical micrograph of a BaTiO₃ sample fired at 1300°C for 70 h in a 1×10^{-11} atm PO₂ showing the nickel discontinuity along the metal layer, and b) Optical micrograph of a BaTiO₃ sample heated at 1250°C for 100 h in a 1×10^{-11} atm PO₂ showing nickel continuity.

Table 5-2: Single crystal growth rates at 1250°C and 1300°C (in parenthesis) at a PO_2 of 1×10^{-11} atm for BaTiO_3 and $\text{Ba}(\text{Zr}_{0.05}\text{Ti}_{0.95})\text{O}_3$ samples bonded to [001] and [110] BaTiO_3 single crystals.

Material	[001] ($\mu\text{m/h}$)	[110] ($\mu\text{m/h}$)
BaTiO_3	3.5 (4.5)	3 (5)
$\text{Ba}(\text{Zr}_{0.05}\text{Ti}_{0.95})\text{O}_3$	4 (5)	3.5 (4.5)

Figure 5-13 shows a BaTiO_3 composite sample bonded to a [001] BaTiO_3 single crystal fired at 1250°C for 30 h in a 1×10^{-11} atm PO_2 . The circled region in the image shows the single crystal growth into the 2-2 composite. The equilibrium morphology of the pyramidal shape has been achieved, and has been limited by the nickel layers. Figure 5-14 shows the same sample held for an additional 15 h at 1250°C in a 1×10^{-11} atm PO_2 . With the additional growth, the single crystal morphology is the same, and the growth rate was calculated to be between 3 – 4 $\mu\text{m/h}$. There is no change in the single crystal boundary growth rate after the equilibrium morphology has been achieved even when the grown crystal is limited by the nickel layers. The constant growth rate is similar to observations reported in the previous chapter for the patterned single crystals (Figure 4-10).

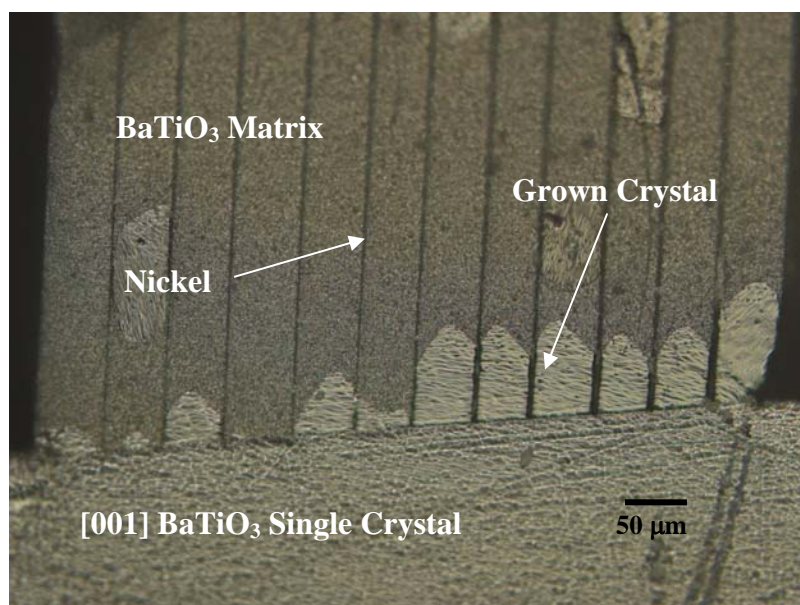


Figure 5-13: A BaTiO₃ composite sample bonded to a [001] BaTiO₃ single crystal fired at 1250°C for 30 h in a 1x10⁻¹¹ atm PO₂.

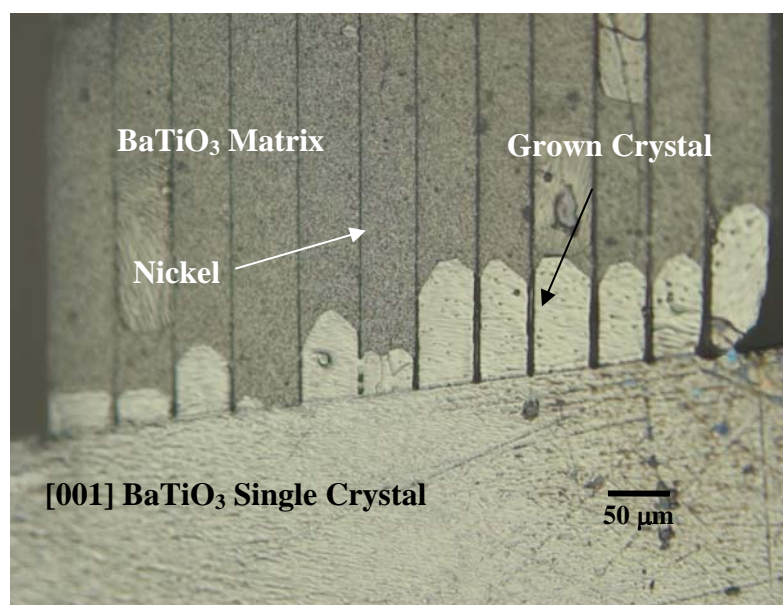


Figure 5-14: A BaTiO₃ composite sample bonded to a [001] BaTiO₃ single crystal fired at 1250°C for a total of 45 h in a 1x10⁻¹¹ atm PO₂.

Figure 5-15 shows an optical micrograph of a $\text{Ba}(\text{Zr}_{0.05}\text{Ti}_{0.95})\text{O}_3$ / nickel composite that has been heated to 1250°C for 100 h in a PO_2 of 1×10^{-11} atm. The single crystal has grown $\sim 350 \mu\text{m}$ from a [001] BaTiO_3 single crystal. This corresponds to a 8:1 height to width ratio, which is significantly improved over the patterned solid state crystal growth outlined in Chapter 4. Figure 5-16 shows the final single crystal / epoxy composite after backfilling the same sample shown in Figure 5-15.

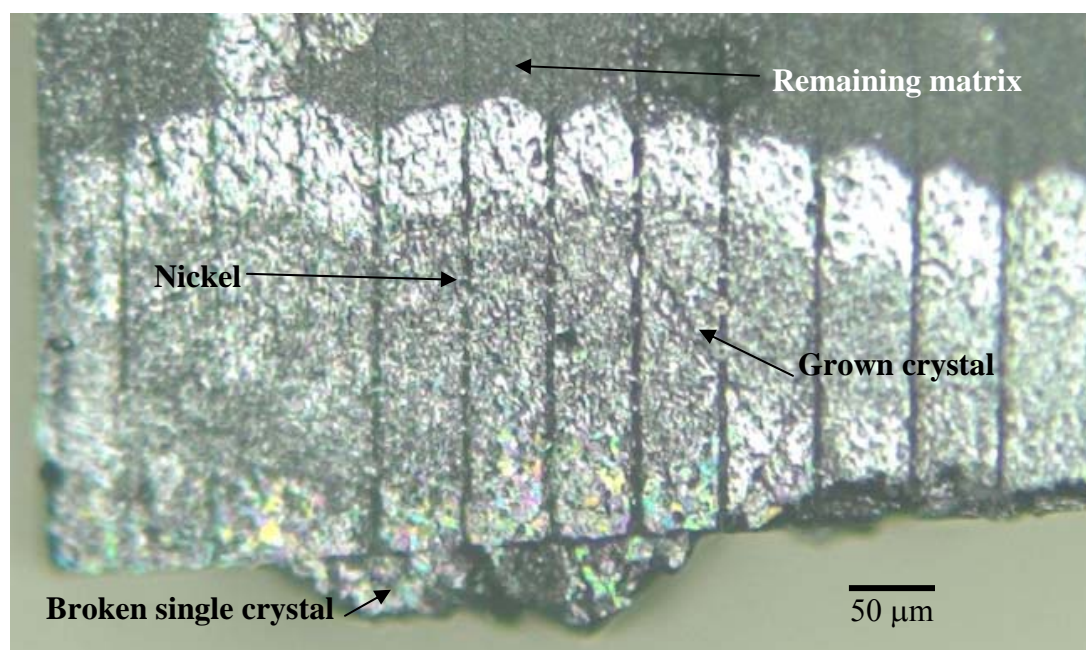


Figure 5-15: An optical micrograph of a $\text{Ba}(\text{Zr}_{0.05}\text{Ti}_{0.95})\text{O}_3$ / nickel composite that has been heated to 1250°C for 100 h in a PO_2 of 1×10^{-11} atm.

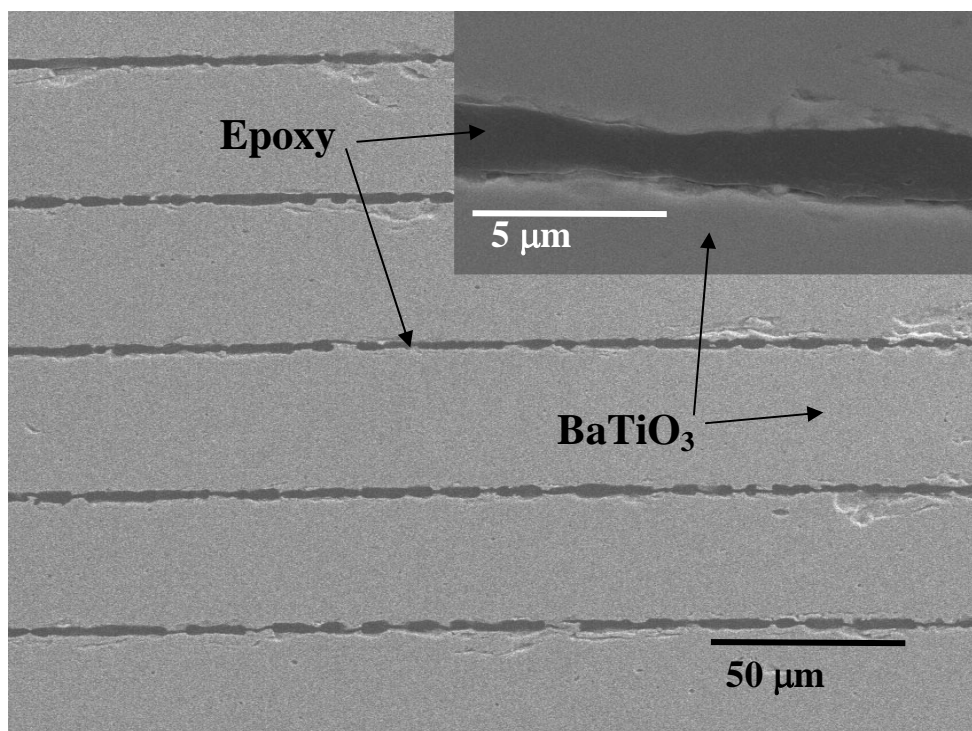


Figure 5-16: An optical micrograph of a $\text{Ba}(\text{Zr}_{0.05}\text{Ti}_{0.95})\text{O}_3$ / epoxy composite, with an inset SEM image showing the single crystal / epoxy boundary.

The ceramic / epoxy composites were fabricated by etching away the nickel layer by a 10:1 diluted HNO_3 solution. HNO_3 was chosen based on the results of Kim et al. who studied the leaching rate of nickel in MLCC BaTiO_3 capacitors as a function of different acid solutions on the leaching temperature, concentration, nickel layer thickness, etc. They showed that the highest etch rates for HNO_3 at 90°C with constant agitation. The activation energy of the nickel leaching was determined to be 37.6 kJ/mol and the main rate determining factor was the nickel layer thickness and the path depth of the nickel through the BaTiO_3 layers.²²

The etching process was modified by first polishing the samples to expose the nickel on 3 of the 4 sides for adequate exposure and removal of the nickel. The samples were then placed in the nitric acid solution and were constantly agitated (by mixing) for 5 minutes, then removed and cleaned using deionized water. This process was then repeated for up to 4 h depending on the total width of the ceramic / nickel composites. Leaving the composites to etch longer than the 5 minute interval would cause excessive

etching of the BaTiO₃ layers, as shown in Figure 5-17a. Figure 5-17b is an optical cross section of a backfilled ceramic / epoxy composite sample after etching for 4 h without the intermittent deionized washing procedure. There is significant etching of the BaTiO₃ layers as indicated by the arrows and is a result of the nickel not being successfully removed between the BaTiO₃ layers. The intermittent washing step significantly limited the etching of the BaTiO₃.

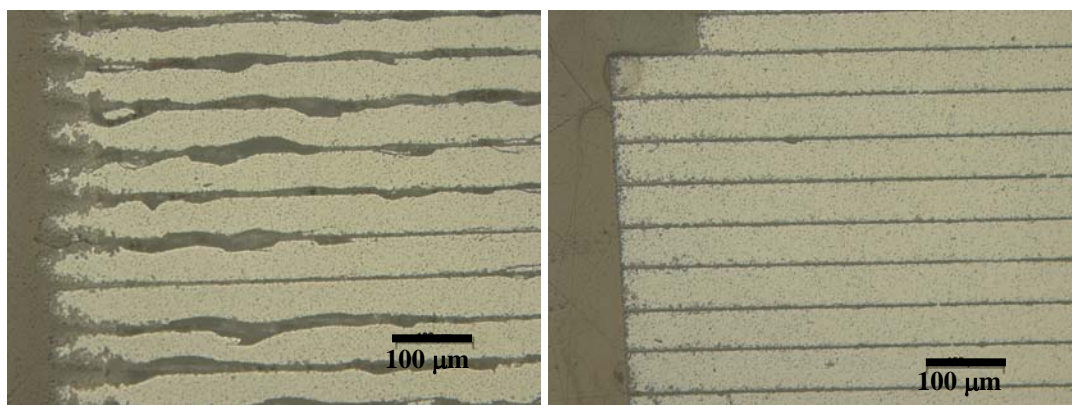


Figure 5-17: Optical micrographs of the cross section of the etched and backfilled ceramic / epoxy composites etched using HNO₃ for a) a continuous 4 h etch and b) removal and washing after 5 minute etch intervals.

Another issue associated with the etching of the nickel is the barium leaching from the surface of the BaTiO₃ compacts. Anderson et al. showed that there is significant barium leaching from the surface of BaTiO₃ when placed in acid solutions.²³ Even with the intermittent washing steps, the interface chemistry of BaTiO₃ could still be significantly altered after the repeated etching process. The surface the Ba/Ti ratio will be different, as well as point defects, such as barium and the compensating oxygen vacancies could be present. Erhart and Karsten modeled the electrical conductivity of BaTiO₃ as a function of defect concentration. They showed that with an increase in both barium and oxygen vacancies the electrical conductivity increases.²⁴ During the HNO₃ acid etching procedure, any additional point defects induced at the interface could produce conduction pathways through the final ceramic / epoxy composites, thus affecting the final dielectric and piezoelectric properties.

Polotai et al. also showed that when co-firing BaTiO₃ with nickel in heavy reducing atmospheres, an inter-metallic alloy is formed. This phase consists of reducing the barium in BaTiO₃ to metallic Ba, and thus forming an intermediate (Ba,Ti,Ni) metal alloy.²⁵ This alloy could potentially be less reactive in HNO₃, and is not fully removed during the etching process. This could also cause an effect on the final properties of the ceramic / epoxy composite.

5.4.1 Dielectric and Piezoelectric Results

The dielectric permittivity and loss were measured from 100 Hz to 100 kHz from 25°C to 140°C for both BaTiO₃ and Ba(Zr_{0.05}Ti_{0.95})O₃ ceramic and polycrystalline / epoxy composite samples. The Curie temperatures were ~128°C and ~114°C for the BaTiO₃ and Ba(Zr_{0.05}Ti_{0.95})O₃ ceramic and epoxy composites, respectively. Jaffe et al.²⁸ showed a shift of ~20°C for the 5 mol% zirconia doped BaTiO₃, which is close to the observed shift (~15°C). The slight difference could be caused by an inhomogeneous distribution of the zirconia in the final polycrystalline sample. Figures **5-18** and **5-19** show the dielectric permittivity and loss as a function of temperature for the BaTiO₃ ceramic and epoxy composite, and for the Ba(Zr_{0.05}Ti_{0.95})O₃ ceramic and epoxy composite, respectively.

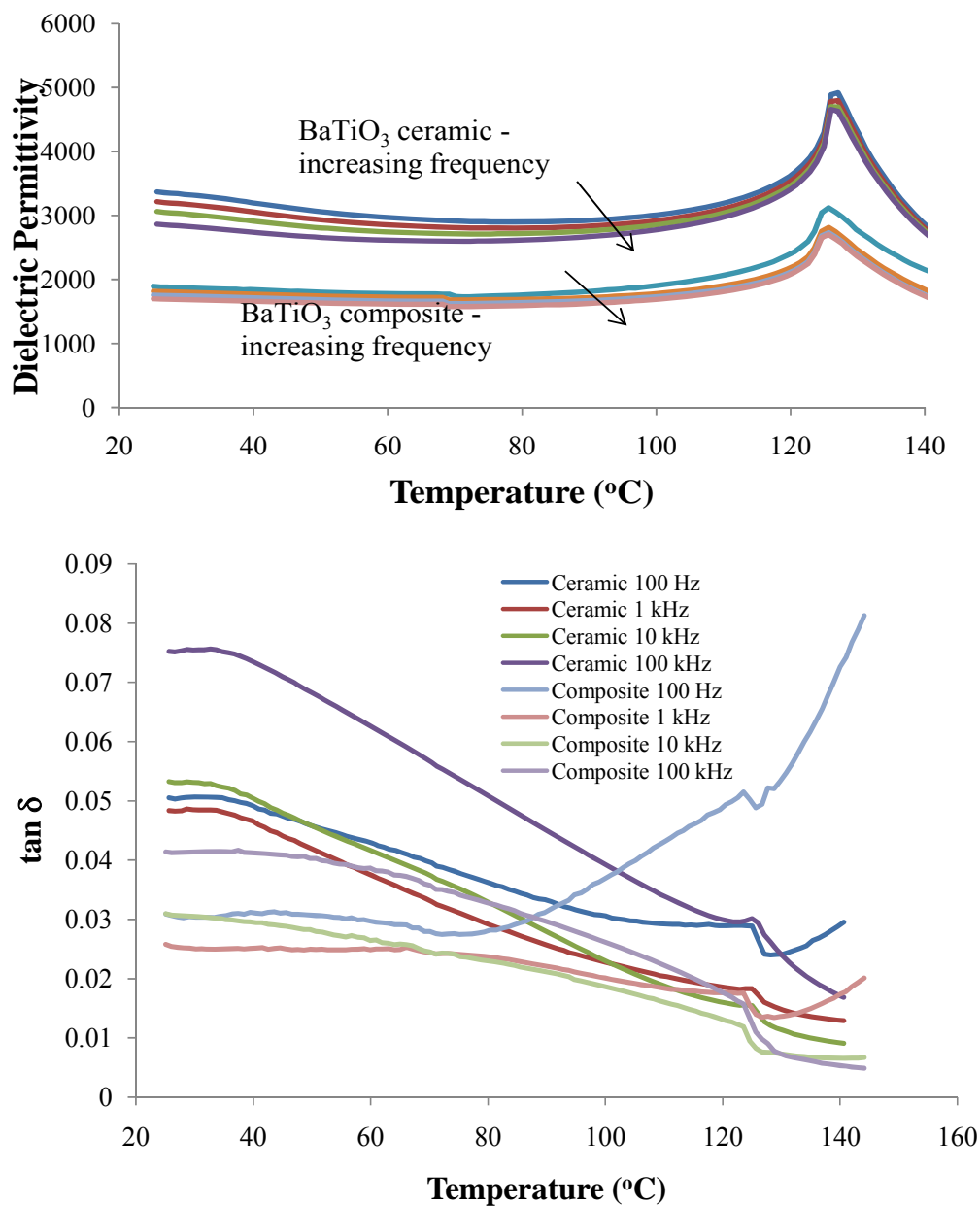


Figure 5-18: Dielectric permittivity and loss tangents as a function of temperature for BaTiO₃ ceramic and epoxy composites from 100 Hz to 100 kHz.

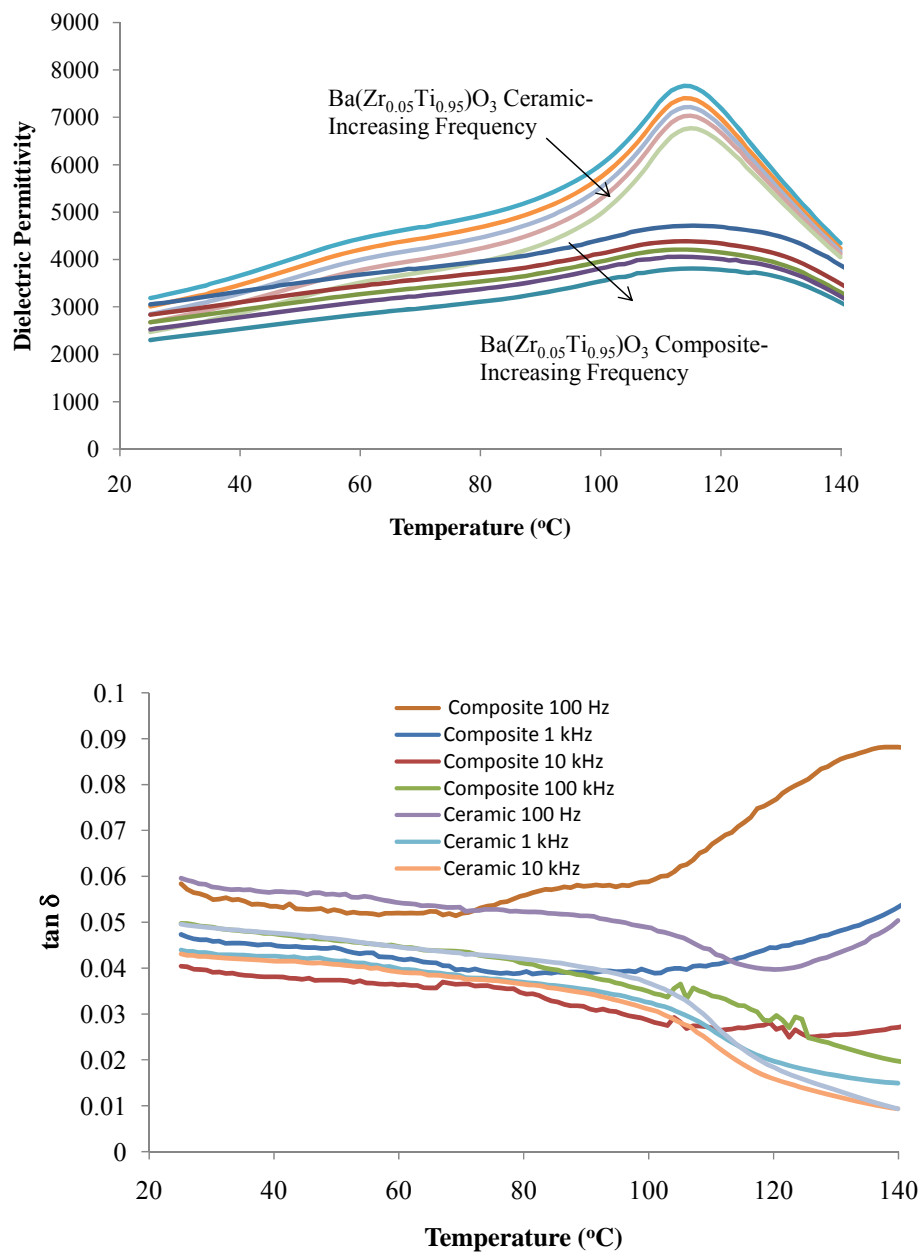


Figure 5-19: Dielectric permittivity as a function of temperature for Ba(Zr_{0.05}Ti_{0.95})O₃ ceramic and epoxy composites from 100 Hz to 100 kHz.

It was found that the BaTiO₃ ceramic and BaTiO₃ / epoxy composite samples show the same general trend, only the magnitude of the dielectric permittivity changed. There is a sharp peak at the Curie temperature where the relative permittivity increases to 4,900 and 2,600, respectively. The loss values for the BaTiO₃ and Ba(Zr_{0.05}Ti_{0.95})O₃ ceramic and epoxy composites were all under 5% at room temperature for 1 kHz. Above the Curie temperature, the dielectric loss decreased as domain walls are eliminated.^{28, 29}

The Ba(Zr_{0.05}Ti_{0.95})O₃ ceramic and Ba(Zr_{0.05}Ti_{0.95})O₃ / epoxy composites show a diffuse peak at the transition temperature, along with more dielectric dispersion, which could be caused by inhomogeneous distribution of the zirconia in the calcined powder. The dielectric peak permittivity decreases from 6,800 for the Ba(Zr_{0.05}Ti_{0.95})O₃ ceramic to 4,400 for the Ba(Zr_{0.05}Ti_{0.95})O₃ / epoxy composite. The loss for the sample set is roughly 4–6 % except for the 100 Hz data. The values for the 100 Hz rose due to conduction at low frequencies. Table 5-3 lists the dielectric permittivity and loss at 25°C and at the T_c at 1 kHz. It is notable that the low frequency loss of the composites is somewhat higher than that of the ceramic at elevated temperatures. This would be consistent with the either incomplete reoxidation of the composite samples or with the development of local nonstoichiometric regions associated with leaching during the etching step.

Table 5-3: Dielectric permittivity and loss at 1 kHz for BaTiO₃ and Ba(Zr_{0.05}Ti_{0.95})O₃ ceramic and epoxy composites.

	25°C Perm.	25°C Loss	T _c Perm.	T _c Loss
BaTiO ₃ Ceramic	3,100	0.05	4,900	0.03
BaTiO ₃ Composite	1,900	0.028	2,600	0.02
Ba(Zr _{0.05} Ti _{0.95})O ₃ Ceramic	3,200	0.045	6,800	0.045
Ba(Zr _{0.05} Ti _{0.95})O ₃ Composite	2,800	0.05	4,400	0.023

The parallel mixing rule was employed to estimate the change in dielectric permittivity that would be expected as a function of the amount of epoxy in the 2-2 polycrystalline ceramic / epoxy composites. The dielectric permittivity of the Epotek epoxy is ~ 4. Using the room temperature and Curie temperature dielectric permittivity values for the polycrystalline ceramic in Table 5-3, the composite dielectric permittivity was calculated using Equation 5-1.³⁰

$$\epsilon^* = V_{Ceramic} \epsilon_{Ceramic} + V_{Epoxy} \epsilon_{Epoxy} \quad \mathbf{5-1}$$

where ϵ^* is the dielectric permittivity of the composite, V is the volume fraction of the ceramic or epoxy, and ϵ is the dielectric permittivity of the ceramic or epoxy. The calculated and measured dielectric permittivity for the BaTiO₃ and the Ba(Zr_{0.05}Ti_{0.95})O₃ / epoxy composites at room temperature and at the Curie temperature are listed in Table 5-4. There is only 8 vol% epoxy in the composite structures, which would agree well with an ~8% drop in the dielectric permittivity. The measured values are well below the calculated dielectric permittivity of the composites. There are several possibilities for the significant drop in effective permittivity; 1) excess amount of epoxy in the composites, in particular if any appears between the ceramic layers and the electrodes, which would introduce a series component for the low permittivity phase, 2) the electrodes were not perpendicular to the 2-2 composite layers, which would also lead to the parallel mixing rule being an inadequate description, 3) changes in the surface chemistry during etching of the nickel as previously described, or 4) the presence of local electric fields leading to a finite clamping of the dielectric response.

Table 5-4: Calculated and measured dielectric permittivity at room temperature and at the Curie temperature at 1 kHz for BaTiO₃ and Ba(Zr_{0.05}Ti_{0.95})O₃ epoxy composites.

	25°C Calculated	25°C Measured	T _c Calculated	T _c Measured
BaTiO ₃ Composite	2,852	1,900	4,508	2,600
Ba(Zr _{0.05} Ti _{0.95})O ₃ Composite	2,944	2,800	6,256	4,400

The polarization vs. electric field hysteresis loop was measured at 10 Hz on a BaTiO₃ ceramic sample to determine the coercive field (E_c) for poling. Figure 5-20 shows the hysteresis of the BaTiO₃ ceramic. The measured E_c was ~ 3 kV/cm, which correlates well with previous studies.²⁶ The data shows a small contribution from loss, since the polarization vs. field does not come to a point at high fields but remains rounded. This could well be due to the influence of the incomplete reoxidation of the ceramic, so that there is a residual concentration of oxygen vacancies (with the associated trapped electrons). These oxygen vacancies would be introduced during the low pO₂

sintering. In future work, it is recommended that the reoxidation conditions for these ceramics be optimized. As is typical for BaTiO₃ ceramics, the remanent polarization is considerably smaller than the maximum polarization.³¹

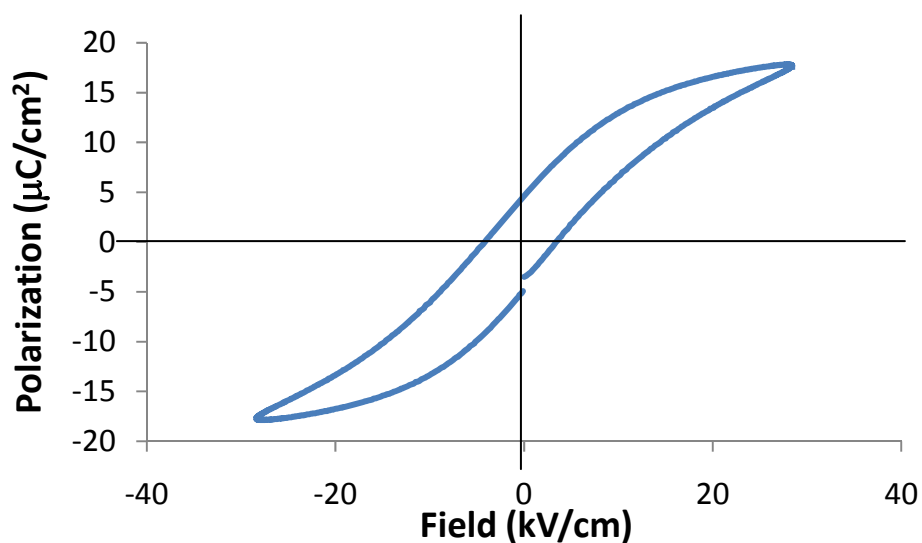


Figure 5-20: Polarization vs. electric field for a BaTiO₃ ceramic measured at 10 Hz.

Measurements were made of the bipolar and unipolar strain vs. field for the sample and electrode geometry in Figure 5-21. The electric field for poling was applied along the 3-axis, and the strain response was measured along the same axis (d_{33} measurements).

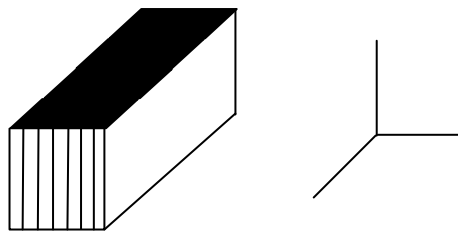


Figure 5-21: Schematic showing the configurations of the composite geometry used for the d_{33} strain vs. field and the d_{31} resonance measurements. The black regions represent the electrode area.

Figures 5-22 and 5-23 show the bipolar and unipolar strain vs. electric field behavior of the BaTiO₃ ceramic and BaTiO₃ / epoxy composite samples at 1 Hz, respectively. The ceramic sample showed a maximum strain of ~ 0.12 % at a field of 23 kV/cm. The BaTiO₃ / epoxy sample showed a strain of ~0.10 % at the same field strength. The d_{33} was estimated from the slope of the <10 kV/cm region of the unipolar strain vs. field measurement on decreasing field (Figure 5-23). The d_{33} of the BaTiO₃ ceramic and BaTiO₃ / epoxy composite were 70 pC/N and 65 pC/N, respectively.

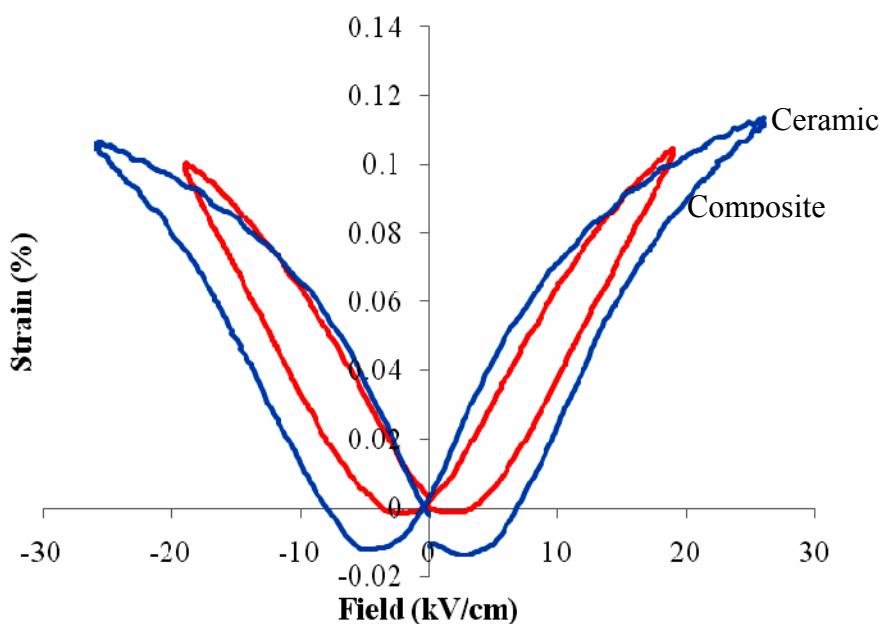


Figure 5-22: Bipolar strain vs. electric field for a BaTiO₃ ceramic and composite samples measured at 1 Hz.

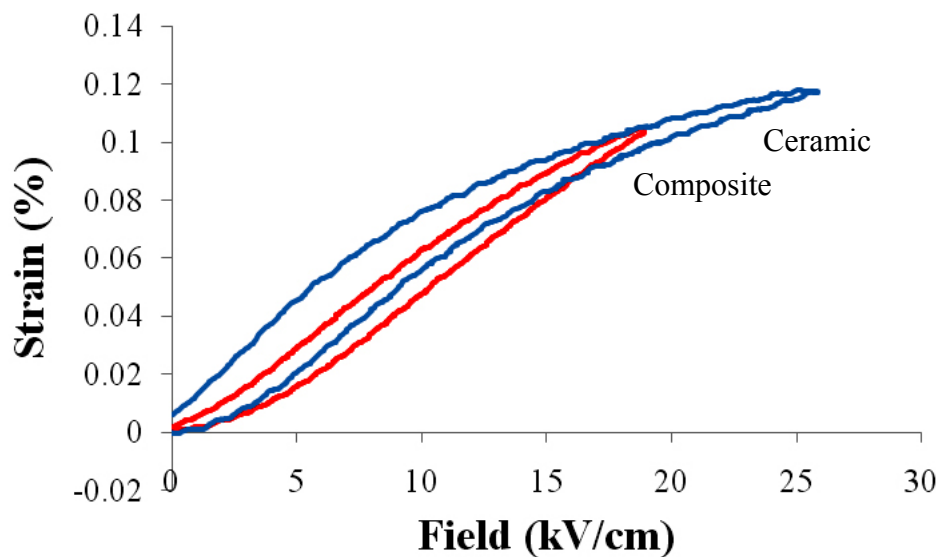


Figure 5-23: Unipolar strain vs. electric field for a BaTiO₃ ceramic and composite samples measured at 1 Hz.

Figures 5-24 and 5-25 show the bipolar and unipolar strain vs. electric field behavior of the Ba(Zr_{0.05}Ti_{0.95})O₃ ceramic and Ba(Zr_{0.05}Ti_{0.95})O₃ / epoxy composite samples at 1 Hz, respectively. The ceramic sample showed a maximum strain of ~0.11 % at a field of 20 kV/cm. The Ba(Zr_{0.05}Ti_{0.95})O₃ / epoxy sample showed a strain of ~0.08 % at 15 kV/cm. The d_{33} was estimated by the same method described above and the d_{33} of the Ba(Zr_{0.05}Ti_{0.95})O₃ ceramic and Ba(Zr_{0.05}Ti_{0.95})O₃ / epoxy composite were 68 pC/N and 61 pC/N, respectively.

Rehrig et al. measured the d_{33} coefficient of BaTiO₃ and Ba(Zr_{0.05}Ti_{0.95})O₃ TGG single crystals and reported values near 140 pC/N and 350 pC/N, respectively.²⁶ The samples were measured along the pseudocubic [001] direction from the high field (>20 kV/cm) unipolar strain vs. field measurements. The BaTiO₃ d_{33} of 140 pC/N is in good agreement with Jaffe et al.²⁸ In this study, both the polycrystalline ceramic and ceramic / epoxy composites showed a lower d_{33} (roughly half the value). It is believed that one reason for the smaller piezoelectric constants in this work is grain size. Demartin and Damjanovic illustrated the effect of the grain size on piezoelectric coefficients of

polycrystalline BaTiO₃ ceramics. For coarse grained samples (~26 μm) the d₃₃ was 120 pC/N.³² Their fine grained BaTiO₃ samples (~0.6 μm) showed a d₃₃ of 60 pC/N.³² The fine grained sample is in agreement with the results reported here, since the average grain size of the ceramics and ceramic / epoxy composites were ~ 3 μm. Thus it is possible that the d₃₃ values should range between the 60 pC/N and the 120 pC/N reported by Demartin and Damjanovic.³² These results are very encouraging, as they suggest that it is possible to make composite samples using tape cast piezoelectrics cofired with metallization *without significantly degrading the piezoelectric response during subsequent processing*. The results might be expected to be even better with a Pb-based piezoelectric, since they tend to be less susceptible to leaching than BaTiO₃.

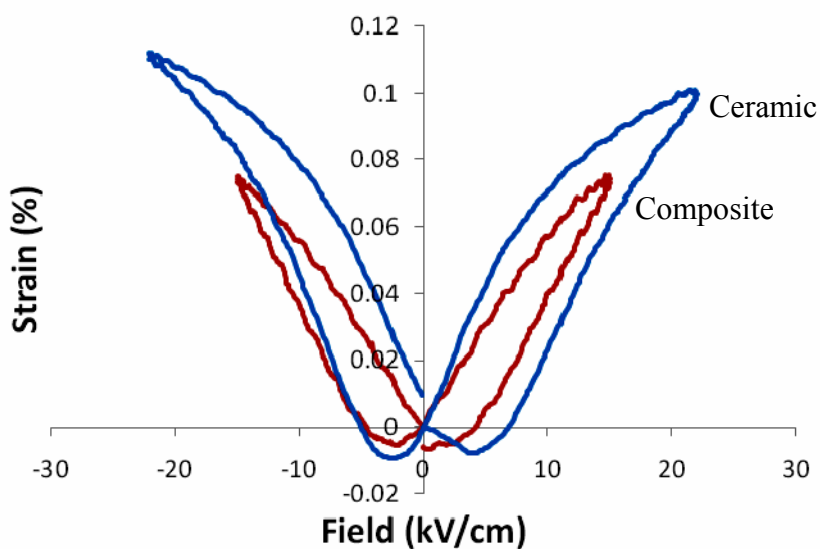


Figure 5-24: Bipolar strain vs. electric field for a Ba(Zr_{0.05}Ti_{0.95})O₃ ceramic and composite samples measured at 1 Hz.

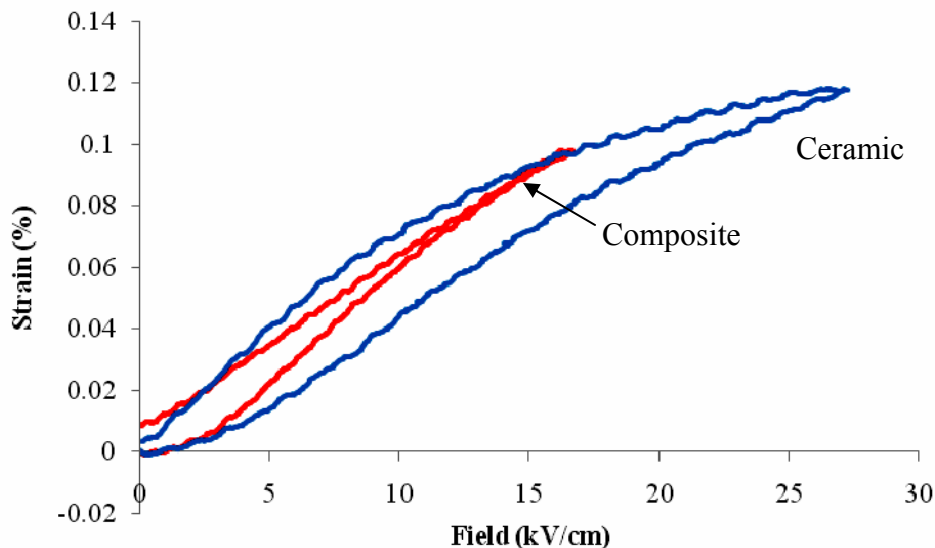


Figure 5-25: Unipolar strain vs. electric field for a $\text{Ba}(\text{Zr}_{0.05}\text{Ti}_{0.95})\text{O}_3$ ceramic and composite samples measured at 1 Hz.

The transverse electromechanical coupling coefficients for the BaTiO_3 and $\text{Ba}(\text{Zr}_{0.05}\text{Ti}_{0.95})\text{O}_3$ ceramic and epoxy composites are listed in Table 5-5. The sample and electrode geometry is shown schematically in Figure 5-21. The poling field was applied along the 3-axis. The field for the resonance measurement was applied along the same axis, and the length extension resonance mode was measured. This was confirmed through the frequency constant of BaTiO_3 (roughly $2200 \text{ Hz}\cdot\text{m}$)³³ and the measured sample dimensions. Also, the resonance measurement was conducted on samples immediately after poling, without any aging and without a DC bias. After aging for 24 h, no resonance was observed for the electromechanical coupling measurements, suggesting considerable local internal fields in the ceramic that lead to depoling. The d_{31} values obtained here are roughly half the value of the d_{33} values reported above. In general, the d_{31} coefficients of the epoxy composites were comparable to the ceramics of the same composition, taking into account the error associated with the measurement. The clamped dielectric constant was estimated from the capacitance measured at 5 MHz and at room temperature for each sample.

It should be noted that the d_{31} value measured here corresponds to the direction where the piezoelectric phase is continuous (since the length, rather than the width extensional mode was employed). Of the two transverse directions (parallel and perpendicular to the layers of the 2 -2 composite, this direction should provide the larger piezoelectric response. The d_{31} values are in good agreement with the d_{31} of -34.5 pC/N reported by Jaffe et al.²⁸ on BaTiO₃ single crystals.

Table 5-5: Transverse electromechanical coefficients of BaTiO₃ and Ba(Zr_{0.05}Ti_{0.95})O₃ ceramic and composite samples.

Property	BT Ceramic	BZT Ceramic	BT Epoxy Composite	BZT Epoxy Composite
k_{31}	0.12 ± 0.02	0.16 ± 0.02	0.11 ± 0.02	0.11 ± 0.02
$s_{11}^D (10^{-12} \text{ m}^2/\text{N})$	16.3 ± 0.2	10.5 ± 0.2	11.8 ± 0.2	7.4 ± 0.2
$s_{11}^E (10^{-12} \text{ m}^2/\text{N})$	16.7 ± 0.2	10.8 ± 0.2	12.1 ± 0.2	7.6 ± 0.2
d_{31} (pC/N)	-38 ± 2	-36 ± 2	-36 ± 2	-35 ± 2

The d_{33} and d_{31} equations derived for the parallel model are given in Equation 5-2 and 5-3 below, where V is the volume fraction, d_{33}^* and d_{31}^* are the calculated composite piezoelectric coefficients, and s is the compliance.³⁰

$$d_{33}^* = \frac{(V^{Ceramic} d_{33}^{Ceramic} s_{33}^{Epoxy} + V^{Epoxy} d_{33}^{Epoxy} s_{33}^{Ceramic})}{V^{Ceramic} s_{33}^{Epoxy} + V^{Epoxy} s_{33}^{Ceramic}} \quad 5-2$$

$$d_{31}^* = V^{Ceramic} d_{31}^{Ceramic} + V^{Epoxy} d_{31}^{Epoxy} \quad 5-3$$

The epoxy has a d_{33} and d_{31} of zero, and an s_{33} of $\sim 150 \text{ pm}^2/\text{N}$. Using compliance values of $15 \text{ pm}^2/\text{N}$ ²⁸ and $20 \text{ pm}^2/\text{N}$ ²⁶ for the BaTiO₃ and Ba(Zr_{0.05}Ti_{0.95})O₃, respectively, the change in d_{33} and d_{31} of the composite can be approximated. Table 5-6 shows the calculated d_{33} and d_{31} coefficients compared to the measured coefficients for the two ceramic / epoxy composites. The d_{33} values are slightly higher for the calculated results, but this is probably a consequence approximating the s_{33} coefficient from single

crystal data. The d_{31} measured values are in good agreement within the amount of error associated with the calculations.

Table 5-6: Measured and calculated d_{33} and d_{31} coefficients assuming the parallel model for the BaTiO_3 and $\text{Ba}(\text{Zr}_{0.05}\text{Ti}_{0.95})\text{O}_3$ / epoxy composites.

	d_{33} Measured (pC/N)	d_{33} Calculated (pC/N)	d_{31} Measured (pC/N)	d_{31} Calculated (pC/N)
BaTiO_3	65 \pm 2	68 \pm 2	-36 \pm 2	-35 \pm 2
$\text{Ba}(\text{Zr}_{0.05}\text{Ti}_{0.95})\text{O}_3$	61 \pm 2	66 \pm 2	-35 \pm 2	-33 \pm 2

Cao et al. showed that due to the periodic array of the 2-2 ceramic / epoxy configuration, the d_{33} coefficient should decrease with increasing volume fraction of epoxy.³⁴ The calculated change in the d_{33} based on Cao et al.'s work, for an 8 vol% epoxy composite would be roughly 5%. This would correspond to $\sim 2 - 3$ pC/N change in the epoxy composite samples produced in this study. Therefore, the ceramic / epoxy composites fabricated in this study was within the range the parallel model predicted for the d_{33} values.³⁴

Comparing the results from the piezoelectric coefficient measurements to the dielectric data, a few of the potential problems originally proposed for the loss in dielectric constant can be eliminated. Since the d_{33} values of the composite are similar to the polycrystalline ceramics, the proposed excess epoxy near the electrodes is not likely to be the main cause in the dielectric permittivity drop, as this should have decreased the piezoelectric response. Thus, it would seem that a more significant cause for the dielectric permittivity change is surface damage of the piezoelectric phase from the etching procedure. Also defect dipoles present in the composite samples could cause the internal fields formed to lower the dielectric permittivity response compared to the polycrystalline ceramic samples.

Properties of the single crystal / epoxy composites could not be measured due to the high loss. This could be from insufficient re-oxidization of the leached composite or the removal of the nickel layers prior to backfilling with the epoxy. It would be important in the future to re-measure the dielectric and piezoelectric properties on

samples which were optimally re-oxidized. This might allow property degradation from oxygen vacancy content from property degradation due to surface defects associated with the composite fabrication process to be unambiguously separated.

5.5 Conclusions

A new process has been developed to mediate lateral single crystal growth with nickel layers. The growth rates for single crystal conversion were 3 – 4 $\mu\text{m}/\text{h}$ and were similar for both BaTiO_3 and $\text{Ba}(\text{Zr}_{0.05}\text{Ti}_{0.95})\text{O}_3$ using [001] and [110] single crystals at 1250°C in 1×10^{-11} atm PO_2 . Single crystal growth of $\sim 350 \mu\text{m}$ has been achieved, and single crystal elements with an 8:1 height to width were fabricated.

The metal – mediated single crystal growth technique was employed to produce 2-2 single crystal (or polycrystalline ceramic)/polymer composites. Using tape casting combined with screen printed metal layers, 2-2 composites were formed with ceramic thicknesses in the range of 4 – 70 μm and metal layer thickness ranging from 1.5 – 5 μm . With improved processing, it is anticipated that both the dielectric and electrode thicknesses could be decreased below 1 μm . Single crystal/metal composites were fabricated by single crystal conversion of the ceramic layers using BaTiO_3 single crystal templates. By selectively removing the metal layers by acid etching and backfilling with epoxy, the final ceramic/polymer composites can be made with a range of pitches, single crystal (or ceramic) layers, and kerfs.

The fine scale ceramic / epoxy composites show promise for piezoelectric transducers fabricated by the metal – mediated ceramic approach. The d_{33} values of the BaTiO_3 / epoxy and $\text{Ba}(\text{Zr}_{0.05}\text{Ti}_{0.95})\text{O}_3$ / epoxy composites were similar to the polycrystalline ceramics of the same composition, as predicted by current models. The d_{33} values reached a maximum of 70 pC/N and 68 pC/N for the BaTiO_3 / epoxy and $\text{Ba}(\text{Zr}_{0.05}\text{Ti}_{0.95})\text{O}_3$ / epoxy composites, respectively.

5.6 References

1. Bowen, L., R. Gentilman, F. Daniel, H. Pham, W. Serwatka, C. Near, and B. Pazol, "Design, Fabrication, and Properties of SonoPanel 1-3 Piezocomposite Transducers," *Ferroelectrics*, **187**: 109-20 (1996).
2. Smith, W.A., "Composite Piezoelectric Materials for Medical Ultrasonic Imaging Transducers - A Review," *6th IEEE Int. Symp. Appl. Ferroelectrics*, **June**[8-11]: 249-56 (1986).
3. Cauchy, C.J. "Thermoelectric Module" US 5448109, 1995.
4. Ohta, T. and T. Kajikawa "Process for Producing a Thermoelectric Module" US 4902648, 1990.
5. Zou, X.-Y., Q. Chen, B. Liang, and J.-C. Cheng, "Control of the Elastic Wave Bandgaps in Two-Dimensional Piezoelectric Periodic Structures," *Smart Materials and Structures*, **17**: 1-5 (2008).
6. Yin, J., M. Lukacs, K. Harasiewicz, and S. Foster, "Ultra-Fine Piezoelectric Composites for High Frequency Ultrasonic Transducers," *IEEE Int. Ultrasonics, Ferroelectrics, and Frequency Control*, **3**: 1962-5 (2004).
7. Jong, N.D., J. Souquet, G. Faber, and N. Bom, "Transducers in Medical Ultrasound: Part Two - Vibration Modes, Matching Layers and Grating Lobes," *Ultrasonics*, **23**[4]: 176-82 (1985).
8. Abrar, A., D. Zhang, B. Su, T.W. Button, K.J. Kirk, and S. Cochran, "1-3 Connectivity Piezoelectric Ceramic-Polymer Composite Transducers Made with Viscous Polymer Processing for High Frequency Ultrasound," *Ultrasonics*, **42**: 479-84 (2004).
9. Safari, A., M. Allahverdi, and E.K. Akdogan, "Solid Freeform Fabrication of Piezoelectric Sensors and Actuators," *J. Mat. Sci.*, **41**: 177-98 (2006).
10. Cannata, J.M., Q.F.Zhou, and K.K. Shung, "Development of a High Frequency (35 MHz) Linear Ultrasonic Array using 2-2 Composite Elements," *IEEE Ultrasonics Symposium Proceedings*, **2**: 894-7 (2004).
11. Michau, S., P. Mauchamp, and R. Dufait, "Piezocomposite 30MHz Linear Array for Medical Imaging: Design Challenges and Performances Evaluation of a 128 Elements Array," *IEEE Ultrasonics Symposium Proceedings*, **2**: 898-901 (2004).

12. Lukacs, M., J. Yin, G. Pang, R. Garcia, E. Cherin, R. Williams, F.S. Foster, and J. Mehi, "Performance and Characterization of High Frequency Linear Arrays," *IEEE Ultrasonics Symposium Proceedings*, **1**: 105-8 (2005).
13. Jiang, X., J.R. Yuan, A. Cheng, K. Snook, P.J. Cao, P.W. Rehrig, W.S. Hackenberger, G. Lavalle, X. Geng, and T.R. Shrout, "Microfabrication of Piezoelectric Composite Ultrasound Transducers (PC-MUT)," *IEEE Ultrasonics Symposium Proceedings*, **2**: 918-21 (2006).
14. Jung, J.K. and W.J. Lee, "Dry Etching Characteristics of Pb(Zr,Ti)O₃ Films in CF₄ and Cl₂/CF₄ Inductively Coupled Plasmas," *Jap. J. Appl. Phys.*, **40**: 1408-19 (2001).
15. Wang, S., X. Li, K. Wakabayashi, and M. Esashi, "Deep Reactive Ion Etching of Lead Zirconate Titanate Using Sulfur Hexafluoride Gas," *J. Am. Ceram. Soc.*, **82**[5]: 1339-41 (1999).
16. Zola, J. "Method for Fabricating Composite Transducers: Laminating Piezoelectric Material and Passive Material" US Patent 4 514 247, April 30, 1985.
17. Stevenson, J.W., M.R. Reidmeyer, and W. Huebner, "Fabrication and Characterization of PZT/Thermoplastic Polymer Composites for High Frequency Phased Arrays," *J. Am. Ceram. Soc.*, **77**[9]: 2481-4 (1994).
18. Ritter, T.A., T.R. Shrout, R. Tutwiler, and K.K. Shung, "A 30-MHz Piezo-Composite Ultrasound Array for Medical Imaging Applications," *IEEE Trans. on Ultrasonics, Ferroelectrics, and Frequency Control*, **49**[2]: 217-30 (2002).
19. Hackenberger, W., S. Kwon, P. Rehrig, K. Snook, S. Rhee, and X. Geng, "2-2 PZT-Polymer Composites for High Frequency (>20 MHz) Ultrasound Transducers," *IEEE Ultrasonics Symposium Proceedings*, **2**: 1253-6 (2002).
20. Button, T.W., S. Cochran, K.J. Kirk, D. MacLennan, A. MacNeil, K. McDonald, C. Meggs, D. Rodriguez-Sanmartin, R. Webster, and D. Zhang, "Net-Shape Ceramic Manufacturing as an Aid to Realize Ultrasonic Transducers for High-Resolution Medical Imaging," *IEEE Ultrasonics Symposium*: 1625-8 (2005).
21. Lukacs, M., M. Sayer, G. Lockwood, and S. Foster, "Laser Micromachined High Frequency Ultrasonic Arrays," *IEEE Ultrasonics Symposium Proceedings*, **2**: 1209-12 (1999).
22. Kim, E.-Y., J.-C. Lee, B.-S. Kim, M.-S. Kim, and J. Jeong, "Leaching Behavior of Nickel from Waste Multi-Layer Ceramic Capacitors," *Hydrometallurgy*, **86**: 89-95 (2007).

23. Anderson, D.A., J.H. Adair, D. Miller, J.V. Biggers, and T.R. Shrout, Surface Chemistry Effects on Ceramic Processing of BaTiO₃ Powder, in *Ceramic Powder Science II*. 1988: Westerville, OH. p. 485-92.
24. Erhart, P. and A. Karsten, "Modeling the Electrical Conductivity in BaTiO₃ on the Basis of First-Principles Calculations," *J. Appl. Phys.*, **104**[4]: 044315/1-044315/8 (2008).
25. Polotai, A.V., G.-Y. Gai, E.C. Dickey, and C.A. Randall, "Utilization of Multiple-State Sintering to Control Ni Electrode Continuity in Ultrathin Ni-BaTiO₃ Multilayer Capacitors," *J. Am. Ceram. Soc.*, **90**[12]: 3811-7 (2007).
26. Rehrig, P.W., *Templated Grain Growth of BaTiO₃-Based Perovskite Single Crystals*, PhD. in *Materials Science and Engineering*. 1999, the Pennsylvania State University. p. 129.
27. Lee, B.-K., S.-Y. Chung, and S.-J. Kang, "Grain Boundary Faceting and Abnormal Grain Growth in BaTiO₃," *Acta. Mater.*, **48**: 1575-80 (2000).
28. Jaffe, B., W.R. Cook, and H. Jaffe, Piezoelectric Ceramics. 1971, Marietta, OH: R.A.N. Publishers.
29. Jona, F. and G. Shirane, Barium Titanate, in *Ferroelectric Crystals*. 1962, Pergamon Press: New York, NY. p. 108-215.
30. Uchino, K., Ferroelectric Devices. 2000, New York: Marcel Dekker, Inc.
31. Park, S.E. and T.R. Shrout, "Ultrahigh Strain and Piezoelectric Behavior in Relaxor Based Ferroelectric Single Crystals," *J. Appl. Phys.*, **82**[4]: 1804-11 (1997).
32. Demartin, M. and D. Damjanovic, "Dependence of the Direct Piezoelectric Effect in Coarse and Fine Grained Barium Titanate Ceramics on Dynamic and Static Pressure," *Appl. Phys. Lett.*, **68**[21]: 3046-8 (1996).
33. Levinson, L.M., Electronic Ceramics: Properties, Devices, and Applications. 1988, New York, NY: M. Dekker.
34. Cao, W., M. Zhang, and L.E. Cross, "Theoretical Study on the Static Performance of Piezoelectric Ceramic-Polymer Composites with 2-2 Connectivity," *IEEE Trans. on Ultrasonics, Ferroelectrics, and Frequency Control*, **40**[2]: 103-9 (1993).

Chapter 6

Summary and Future Work

6.1 Summary

The overall goal of this study was to develop a process that would enable control over the location and orientation of single crystals grown into a polycrystalline matrix. The objectives to achieve that goal were three fold: 1) to understand the factors involved in controlling local enhanced grain growth and single crystal growth in dense BaTiO₃ while limiting matrix grain growth, 2) to determine how to mediate the growth of single crystal elements during solid state conversion with metal interlayers in a 2-2 BaTiO₃ ceramic / nickel composite, and 3) to correlate the piezoelectric properties with the scale of 2-2 single crystal / epoxy composites produced by the metal mediated single crystal growth process.

A process was developed for enhanced grain growth on a local scale. The process involved the deposition of a dopant on the surface of a dense polycrystalline matrix in a patterned array. This was accomplished by spin coating TiO₂ on the surface of a polycrystalline BaTiO₃ matrix and using both optical photolithography and wet etching to define the spacial location of the deposited TiO₂. To control the local grain growth enhancement, adjustments in the Ba/Ti ratio from the excess doped TiO₂ was utilized to increase the average grain size under the deposited TiO₂ pattern. Combining the Ba/Ti ratio adjustments and modifying the PO₂ atmosphere, grain growth enhancement on a local scale while limiting matrix grain growth was achieved. The grain growth enhancement region was named the diffusion affected zone, because it was the region where exaggerated grain growth was induced by Ti⁴⁺ diffusion from the surface doping.

The specific conditions for enhancing grain growth at the surface of BaTiO₃ while limiting the matrix coarsening were determined. The depth of the diffusion affected zone was directly related to the amount of surface doped TiO₂ and the growth atmosphere.

The optimal conditions for the growth from the TiO₂ surface doped BaTiO₃ were heating at 1300°C in a PO₂ of 1x10⁻⁵ atm with TiO₂ coating thicknesses below 100 nm. For samples fired in air, matrix coarsening occurred away from the diffusion affected zone. The average matrix grain size increased to 20 – 30 μm after 2 h. In contrast, matrix coarsening could be limited by heating at lower oxygen partial pressures. For example, the matrix grain size was maintained around 3-4 μm for samples heated at 1300°C in a PO₂ of 1x10⁻⁵ atm for 2 h. For TiO₂ thicknesses above 100 nm, the depth of the diffusion affected zone increased from ~ 40 μm (100 nm TiO₂) to ~ 250 μm (150 nm TiO₂) after 2 h at 1300°C in a PO₂ of 1x10⁻⁵ atm. The change in the diffusion affected zone thickness for the 100 nm and 150 nm TiO₂ samples is presumably due to a change in the grain boundary diffusion rate. For the samples with 150 nm TiO₂, the concentration caused exaggerated grain growth to occur thus increasing the diffusion affected zone compared to the <100 nm TiO₂ samples.

The patterned TiO₂ surface doped layer, described by the above process, was used to determine the amount of lateral and vertical growth from the doped surface. For samples fired in air, the growth distances were roughly the same for the lateral and vertical directions. Somewhat more pronounced anisotropy in the growth rates was achieved when samples were heat-treated in a reducing atmosphere. For example, for samples heat-treated at 1300°C in a PO₂ of 1x10⁻⁵ atm, there was only a few microns (~5 μm) of lateral growth for <100 nm TiO₂ layers. The vertical distance reached up to 40 μm after 2 h for a 100 nm TiO₂ layer. For the 150 nm TiO₂ layer, the vertical and lateral growth distances of the diffusion affected zone were the same as the air fired samples. This difference can be attributed to the increase in concentration of TiO₂ to cause exaggerated grain growth to occur for TiO₂ levels above 150 nm. The patterned diffusion affected zone grain structure did not result in a preferred orientation of the large surface – nucleated BaTiO₃ grains.

To control the orientation of the grains in the diffusion affected zone, a new process needed to be developed. This process involved the control of the location and orientation for BaTiO₃ crystal growth in by solid state conversion. The new process involves the same conditions outlined earlier for grain growth enhancement by TiO₂

surface doping, but with a few additions. A method of producing a patterned array of oriented BaTiO₃ crystal templates was developed by using optical photolithography and dry etching techniques (ICP-RIE). Combining the modifications from Ba/Ti ratio adjustments (by TiO₂ doping) and PO₂ atmosphere control with the patterned single crystal templates, solid state single crystal growth of oriented grains while limiting matrix grain growth was achieved.

In this study, a patterned single crystal with a 1000 μm line pattern array with a template relief of 1 μm was used to template crystal growth by solid state conversion. Orientation control was achieved with patterned [100] and [110] BaTiO₃ single crystals. The growth rates characteristic of propagation of the single crystal boundary into the matrix were 10 – 15 μm/h for the vertical growth rates for both [100] and [110] orientations, while the lateral growth rates were 10 – 15 μm/h and 5 – 10 μm/h for [100] and [110] orientations, respectively at 1300°C in 1x10⁻⁵ atm PO₂. The slow growth rates were attributed to the partial reduction of Ti⁴⁺ to Ti³⁺, combined with sintering below the liquid-phase sintering temperature of 1332°C. There were no detectable changes in the growth rates after the equilibrium morphology of the single crystal growth was achieved. Orientation control by the patterned single crystal in the enhanced growth regions was confirmed with EBSD. Although this study focused on using a line pattern for oriented grain growth, it can be envisioned that a variety of template shapes and spatial distributions can be used to provide an array of oriented grains in a polycrystalline matrix.

A new process was developed to produce high aspect ratio, oriented grains in a polycrystalline matrix. Oriented grains of only 2:1 height to width aspect ratio was possible with the patterned single crystal technique for fabricating oriented grains in BaTiO₃. Thus, a new method for mediating lateral solid state crystal growth is needed to obtain higher aspect ratio grains. To mediate the solid state crystal growth, the polycrystalline matrix was modified by the addition of metal layers in an array. Using alternating stacked tape cast BaTiO₃ and screen printed nickel layers, a 2-2 composite structure was fabricated. Nickel was chosen to mediate the lateral growth during single crystal conversion because it can be co-fired at a sufficiently low temperature to obtain

dense nickel layers with fine-grained BaTiO₃. With this technique high aspect ratio oriented grains of 8:1 height to width aspect ratio were achieved with [001] and [110] BaTiO₃ single crystals. The high aspect ratio, patterned array structure can be utilized in several applications, but the focus of this research was on 2-2 ultrasonic transducers.

To mediate single crystal growth in BaTiO₃ with Ni required new conditions for crystal growth. The PO₂ was changed to 1x10⁻¹¹ atm to avoid the oxidation of nickel, however the other process conditions determined from the patterned single crystal were unchanged. Thus, an approach was developed for fabricating 2-2 single crystal / polymer composites by the metal –mediated single crystal growth technique. The process was adapted to produce 2-2 BaTiO₃ and Ba(Zr_{0.05}Ti_{0.95})O₃ ceramic / nickel composites. The 2-2 composites were formed with ceramic thicknesses in the range of 4 – 70 μm and the metal layer thickness ranged from 1.5 – 5 μm. Single crystal / nickel composites were fabricated by single crystal conversion of the ceramic layers using [001] and [110] BaTiO₃ single crystals.

The optimal conditions for single crystal growth using BaTiO₃ and nickel were observed at 1300°C and a PO₂ of 1x10⁻¹¹ atm occurred. For oxygen partial pressures below 1x10⁻¹³ atm, no single crystal growth was measured. The growth rates for the single crystal conversion were measured as 3 – 3.5 μm/h and 3.5 – 4 μm/h for BaTiO₃ and Ba(Zr_{0.05}Ti_{0.95})O₃, respectively at a PO₂ of 1x10⁻¹¹ atm. There was no significant difference in the growth rates between the [001] and [110] single crystals templates. Single crystal growth distances up to ~350 μm were achieved after 100 h at 1250°C in a PO₂ of 1x10⁻¹¹ atm. 2-2 single crystal / epoxy composites were fabricated by selectively leaching the nickel layers with dilute HNO₃ and backfilling with epoxy.

Preliminary measurements on the single crystal / epoxy composites showed a high degree of conductivity and were unsuitable for further dielectric and piezoelectric measurements. The high conductivity could be from insufficiently re-oxidization of the BaTiO₃ single crystal or from incomplete removal of the nickel in the 2-2 composite structure. Fine scale polycrystalline **ceramic** / epoxy composites which were fabricated by the metal – mediated ceramic patterning approach show promise for piezoelectric transducers. The d₃₃ values of the BaTiO₃ / epoxy and Ba(Zr_{0.05}Ti_{0.95})O₃ / epoxy

composites were similar to the polycrystalline ceramics of the same composition. The d_{33} reached a maximum of 55 pC/N and 42 pC/N for the BaTiO₃ / epoxy and Ba(Zr_{0.05}Ti_{0.95})O₃ / epoxy composites, respectively. The d_{31} coefficient was reduced by half in the composite samples compared to the ceramic counterparts.

6.2 Future Work

This thesis outlines the basis for understanding how oriented grain growth in a patterned array in a polycrystalline matrix can be achieved; however, there are several aspects that can be investigated further. The topics include, specific to this study, 1) the diffusion and incorporation of TiO₂ in the BaTiO₃ matrix, 2) fabrication of 2-2 single crystal / epoxy composites for piezoelectric measurements, and in general 3) varying the size, shape, and distribution of templates, and 4) applying the metal – mediated crystal growth method to other piezoelectric systems.

One of the areas that should be investigated further is determining where the TiO₂ dopant is located as a function of heat treatments in the surface doping and the single crystal conversion experiments. It is important to know where and how the TiO₂ is incorporated in the matrix to understand how the coarsening of the matrix occurs, since the heating temperatures are below the liquid formation temperature. This is especially important since there was significant diffusion anisotropy as a function of TiO₂ thickness for samples heated in low PO₂ levels. Determining the diffusion profile of the TiO₂ under different heat treatment atmospheres would enable a more accurate model on how the TiO₂ would affect the single crystal boundary mobility. The data can then be compared to models of diffusion from a finite line source. Also analysis of the diffusion – affected zone's grain boundary structure is needed to determine if the TiO₂ additions stay at the grain boundaries, or if a second phase is formed. With the small amount of TiO₂ added (25 nm layer) the detection of the slight change over the Ti concentration in the ceramic BaTiO₃ is very difficult and needs to be measured by a technique that is sensitive to slight variations in chemistry. Transmission electron microscopy, electron

energy loss spectroscopy, and electron probe microscopy should help in determining if a second phase is present and how the TiO_2 is incorporated into the matrix.

There are a few issues that need further attention for fabricating single crystal / epoxy composites of suitable quality for piezoelectric measurements. The main issue is the successful bonding, nucleation, and growth of the single crystal orientation along **all** of the ceramic elements in the composite structure. There have been several attempts where only a fraction of the ceramic elements have been successfully converted to the single crystal orientation, however any unconverted ceramic layers would be problematic in the end piezoelectric response. Thus further evaluation of the preparation and bonding technique for the composite crystal growth is needed to avoid this issue. Further study on the reason behind the high conductivity of the single crystal / epoxy composites is needed to improve the piezoelectric response of the grown crystals. The high conductivity issues could be from the incomplete re-oxidation or removal of the nickel layers during the ceramic / epoxy composite fabrication.

It would also be interesting to ascertain the effects of template shape, orientation, and grown crystal impingement on each other. The first set of experiments would be to change the shape and spacing of the templates. By altering the features of the templates, to squares, circles, triangles, etc. the formation of the equilibrium configuration of the oriented grains can be measured as a function of heat treatment. Also, growth rates from the different shaped templates can be measured and correlated to the final grown crystal shape and size. For example, varying the template spacing from 50 – 500 microns and the heating times from 0 – 10 h would enable crystal impingement studies.

Figure **5-5** shows potential template designs for examining the importance of grown crystals impinging on each other. The arrowed directions indicate the direction of the crystal growth front. Crystal growth could be monitored as a function of crystal orientation, angle, and template spacing. Of particular interest is whether or not the growth rates change as two perfectly oriented grains coalesce. Once this is understood, the study could be extended to examine impingement of crystals of different orientations. This could be accomplished using patterned bi-crystals in combination with the same pattern structures shown in Figure **5-5**. This will provide an understanding how the

misalignment of the oriented grains, as a function of angle and orientation have on the final microstructure and piezoelectric properties.

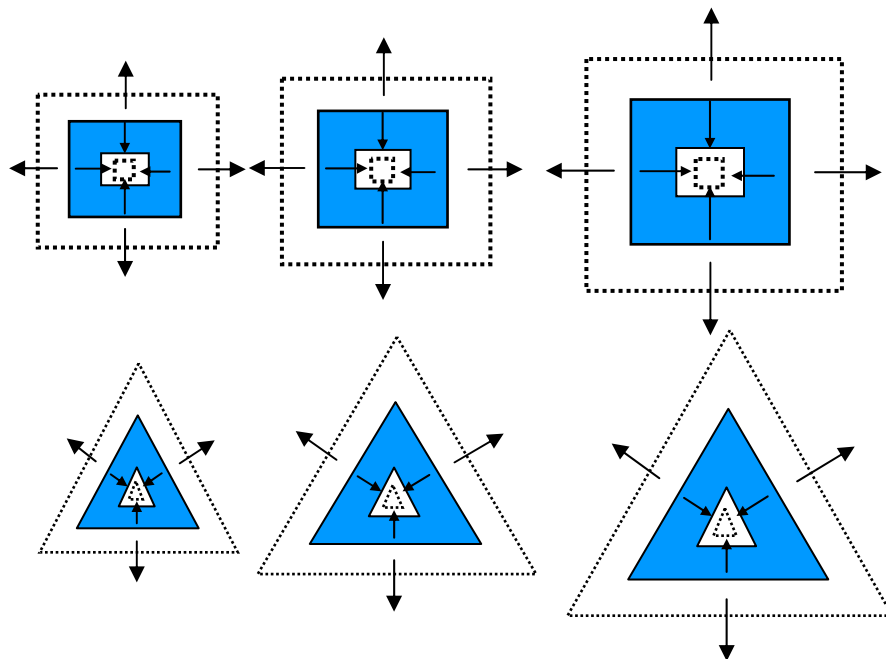


Figure 6-1: Schematic of different template shapes and sizes (colored areas) for single crystal growth impingement experiments. The arrows show the direction of grown crystal directions with the dotted lines projecting the single crystal growth front.

Metal – mediated single crystal growth promises to be a powerful means to regulate solid state conversion on a fine scale leading to composite structures with unique connectivities and compositions. In this study only BaTiO_3 and Ni were used, and the atmosphere required to prevent the oxidation of nickel significantly reduced the single crystal boundary growth rate. To improve the rate, and the aspect ratio of the single crystal elements grown, a more oxidation resistant metal should be investigated, such as Pt, Ag/Pd, and Cu. In addition, this process can be generalized to be used with other piezoelectric ceramics, such as PMN-28PT and PZT, which have a higher piezoelectric response than BaTiO_3 . Co-firing of PZT with base metal electrodes has been demonstrated for multilayer actuators.¹ Also, the metal – mediated crystal growth technique can be applied to other ceramic / metal connectivities, such as a 1-3 composite transducers.

6.3 References

1. Donnelly, N.J., T.R. ShROUT, C.A. Randall, and I.M. Reaney, "Thermochemical Reactions between PZT and Ag/Pd Powders: Relevance to Cofiring of Multilayer Actuators," *J. Am. Ceram. Soc.*, **91**[3]: 1013-8 (2008).

VITA

Michael Stephen Ugorek

Michael Stephen Ugorek was born in Albion, NY in 1980. He graduated from Albion High School in 1998. He earned his B.S. degree in Ceramic Engineering in May 2002 and M.S. degree in Ceramic Engineering in May 2004, both from Alfred University in Alfred, NY. After finishing his Ph.D. in the Spring of 2009 he is planning on working for Owens Corning in Granville, OH as an Advance Engineer. He is a member of The American Ceramic Society, Materials Research Society and Keramos and is publishing a paper and patent on his graduate work.